UNIVERSITY OF OTTAWA

Coherent Anti-Stokes Raman Scattering Miniaturized Microscope

By

Brett Smith

Thesis submitted to the Faculty of Graduate and Postdoctoral Studies in partial fulfillment of the requirements for the degree of Master of Applied Science in Biomedical Engineering

School of Electrical Engineering and Computer Science
University of Ottawa
The Ottawa-Carleton Institute for Biomedical Engineering

Abstract

Microscopy techniques have been developed and refined over multiple decades, but innovation around single photon modalities has slowed. The advancement of the utility of information acquired, and minimum resolution available is seemingly reaching an asymptote. The fusion of light microscopy and well-studied nonlinear processes has broken through this barrier and enabled the collection of vast amounts of additional information beyond the topographical information relayed by traditional microscopes. Through nonlinear imaging modalities, chemical information can also be extracted from tissue. Nonlinear microscopy also can beat the resolution limit caused by diffraction, and offers up three-dimensional capabilities. The power of nonlinear imaging has been demonstrated by countless research groups, solidifying it as a major player in biomedical imaging.

The value of a nonlinear imaging system could be enhanced if a reduction in size would permit the insertion into bodily cavities, as has been demonstrated by linear imaging endoscopes. The miniaturization of single photon imaging devices has led to significant advancements in diagnostics and treatment in the medical field. Much more information can be extracted from a patient if the tissue can be imaged in vivo, a capability that traditional, bulky, table top microscopes cannot offer. The development of new technologies in optics has enabled the miniaturization of many critical components of standard microscopes. It is possible to combine nonlinear techniques with these miniaturized elements into a portable, hand held microscope that can be applied to various facets of the biomedical field.

The research demonstrated in this thesis is based on the selection, testing and assembly of several miniaturized optical components for use as a nonlinear imaging device. This thesis is the first demonstration of a fibre delivered, microelectromechanical systems mirror with miniaturized optics housed in a portable, hand held package. Specifically, it is designed for coherent anti-Stokes

Raman scattering, second harmonic generation, and two-photon excitation fluorescence imaging. Depending on the modality being exploited, different chemical information can be extracted from the sample being imaged. This miniaturized microscope can be applied to diagnostics and treatments of spinal cord diseases and injuries, atherosclerosis research, cancer tumour identification and a plethora of other biomedical applications. The device that will be revealed in the upcoming text is validated by demonstrating all designed-for nonlinear modalities, and later will be used to perform serialized imaging of myelin of a single specimen over time.

Statement of Originality

The author declares that the results presented in this thesis were obtained during the course of his M.A.Sc. research under Dr. Hanan Anis, and that this is, to the best of his knowledge, original work.

The following academic contribution was made from some of the work presented in this thesis:

1. B. Smith, M. Naji, S. Murugkar, E. Alarcon, C. Brideau, P. Stys, H, Anis, “Miniaturized, fibre delivered multimodal CARS exoscope”, (Undergoing peer review for Optics Express).
2. B. Smith, M. Naji, S. Murugkar, C. Brideau, P. K. Stys, H. Anis, “A novel multimodal CARS miniaturized microscope”, Proc. SPIE 8226-74 (2012).
3. S. Murugkar, B. Smith, P. Srivastava, A. Moica, M. Naji, C. Brideau, P. K. Stys, H. Anis, “Miniaturized multimodal CARS microscope based on MEMS scanning and a single laser source”, Optics Express, pp. 23796-23804, 2010.
4. S. Murugkar, B. Smith. C. Brideau, P. Stys, H. Anis, “Development of a fiber optic-based CARS exoscope for the in vivo study of spinal cord disorders”, Proc. Life Science Systems and Applications Workshop, pp. 96-99, 2011.

Table of Contents

List of Figures

Glossary

NIR	Near-Infrared
SHG	Second Harmonic Generation
CARS	Coherent Anti-Stokes Raman Scattering
MS	Multiple Sclerosis
MEMS	Microelectromechanical Systems
MRI	Magnetic Resonance Imaging
TPEF	Two-Photon Excitation Fluorescence
NA	Numerical Aperture
DC	Direct Current
IR	Infrared
SC	Supercontinuum
PCF	Photonic Crystal Fibre
GVD	Group Velocity Dispersion
SPM	Self-Phase Modulation
ZDW	Zero-Dispersion Wavelength
FWM	Four-Wave Mixing
PMT	Photomultiplier Tube
SMF	Single-Mode Fibre
DCPCF	Dual-Clad Photonic Crystal Fibre
GRIN	Gradient-Index Lens
GDD	Group Delay Dispersion
DIP	Dual In-Line Package
FPGA	Field-Programmable Gate Array
USAF	United States Air Force
FWHM	Full Width at Half Maximum
YFP	Yellow Fluorescent Protein
KDP	Dihidrogen Phosphate

Chapter 1

Introduction to Nonlinear Imaging

1.1 A Brief History of Laser Microscopy

The analysis of biological tissue has been the focus of researchers, over many decades to assist in the diagnosis, treatment and general understanding of how the human body works. Living tissue analysis is critical to the understanding of how diseases, infections, viruses, and cellular mutations affect their hosts, and more importantly, how to prevent these from spreading, with the potential of killing the host.

The very first laser based imaging systems were relatively crude compared to today's standards, but they did offer significant advantages over their predecessor, the visible light absorption microscopes. Not only could a laser based system selectively excite fluorophores, it was also not limited to wavelength ranges sensitive to the human eye. The methods used to characterize these fluorescent microscopes are very similar to the methods used in this thesis. Fluorescent microscopes are a significant improvement over traditional imaging systems, but it wasn't until 1957, when Marvin Minsky patented the first method to allow three dimensional imaging with a laser microscope [1], called confocal microscopy. Previously, tissue had to be carefully mechanically sectioned and imaged a single layer at a time; both a time consuming, and cost prohibitive endeavour. The pinhole Minsky introduced was the key first step to allowing out of focus light to be omitted from the detector system, improving image quality and speed of analysis. Despite these benefits, confocal microscopy isn't the most ideal system for imaging living tissue, due to the fact that the entire cone of focus is exposed to, and interacts with a high intensity field of light. The significant amount of energy deposited into the tissue can alter the structure and physical behavior of the sample. Fortunately the

results demonstrated in this thesis do not have this drawback as nonlinear imaging deposits little or no energy into the sample. The first high peak power laser was invented in 1962 by Fred J. McClung, using electrically switched Kerr cell shutters, dubbed Q-switching [2]. It wasn't until 1982, that femtosecond laser sources were developed. Peter F. Moulton of MIT developed the titanium-sapphire laser [3] and this technology has been in use for decades. Many nonlinear imaging techniques were all perfected with the titanium-sapphire laser, all of these modalities exhibiting extremely low sample damage due to the near-infrared (NIR) wavelength of operation.

Figure 1 [4] is an image created by Albert Stolow at the National Research Council Canada showcasing the significance of a multimodal, nonlinear microscope.

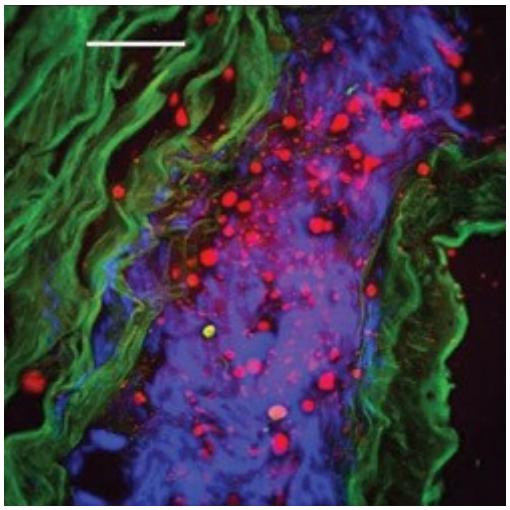

Figure 1: Atherosclerotic rabbit aorta. Red CARS signal from lipids, Blue SHG signal from collagen, and green autofluorescence from elastin [4]

The sample clearly shows blue coloured second harmonic generation (SHG) from collagen, the red coloured lipids from coherent anti-Stokes Raman scattering (CARS), and the green coloured autofluorescence from elastin. Detailed explanations as to how these modalities are generated, and exploited will be presented in the following chapters.

1.2 Motivation

The ability to resolve subcellular structures is paramount to understanding how various diseases progress, and degrade the health of the human race's aging population. Chemical specificity without the need for exogenous fluorophores would also lead to a deeper comprehension as to what the mechanics of these diseases are, and how they affect the quality of life, as well as the lifespan of the patient. Two crucial diseases that would benefit greatly from subcellular resolution, as well as chemical specificity are multiple sclerosis (MS), and ischemic heart disease. This is due to the fact that these diseases are greatly impacted by the presence, and type of lipids that are present in the tissue, as standard microscopy cannot differentiate between lipids and non-lipid structures.

Globally, ischemic heart disease is responsible for 7.25 million human deaths annually [5]. This lack of supply of blood to the heart is typically caused by atherosclerosis of the coronary arteries. It is difficult to identify the risks associated with individual sections of plaque (which is mostly made up of lipids) buildup because current diagnostic techniques are only able to identify the size of the blood vessel's lumen. With this information, physicians can choose to increase the blood flow to the heart by the use of coronary stents, although the majority of complications from atherosclerosis arise from areas of high plaque buildup, which does not necessarily correspond to areas of low blood flow. Identification of the regions of high concentration of plaque is absolutely necessary to begin to save the lives of the more than seven million people who die every year due to this disease. A diagram showing the progression of plaque buildup can be seen in Figure 2 [6].An imaging system that is able to provide chemical specificity could distinguish between normal arterial walls and walls that are saturated with plaque. This ability would give physicians an unstoppable weapon against ischaemic heart disease. The risk of rupture of specific sections could be determined, as well as the composition of the plaque allowing custom tailored drug therapy potentially saving countless lives [7].

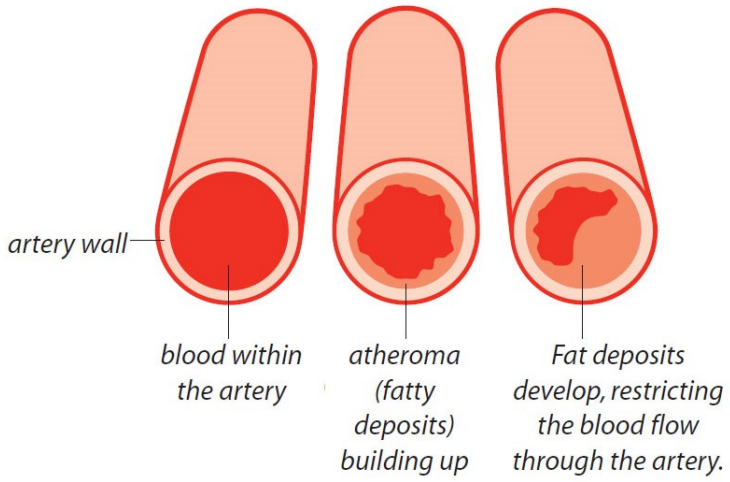

Figure 2: Depiction of arteries and plaque buildup [6]

As mentioned previously, MS would also greatly benefit from the ability to identify specific cellular structure from surrounding tissue. MS is one of the most devastating demyelinating diseases for young adults which affect more than 1.3 million people globally. Up to 60% of those diagnosed with MS are not able to walk within 20 years of receiving that diagnosis. Losing mobility is devastating for the individual as well as to the patient's support system. MS is a demyelinating disease, meaning that the myelin surrounding the axon of a neuron is damaged, or deteriorating (an entire neuron shown in Figure 3 [8]). Understanding the mechanisms behind the destruction of the myelin would give significant insight as to what can potentially be done to reverse the effects of this disease, or prevent it altogether. In order to perform these kinds of investigations, a method of in vivo, label free imaging that can differentiate between different cellular structures must be used.

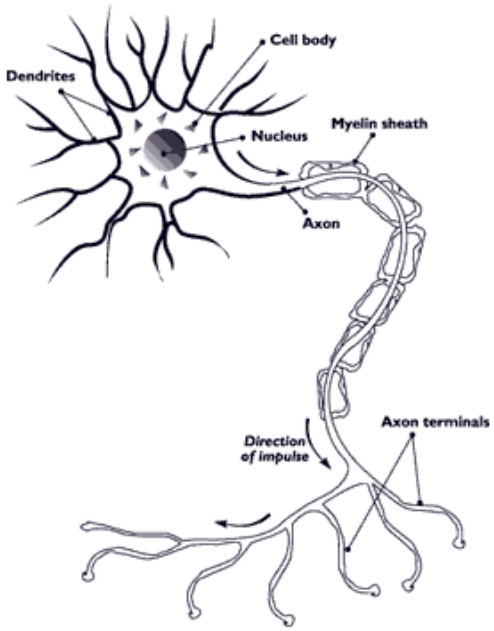

Figure 3: Depiction of a neuron [8]

Multimodal nonlinear microscopy, including CARS and SHG, fortunately are tools that can accomplish this chemical specific imaging modality. Differentiation between plaque riddled and healthy arterial walls is possible with this technique, as well as determining the location of myelin with respect to the axon. CARS microscopy can clearly resolve the lipid rich myelin that degrades as MS tightens its grip. It is for this reason that I have participated in the development of a miniaturized microscope to image myelin. Specifically, the development of this exoscope was to probe the state of decay (or regeneration) of the myelin surrounding the axons contained within the spinal tissue of a rat. The requirements of this study needed a probe that can be inserted into a port on the back of a rat, exposing a small section of the spinal column, while keeping the rat alive and in a healthy state. This preliminary work does not provide a full endoscopic solution that would allow the imaging of the interior of arterial walls necessary to treat atherosclerosis, but it is a stepping stone to enable true endoscopic in vivo imaging. Many of the hurdles associated with in vivo, multimodal, nonlinear imaging have been addressed in the design, assembly and testing of a fibre delivered, microelectromechanical systems (MEMS) scanned miniature microscope that will be discussed in great detail in this thesis.

1.3 Objectives

The motivation behind this thesis is based on the need for clinicians to determine the presence and/or location of lipids. The advancements presented in this thesis can be applied to heart disease, but the main motivation is determining the mechanics of demyelinating diseases, or spinal cord injuries. Performing serialized imaging of spinal tissue is the only way to fully understand these demyelination mechanics. Current spinal tissue white matter imaging techniques involve the sacrifice of multiple specimens, reducing the consistency of individual measurements. When examining the state of decay of myelin, this technique is very resource intensive, and introduces large margins of errors since only a brief snapshot into the myelination state is observed for each experimental specimen. Alternate serialized, noninvasive imaging techniques like magnetic resonance imaging (MRI), can only deliver low resolution measurements, and require costly high-field strength magnets. A slice resolution limit of 0.5 mm restricts the usefulness of MRI studies of the state of myelination.

The ability to image a single mouse over time with microscopic resolution, will give clinicians crucial insight as to the mechanics of MS. Not only will the myelin decay process be able to be examined in detail, strategies to protect the myelin as well as regenerative treatments can be observed.

The primary goal of this thesis is to develop a miniaturized multimodal nonlinear microscope, exploiting CARS, SHG and two-photon excitation fluorescence (TPEF) modalities, with the optical geometry allowing photon collection in the epi direction. This distal end of this miniaturized microscope must have a diameter equal to, or less than 2.0 mm, while maintaining a relatively high numerical aperture (NA) to increase sample power densities and improve the z-sectioning ability. Careful selection of fibre delivery devices and analysis of appropriate dispersion compensation must be done, as well as a critical evaluation of other integrated

miniaturized components. Validation that the exoscope performs according to design specifications will also be performed once the entire assembly is complete.

1.4 Outline

Now that the motivations behind this thesis have been defined, chapter 2 will give an overview of various nonlinear imaging types. The fundamentals that these modalities are based upon will also be discussed, with a brief description of the nonlinear polarizations, as well the significance of the specific type of electronic transition associated with each modality. Comparisons to traditional imaging methods will also be undertaken, and an explanation as to the specific advantages of nonlinear imaging. A significant portion will also be dedicated to understanding the fundamentals of the stimulated Raman processes associated with CARS.

Chapter 3 reveals the developments that have made this thesis possible. The significance of the first papers published on CARS, all the way to the first epi collection of CARS photons will be discussed. Additional milestones associated with the miniaturization of nonlinear endoscopes will be mentioned, including laser technology, beam delivery, optics and scanning mechanisms. Comparisons to the various technologies used in these papers will be deduced. This chapter then focuses on the decided miniaturized components. In-depth analysis of each and every one of the selected components will be made. Detailed explanations of every test performed on these individual components will be analyzed, concluding with a description of the entire setup, from ultrafast photon generation, to photon capture.

The results of the assembled exoscope are discussed in chapter 4. The chapter begins with independent analysis of the focusing optics, and a dual in-line packaged MEMS mirror. Resolution tests as well as biological imaging are undertaken. The

subsequent results are from after the exoscope has been completely assembled, with similar resolution test and biological imaging completed.

As anticipated, the final chapter reflects upon the accomplishments, analyzes the successes, as well as the shortcomings. Short term as well as long term plans for the future employment of the exoscope is discussed.

1.5 Personal Contribution

The bulk of my work was performed after the initial components were selected, and the optics already designed, as this was a group project. The first portion of the project that I was attached to was the operation of the MEMS mirror. Since only the mirror was supplied, the driving electronics and the software needed to be designed. I researched what was needed in order to make the mirror perform as required, as well as writing the initial software. I also designed and constructed the high voltage direct current (DC) square wave converter that was required to operate the MEMS mirror. Once the driving components were completed, I was responsible for the complete testing and characterization of each individual mirror.

Once the assembly of the focusing optics was completed by a local company, preliminary trials combining the MEMS mirror and the optics were performed. I was responsible for integrating those two components with the current microscopy system, as well as performing the imaging of the samples.

Following the confirmation that the optics and MEMS mirror performed as anticipated, I assisted in the assembly of all remaining components into the exoscope. Once the components were installed, I was responsible for confirming the operation and alignment of all optics contained within the exoscope.

Fibre delivery is a crucial part of the exoscope, and I performed dispersion tests on the pair of fibres used in the experiments. I also designed and implemented a prism

compressor to compensate for the dispersion encountered within the delivery fibres. A grating compressor was also used for fibre compensation which was designed by me, but implemented by another PhD student.

With all components at the university, I had to source and prepare samples for resolution testing as well as for biological imaging demonstrations. Once suitable samples were selected prepared, I also performed all the resolution measurements and imaged many of the various other samples included in this thesis. The sourcing and preparation of the biological samples were assisted by a PhD student, as well as by a research associate, who also assisted in acquiring and troubleshooting some of the images taken. The PhD student also was responsible for maintaining the generation of the supercontinuum that will be described in the following chapters.

Chapter 2

Nonlinear Processes: Types and Comparisons, Generation Mechanisms and Advantages

A basic comprehension of nonlinear optics is critical in order to fully understand why nonlinear microscopy is advantageous, and how it affects the selection of components that are vital to a nonlinear microscopy system. This chapter will give an overview as to what are the benefits of nonlinear microscopy, followed by detailed descriptions of the individual processes. More specifically, an examination of the polarization state under intense electric fields will be performed, and how this gives rise to various simple nonlinear effects. Before delving into a description of the more complex CARS process, an explanation of a standard Raman process will be given, as it is fundamental to the understanding of CARS. The last nonlinear effect that will be discussed is supercontinuum generation. It is key to the generation of the anti-Stokes wavelengths for our particular CARS setup.

2.1 A Case for Nonlinear Microscopy

The ability to perform imaging with three-dimensional capabilities has been a highly sought-after goal. A popular method that offers this z-sectioning ability is confocal microscopy. In this modality, a pinhole is used to reject photons that are emitted from out of the plane of interest. While this does give the ability to view individual layers of a sample, there is optical interaction within the entire focal volume. This can cause out of focus areas to become photobleached and cause tissue damage. It also reduces the available penetration depth, as the deeper the photons penetrate, the more likely they are to be absorbed. Z-sectioning is also accomplished through nonlinear microscopy, using near-infrared photons.

Stimulating this nonlinear excitation from wavelengths far from the visible spectrum ensures fewer scattering events as the light passes through the tissue, allowing for

deeper optical penetration before being focused at the region of interest. The water window shown in Figure 4 demonstrates that the absorption of NIR photons within a sample is quite low, still allowing deep penetration of the tissue samples. Using NIR photons in combination with multi-photon absorption enables the emission and collection of photons in the visible spectrum, while still deeply penetrating the tissue samples.

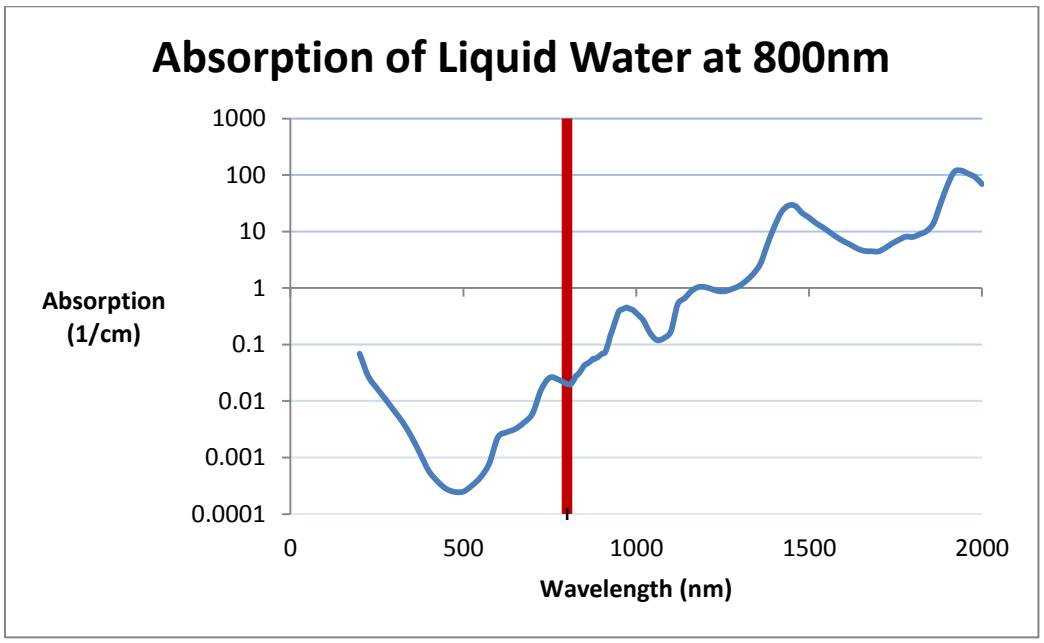

Figure 4: The spectral absorption of liquid water, and plotted 800 nm section (red)

When these NIR photons are focused, the optical field intensity increases. Since the rate of absorption is proportional to the square of the intensity (reasons for this will be discussed in the proceeding sections), only when tightly focused will there be nonlinear interactions. This leads to localization of the generation of nonlinear photons, with out of focus regions remaining inactive in terms of photon interaction. Figure 5 shows the comparison of a linearly active medium in contrast to the small volume of nonlinear interaction.

Since this localization of the generation of detectable photons essentially acts like the pinhole in a confocal microscope, this enables a similar z-sectioning ability.

Different planes of a sample can be imaged at a time simply by translating the sample parallel to the optical axis.

Not only does the localization of the generated nonlinear photons enable 3-D imaging, it also enables sub wavelength resolution. Since the active focal volume is dependent on the nonlinear field strength, the field strength can be reduced to stimulate the nonlinear process within a reduced focal volume smaller than the excitation wavelength.

Another advantage of using NIR photons to excite electronic transitions within a sample is that NIR photons encounter few scattering events, as the energy of the incoming photons is far from the endogenous active (single photon) absorption band. When compared to visible light, this means that the NIR photons can penetrate deeper into the sample, and power densities remain high in the tight focal volume. This means that for all nonlinear modalities, no energy is deposited within the out of focus tissue (at the targeted energy band). This makes the incoming light less phototoxic to the tissue being examined. These properties apply to all nonlinear imaging modalities, (although with TPEF there is some energy deposited into the tissue, as it involves real energy levels and the associated decay lifetimes).

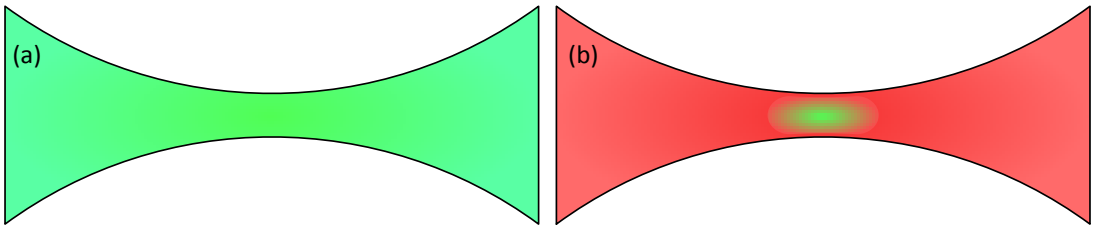

Figure 5: (a) Linear fluorescence interaction volume (Green) (b) Nonlinear interaction volume (Green)

The ability to image individual planes is not the only advantage of nonlinear microscopy, chemical specificity is also enabled through nonlinear imaging. Traditionally, in order to obtain chemical specific structures contained within a sample, exogenous dyes must be added. Not only could the addition of external

material affect the internal processes of live tissue being imaged, dyes are typically carcinogenic. For this reason, it is difficult to perform in vivo fluorescence imaging on living humans. Another obstacle that is present with single photon fluorescence microscopy is the difficulty of separation of the excitation and emission wavelengths. As the energy difference between these two bands of frequencies is not large, filter selection can be quite tedious, and in some cases, impossible. With nonlinear imaging, the pump photons can be easily filtered as they are spectrally distinct. The absorption of multiple photons (during a single atomic transition) in nonlinear microscopy is the reason for this advantage, with a comparative excitation between single photon fluorescence and multiphoton fluorescence pictured in Figure 6 [9].

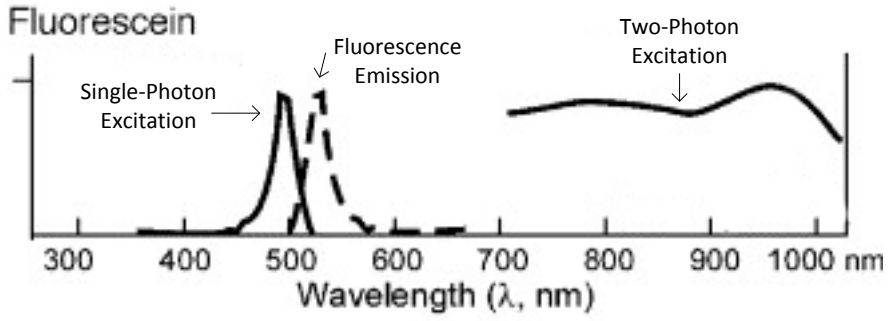

Figure 6: Fluorescein single photon excitation VS two photon excitation and corresponding emission wavelength [9]

2.2 Nonlinear Processes: $\chi^{(2)}$ and $\chi^{(3)}$

The response of a system is said to be nonlinear when the application of an optical field modifies the properties of the material system. The response of the system also varies nonlinearly with respect to the input field. Specifically, it is the polarization, $\tilde{P}(t)$, (dipole moment per unit volume) that varies with respect to the strength of the applied optical electric field, $\tilde{E}(t)$. In nonlinear optics, the polarization relationship to the electric field is not a linear series as with linear optics, but instead it is a power series:

$$\tilde{P}(t) = \epsilon_0\chi^{(1)}\tilde{E}(t) + \epsilon_0\chi^{(2)}\tilde{E}^2(t) + \epsilon_0\chi^{(3)}\tilde{E}^3(t) + \cdots + \epsilon_0\chi^{(n)}\tilde{E}^n(t)$$
$$\equiv \tilde{P}^{(1)}(t) + \widetilde{P^{(2)}}(t) + \widetilde{P^{(3)}}(t) + \cdots \tilde{P}^{(n)}(t)$$

(1)

Where ϵ_0 is the permittivity of free space and $\chi^{(n)}$ is the susceptibility. Equation (1) is the basis for calculating the polarization effect when large optical intensities are present.

When the optical field intensity is high enough, the additional terms in this power series are increasingly responsible for the generation of nonlinear effects including two photon excitation fluorescence, second and third harmonic generation (or even n-harmonic generation with high enough intensities), sum and difference frequency generation, intensity dependant refractive indices, optical parametric oscillation, saturable absorption and stimulated Raman effects (which includes CARS). These nonlinear effects generate new components of the electric field. The nonlinear response of the oscillation of the dipole moment of each atom is responsible for the generation of new frequencies. As nonlinear materials are not simply single atoms, each dipole moment influences its neighboring dipole moment creating a cascading effect when the orientation of each atomic dipole is in line with each other. The time varying polarization is responsible for these generated frequencies and modifications of the refractive index. Without going into a lengthy derivation (from Maxwell's equations), the typical wave equation of a nonlinear medium is:

$$\nabla^2\tilde{E} - \left[\frac{n^2}{c^2}\right]\left[\frac{\partial^2\tilde{E}}{\partial t^2}\right] = \left[\frac{1}{\epsilon_0 c^2}\right]\left[\frac{\partial^2\tilde{P}^{NL}}{\partial t^2}\right]$$

(2)

As mentioned previously, the variable that modifies the properties of the generated electric field is the nonlinear polarization term, $\tilde{P}^{NL}$, which varies depending on the conditions of the input wave, selected material and orientation. Various specific nonlinear polarization terms will be derived in the following sections, with the

general nonlinear polarization contribution for the second and third order nonlinear susceptibilities being given as:

$$\tilde{P}^{(2)} = \epsilon_0 \chi^{(2)} E^2 \quad (3)$$

$$\tilde{P}^{(3)} = \epsilon_0 \chi^{(3)} E^3 \quad (4)$$

2.3 Parametric VS Nonparametric Processes

An important basic concept of nonlinear optics is the comprehension of the different absorption-emission processes, of which there are two. Not all absorbed photons create equal electronic transitions, depending on the nonlinear process being exploited. This is significant, as wavelength of the emitted photons can vary depending on whether or not the process is parametric or nonparametric. A parametric process is defined as having the same initial and final quantum mechanical states. The energy of a photon that is absorbed parametrically by an electron is only contained in virtual levels. This means that there is no time for any residual energy to be transferred to phonon generation. A consequence of not having any interaction with real energy levels is that phase matching must be attended to closely. The lack of vibrational energy transfer is because the lifetime of electrons in virtual levels is much less (essentially instantaneous) than their brethren in excited eigenstates, which is where nonparametric electrons are found. As the energy of excited electrons can be transferred to the material lattice, when the excited electron eventually decays back down to the ground state, the emitted photon will have less energy, and be red shifted. This is in contrast to parametric processes, where there is no energy transfer and the emitted photon has exactly the same energy as that which excited the whole process. Understanding which nonlinear process is being exploited is critical to detection (specifically in filter selection), as the amount of energy deposited into the sample for a nonparametric

process can be significant enough to shift the wavelengths of the photons by many nanometers when compared to a parametric process [10]. This heating can also potentially damage a sample being imaged.

2.4 Second Order Nonlinear Processes: Second Harmonic Generation

SHG is a second order nonlinear process that involves the absorption of two photons of equal wavelength, and the emission of a blue shifted photon $(2\omega = \omega + \omega)$. In SHG, instead of populating real levels, SHG electrons find themselves utilizing virtual states, with the destruction of the two incoming photons, and the creation of the emitted photon happening instantaneously in a single quantum mechanical process. The excitation of a SHG process is depicted in Figure 7.

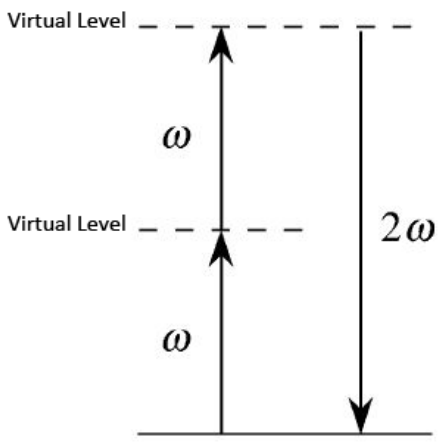

Figure 7: SHG energy level diagram [10]

To understand SHG, take the input electric field strength as:

$$\tilde{E}(t) = Ee^{-i\omega t} + c.c. \quad (5)$$

The induced nonlinear polarization of a material is given as a sum of the product of n nonlinear optical susceptibilities and the corresponding field strength. Specifically for SHG the induced nonlinear polarization for a material that is $\chi^{(2)}$ active is:

$$\tilde{P}^{(2)}(t) = \epsilon_0 \chi^{(2)} \tilde{E}^2(t)$$

(6)

Expanding this term in equation (6), the created polarization is a function of two terms that result in distinctly different results:

$$\tilde{P}^{(2)}(t) = 2\epsilon_0 \chi^{(2)} E E^* + \left(\epsilon_0 \chi^{(2)} E^2 e^{-i2\omega t} + c.c\right)$$

(7)

The first term does not contribute to the generation of the second harmonic, but instead causes optical rectification across the material surface. The reason for this is that the second time derivative is equal to zero. This means that there is an average DC polarization created across the material. The second term is what contributes to the generation of the 2ω photons [10].

2.5 Third Order Nonlinear Processes:

Not only can the exoscope exploit second order nonlinearities, it can also make use of third order processes. These include the more simple modalities such as two photon absorption, and potentially third harmonic generation as well as CARS. In the following section, we will examine the mechanics behind the generation of these third order nonlinear processes.

2.5.1 Two Photon Excitation Fluorescence

One of the simplest examples of a third order nonlinear process is two photon excitation fluorescence. Like many other nonlinear processes, TPEF benefits when compared to linear processes like single photon fluorescence. Instead of a single photon stimulating an atomic transition, the energy of two photons is simultaneously absorbed. Typically either light in the ultraviolet spectrum or in the blue/green region would be used. Instead, low frequency photons (typically in the infrared spectral range) can be used to promote electrons to a real excited state. A single photon of the same frequency would not have the required energy to bridge

the band gap. Two photon absorption can also be useful if the excited state is not connected to the ground state in a single photon absorption transition. As this transition involves a real state it is a nonparametric process with lifetimes allowing for some vibrational energy transfer before decaying back to the ground state. The excitation processes of a TPEF event is shown in Figure 8 [11].

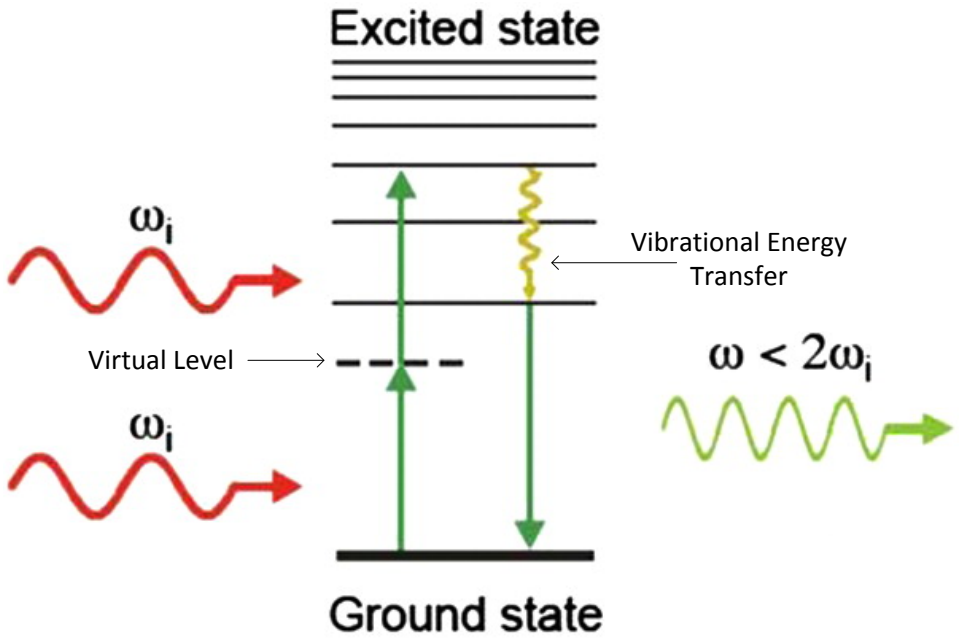

Figure 8: TPEF energy level diagram [11]

The emitted photon during this process will have slightly less than twice the energy of the incoming photons due to the nature of electrons residing in real energy levels. The population of real levels allows for phonons to be created, and energy lost through molecular vibrations.

2.5.2 Third Order Nonlinear Processes: Third Harmonic Generation

Not surprisingly, THG is the destruction of three photons of equal frequency (ω), and the simultaneous creation of a photon three times the frequency (3ω) of the incident photon. Similarly to SHG, the energy levels involved in the transition are virtual. A significant difference is that noncentrosymmetric as well as centrosymmetric materials can be THG active. In order to derive the THG

polarization equation, an assumption of a monochromatic ω is made, and that the electric field is given as a sinusoidal input wave.

$$E = E_1 \cos(\omega t) \tag{8}$$

Now when equation (8) is substituted into the third order nonlinear polarization equation, the result is:

$$\tilde{P}^{(3)} = \chi^{(3)} \epsilon_0 E_1^3 \cos^3(\omega t) \tag{9}$$

Using a $\cos^3 x$ trig identity:

$$\tilde{P}^{(3)} = \chi^{(3)} \epsilon_0 E_1^3 \left[\frac{1}{4}\cos(3\omega t) + \frac{3}{4}\cos(\omega t)\right] \tag{10}$$

Note the $3\omega_1$ in the first term of equation (10), it is responsible for generating the THG signal. While the exoscope created for this thesis has not demonstrated sufficient intensity, or been designed to generate or capture a THG signal, it is conceivable that a future iteration could be designed to incorporate THG imaging capabilities.

2.5.3 Third Order Nonlinear Processes: Analysis of Coherent Anti-Stokes Raman Scattering and its Raman Roots

The core functionality of this device is centred on CARS. In order to fully understand how CARS works, a description of a standard Raman process is needed. The following paragraphs introduce Raman scattering, the difference between Stokes and anti-Stokes generated photons, as well as the molecular vibrational modes that are be responsible for these spectral shifts. This Raman process is fundamental to CARS, and can be resonantly excited. Examples of a molecular bond that can be resonantly excited are C-H bonds. Lipids are prime examples of a tissue that is rich in C-H bonds, and is extremely sensitive to CARS microscopy. In-depth analysis of the

generation mechanics of CARS, and why lipids are such a good match for this modality are given in the following text.

2.5.3. 1 Raman Scattering

The recipient of the Nobel Prize for Physics in 1930 was Sir Chandrasekhara Venkata Raman. He was awarded this honour due to his discovery that when photons of a specific wavelength pass through a material, an extremely small number of these photons change wavelengths [12]. Previous to this discovery, it was thought that photons would only interact with matter by scattering elastically, as seen with Raleigh scattering, or by complete absorption causing an electronic transition.

There are two relevant methods in which a photon can be inelastically scattered while temporarily interacting with phonons present in the material structure: The first method is such that the energy from the incident photon is transferred to the vibrations of the atomic structure of the material, losing energy as it passes through the material. The resulting photon is red shifted, or Stokes scattered. The second method of inelastic scattering occurs when the opposite energy transfer occurs. The incident photon acquires energy from the molecular vibrations of the atomic structure. Figure 9 [13] depicts the energy bands and associated spectrum of both Stokes and anti-Stokes scattered photons as well as the elastically scattered Rayleigh photons. The resultant photon is now blue shifted, or anti-Stokes scattered [14].

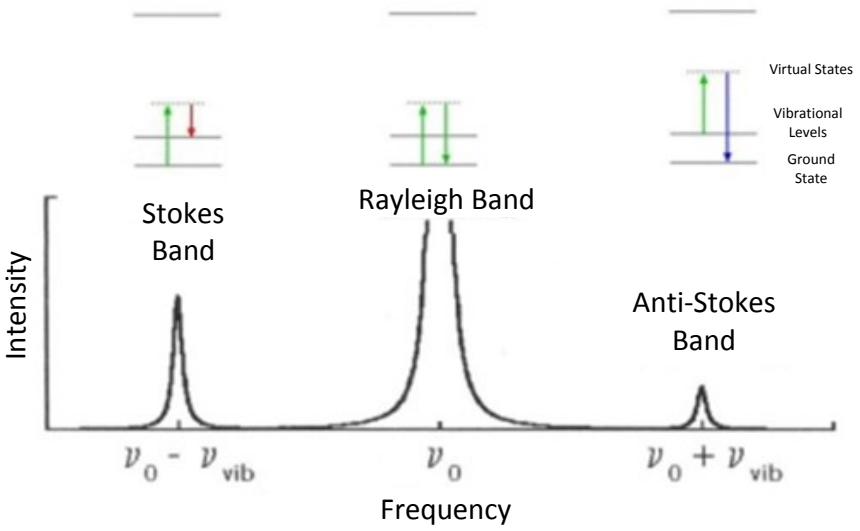

Figure 9: Rayleigh scattering frequency with the Stokes and anti-Stokes sidebands [14]

The energy difference of these scattered photons is equal to the molecular vibrational energy of the material being examined. It is also significant to note that different chemical bonds present in a molecule all have distinct vibrational energies. In general, a molecule with n number of atoms has a number of resonant vibrational frequencies equal to 3n-6 (unless the molecule is linear, not permitting the observations of axial rotations. This specific number of vibrations is represented by 3n-5). The simplest types of vibrations that can be found in atomic systems are shown in Figure 10 [15].

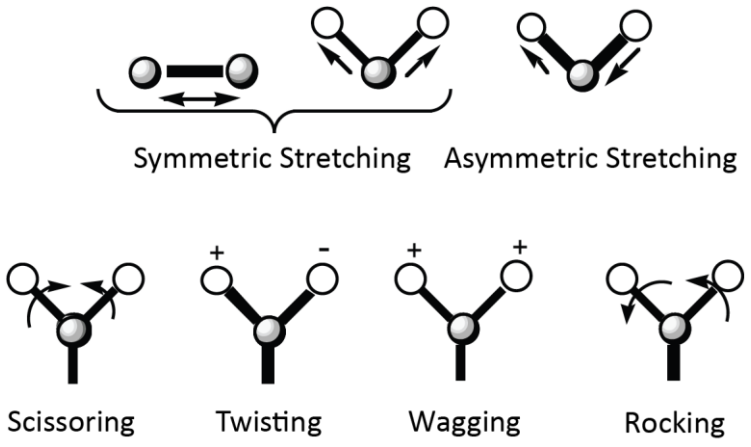

Figure 10: Types of molecular vibrations [15]

The frequencies of these resonant vibrations can span from low frequency twisting and bending modes at energies of about 100 cm^{-1}, to the high energies near 3500 cm^{-1} of stretching modes. The larger molecules give significantly more complex spectra. The fingerprints of these bond specific vibrational energies can be observed by infrared (IR) spectroscopy as well, but there are many differences between these two spectroscopic techniques. The main limiting factor of using IR spectroscopy in biological imaging is due to the high absorption in water of IR and far IR photons, where wavelengths typically used in Raman spectroscopy can be at the minimum of the water absorption window (400-500 nm). This means that samples probed with Raman spectroscopy can be kept in an aqueous medium, while IR spectroscopy is not suitable for in vivo biological imaging.

Based on these observations, the power of a Raman scattered photon is incredibly apparent: Raman photons could be used to identify the chemical properties of an unknown material or differentiate between biological structures, accomplished without the need for staining, vaporization or other chemical addition. All of these processes could potentially damage the sample being observed. If Raman spectroscopy could be applied to imaging live cells, much information could be determined about cell dynamics, structure and reaction to external stimulus. Raman, being the weak effect that it is, would require either very high laser powers (possibly damaging the specimen) or very high acquisition times (in which the live cell could be in motion causing significant blurring). If the sample has any innate autofluorescence (which is typically orders of magnitude stronger than the Raman effect), it will overwhelm any Raman photons that are generated. Fortunately there is a way to resonantly excite this Raman process.

2.5.3.2 Coherent Anti-Stokes Raman Scattering

Coherent anti-Stokes Raman scattering is a powerful imaging modality that is a slight modification of Raman's spectroscopic effect. As was mentioned in the previous section, Raman scattered photons are a rare occurring phenomenon. If the intensity

of an electric field is high enough, nonlinear effects can be induced on a sample, greatly increasing the Raman response. CARS is a third order nonlinearity involving real electronic molecular transitions. This means that the process is resonant, unlike a typical Raman transition. The stimulation of these high intensity photons actually induces the vibrations of all molecules in the focal region to be in phase with each other. The increase in Raman response caused by the high intensity optical fields has a nonlinear dependency on the input power. The intensity of the Raman signal is now tunable based on the input laser power, which is the key fundamental property of CARS.

Specifically, the generation of the Raman signal requires three photons, two of which have the same frequency (ν_1), the third (ν_2) is tuned to the vibrational energy difference of the molecular vibration being probed (ν_R), given by the following equation:

$$\nu_R = \nu_1 - \nu_2 \quad (11)$$

Now that a resonant frequency is established, an explanation of the order of photon interaction will be given. First a pump photon of frequency ν_1 is absorbed by the system. This photon resides in a virtual state until a photon of frequency ν_2 is incident upon the system. This photon stimulates the emission of another photon of equal frequency, causing an electronic decay to the ground state. The energy of this electron is not, however, at the same level as when is started. It has gained some vibrational energy equal to ν_R, due to the energy difference of the second photon. Before this electron can lose this additional energy, another photon of frequency ν_1 is absorbed promoting the electron up to another virtual level. The electron then decays back to the ground state, emitting an anti-Stokes photon of frequency ν_{AS}. This process is described by the subsequent equation and the energy level diagram and process shown in Figure 11 [10]:

$$\nu_{AS} = 2\nu_1 - \nu_2$$

(12)

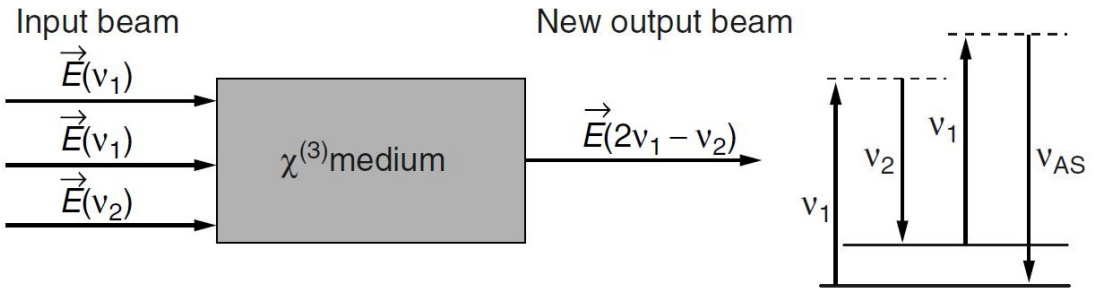

Figure 11: Photon interaction and energy level diagram for a CARS process [10]

It is evident that the anti-Stokes photon generated is spectrally distinct from both pump and Stokes input photons. These input photons can be filtered, leaving only the anti-Stokes photon to be captured. Now that a basic understanding of CARS has been given from a photon absorption perspective, a concise mathematical analysis will be done.

In order for a CARS signal to be generated, two laser beams at frequency ω_1 and $\omega_2 < \omega_1$ must interact. Mathematically, this gives rise to a specific nonlinear four-wave mixing susceptibility that leads to the generation of an anti-Stokes photon at frequency $2\omega_1 - \omega_2$ (whose complete derivation is outside of the scope of this thesis):

$$\chi_F^{(3)}(\omega_a = \omega_1 - \omega_2 + \omega_1) = \frac{-\left(\frac{\epsilon_0 N}{6m\omega_\nu}\right)\left(\frac{\partial\alpha}{\partial q}\right)_0^2}{[(\omega_1 - \omega_2) - \omega_\nu] + i\gamma}$$

(13)

Where ω_a is the anti-Stokes generated frequency, N is the number density of molecules, $\frac{\partial\alpha}{\partial q}$ is the change of the polarizability of a molecule with respect to the internuclear distance, ω_ν is the inherent resonant molecular frequency and γ is the damping constant. A nonlinear response occurs in the system when $\omega_1 - \omega_2$ is

equal to the molecular resonant frequency ω_v. This identity is the basis of why CARS is a useful tool for molecular imaging. Much like in standard Raman spectroscopy, the fact that molecular vibrations are indicative of the actual type molecule itself, CARS can resonantly excite these vibrations. CARS can accurately differentiate between regions containing the molecule being probed and those where there is an absence of the specific molecule, as the laser focal point scans from one region to the next.

A very suitable type of tissue for CARS imaging are lipids. Lipids contain high concentrations of C-H bonds, and consequently generate considerable CARS photons, with high contrast. The molecular vibration (stretching mode) of the C-H bonds can be resonantly excited when it equals the difference between the pump and the Stokes wavelengths. Since the contrast is based on the intrinsic vibrational properties of the molecule itself, there is no need to add any exogenous fluorophores or tags. This can allow viewing of dynamic cellular processes, with high time resolution. Lipid droplets are frequently imaged by CARS microscopes, since they are primarily made of triglycerides and sterol esters, which typically have a high concentration of C-H bonds. In addition to imaging cellular lipid droplets, CARS is exceptionally good at imaging myelin. Myelin is largely composed of 70-80% lipids which, as mentioned previously, typically contain a high concentration of C-H bonds.

There are different types of CARS that offer their own specific advantages, while the fundamental anti-Stokes wavelength generation mechanism remains unchanged. Femtosecond CARS denotes the use of a femtosecond, transform limited pump and stokes beam. This setup offers the highest possible peak powers, and consequently the most intently generated CARS signals. If peak powers are high enough, this can actually lead to an increase in the generation of nonresonant CARS background. This is simply due to the fact that the spectrum of femtosecond pulses (hundreds of cm^{-1}) is much larger than that of the Raman band being probed (~10 cm^{-1}). The only way to reduce the bandwidth of the laser pulse is to increase the pulse width. This results in lower peak powers, but also reduces the nonresonant background. This was

actually found to increase the signal-to-background ratio. Cheng et al. showed that using a 2-3 ps pump laser source was actually the optimal pulse width to maximize the signal-to-background ratio [16].

It is possible to combine the advantages of both picosecond, and femtosecond CARS. This can be accomplished by keeping either the pump or stokes as a femtosecond pulse, while broadening the pulse width of the other to the picosecond regime (called the probe pulse), this is called multiplex CARS, demonstrated in Figure 12 [17]. Since the spectral overlap is defined by the narrow bandwidth probe pulse, the spectral regions of the femtosecond pulse that don't overlap with the picosecond pulse don't generate a nonlinear signal. This reduces the background CARS signal, while one beam still has high peak intensities. The region of spectral overlap can also be tuned to resonantly excite other molecular vibrational modes. The pulse widths that we use in the exoscope setup can exploit the multiplex CARS advantages, as a femtosecond pump, and a picosecond Stokes are used.

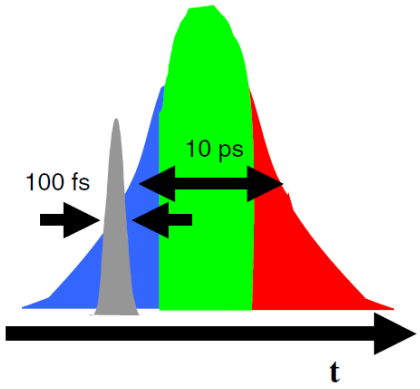

Figure 12: Depiction of the spectral envelope of a picosecond pulse interacting with a femtosecond pulse in multiplexed CARS [17]

2.6 Generation of the 1030 nm Stokes Beam

This section describes a nonlinear process that is related to imaging indirectly. This is a complex nonlinearity that is used to create a spectrum of white light from a photonic crystal fibre (PCF) in which the 1040 nm Stokes beam is picked from. This supercontinuum (SC) allows only a single laser source to be used for CARS imaging.

The phenomenon of supercontinuum generation was first experimented with in the 1970s by Alfano and Shapiro in borosilicate glass. They focused a picosecond pulsed, frequency-doubled neodymium:glass laser into a small piece of silica and were able to successfully generate a white continuum from 400-700 nm albeit with very high pulse energies (5 mJ). This work progressed from bulk material to silica fibres as the propagation distance could be very long and confinement area was extremely small thus increasing the interaction length, and the opportunity for the nonlinear processes to create the spectral pulse broadening. A diagram of the spectrum of an ultrafast pulse as its propagating throughout a PCF is shown in Figure 13 [18].

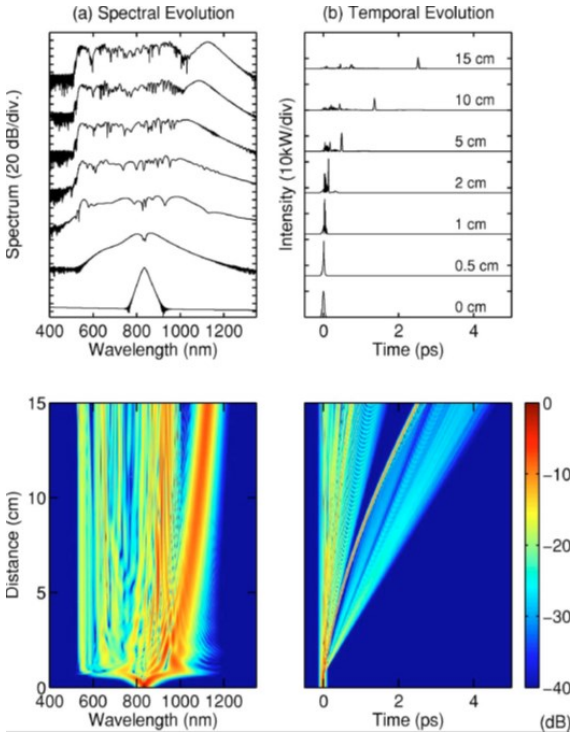

Figure 13: Temporal and spectral evolution of an ultrafast pulse propagating through a PCF [18]

Typically, the SC generation process starts with a femtosecond pulse that is considered a high order soliton. The pulse's spectrum rapidly broadens, usually forming two asymmetric peaks on either side of the pump centre. This high order soliton then breaks down and fissions into its fundamental solitons. The SC spectra generated in PCFs does not reflect only the profiles of individual soliton fission (as this would be represented by multiple distinct peaks), but instead has a flatter

profile. SPM can become the dominant SC generating effect as the envelope of light moves further away from the zero-dispersion wavelength (ZDW).

Cross-phase modulation offers up similar broadening characteristics as SPM, but instead of the frequency shift being self-induced, it is an external field that drives this variation. Instead of two pump photons mixing together, a pump and, say another photon generated by the initial four-wave mixing (FWM) process (or via a myriad of other processes) can interact producing additional frequency components. This essentially creates a cascading generation of new frequencies as long as phase matching is maintained.

Stimulated Raman scattering is yet another avenue for the red-shifting of the SC photons, the mechanics of which will be discussed in the following chapter.

2.7 Conclusion

Based on the preceding text, it is evident that in order to perform imaging with chemical specificity, a single photon based system is impossible to use for live tissue. Nonlinear microscopy achieves this chemical specificity without the need for exogenous dyes, while keeping the excitation-emission wavelengths spectrally distinct for ease of filtration. Tissue damage is also kept at a low level because of the small or even non-existent energy transfer to the sample. Z-sectioning is achieved since the nonlinear signal is only generated within a small focal volume. The mechanics behind each type of nonlinear processes have been discussed, with emphasis how $\chi^{(2)}$ and $\chi^{(3)}$ affect the polarization state of a material system, as well as the significant difference between parametric and nonparametric processes. A background of Raman scattering has been given, with the critical details of how CARS photons are generated. The information presented allows the selection of samples imaged in the following section.

While not all nonlinear processes have been discussed in detail, all nonlinear processes that are relevant to the exoscope have been addressed. Based on the information contained within the previous text; it is obvious as to why nonlinear microscopy offers significant advantages over linear microscopy. What might not be quite so obvious, is actually how to implement the nonlinear modalities. The topic of the following chapter is how these nonlinear processes have been applied to imaging, and how to overcome the difficulties working with high peak power pulses.

Chapter 3

CARS Endoscopy: The Advancement and Miniaturization of CARS Imaging, Component Selection, and Anticipated Performance

The following chapter will disclose the enabling technology related to the miniaturization of a CARS microscope. It is important to note that this is not an extensive investigation into the history of all CARS-related discoveries, but includes only a review of milestones that are pertinent to this thesis. Specific emphasis will be placed on the analysis of the individual components that make up the exoscope. Finally, the theoretical performance of the exoscope will be calculated, including the anticipated axial and lateral resolutions.

3.1 CARS: From Spectroscopy to Imaging

CARS had been demonstrated as a successful tool to enhance Raman scattering in spectroscopic applications, such as gas jet [19] and flame [20] molecular composition studies as early as 1973, although limited to a resolution of about 20 µm. This resolution limit has little negative effect on spectroscopic studies. In fact CARS is well suited to perform chemical composition studies of uniform samples. It wasn't until almost a decade later that this resolution limit was improved upon, and CARS as a contrast mechanism was applied to imaging biological tissues [21]. The system used an argon-ion mode-locked laser to pump two different dye lasers. The first laser contained a rhodamine 6G dye, with a tuneable output between 565-620 nm, with 250 mW of available average power, while maintaining a 6 ps pulse at 80 MHz. The second laser contained a 4-(dicyanomethylene)-2-methyl-6-(para-dimethylaminostyryl)-4H-pyran dye, was tunable between 620-700 nm, and produced 150 mW of average power while maintaining an 8 ps pulse width at 80 MHz. The use of lasers within the visible spectrum produced the first published images using CARS shown in Figure 14 [21], despite the high non-resonant

background signal produced as a consequence of using visible light. It is also important to note that the pump and stokes were not collinear. This cross-beam geometry overlapped in a very small portion of the focal volume of each beam, resulting in low spatial resolution, poor phase matching conditions and consequently low sensitivity.

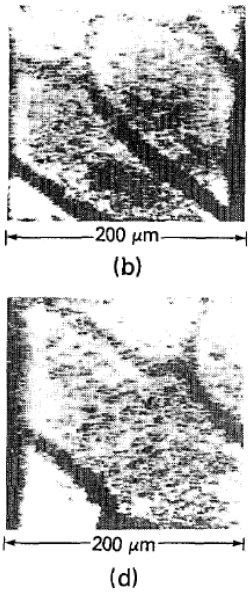

Figure 14: CARS images of D_2O soaked onion-skin cells, with the lasers are tuned to resonantly excite the 2450 cm^{-1} band of the D_2O [21].

The second major publication centred on CARS as an imaging modality was primarily an attempt to reduce the non-resonant background that plagued the sensitivity of the previous CARS setup. This was accomplished by Zumbush et al. by using near infrared wavelengths to stimulate the CARS process. The reduction in energy per photon of the longer wavelengths made exciting real energy levels less probable, reducing the occurrence of electron promotion to these levels. This work was based around a femtosecond Ti-sapphire laser tuned to 855 nm, which was split and a portion sent to an optical parametric oscillator which red shifted the wavelength to 1.1-1.2 μm. The difference in these wavelengths meant that bond energies from 2600-3300 cm^{-1} could be resonantly excited. Both wavelengths were overlapped temporally and spatially, and focused by a high NA (1.4, 60X) microscope objective

onto live bacteria (show in Figure 15), with the CARS signal being collected in the forward direction [22].

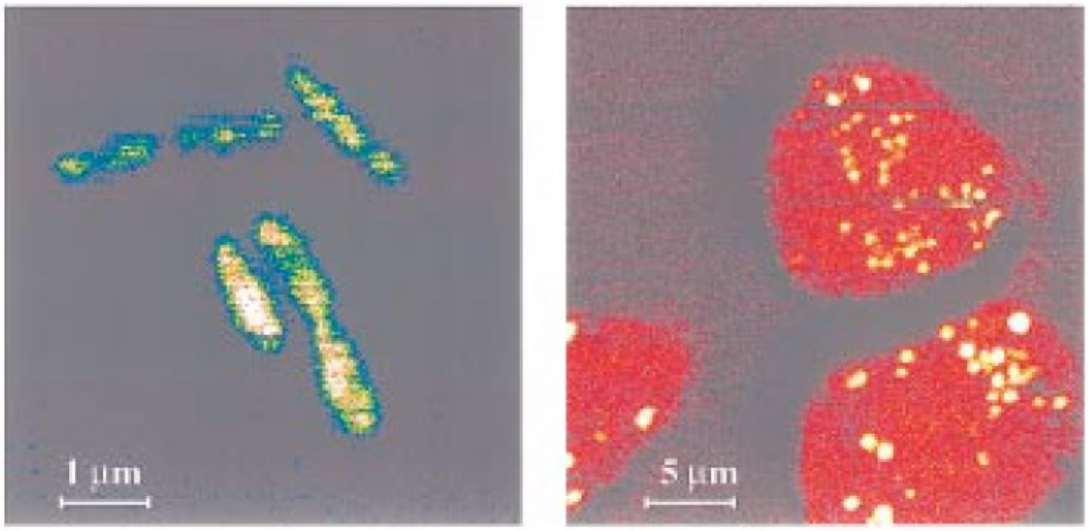

Figure 15: CARS images of unstained, live cells, including (a) Shewanella putrefaciens in D2O, with the Raman shift at 2878 cm-1 being resonantly driven and (b) HeLa cells. The bright regions are mitochondria rich in aliphatic C-H bonds at 2913 cm^{-1} [22].

The collinear optical geometry in conjunction with the high NA meant that phase matching conditions were more easily met (due to the larger cone of wave vectors, and small interaction volume), increasing the CARS sensitivity. The small interaction volume as a consequence of the use of a high NA objective also meant that 3D sectioning was made possible, further increasing the usefulness of this new imaging modality. The use of near infrared beams also had additional benefits, including lower photo-damage and a reduction of Rayleigh scattering, allowing deeper sample penetration.

One of the remarkable properties of CARS that was exploited by all previously mentioned discoveries is its coherent nature. This is in contrast to standard Raman scattering, as Raman photons are emitted in all directions. The generation mechanics of CARS and its coherent nature were discussed by Potma et al. in their 2000 paper. Specifically they investigated the intensity distribution of a CARS signal within a diffracted limited volume [23]. Further work was presented by Cheng et al.

in 2002. It was demonstrated that the radiation pattern of CARS photons is extremely dependant on the structure of the surrounding material, mainly the size and shape of the adjacent objects and environment, as well as the nonlinear susceptibility of the object itself. The object being imaged had a significant impact on whether or not the generated CARS signal would propagate in the forward, or epi direction [24]. If the sample being investigated is very thin, the radiation pattern is quite directional, and almost of equal magnitude in the forward versus the backward direction. As the sample increases in thickness, there is constructive interference in the forward direction (as the phase mismatch is reduced), and destructive interference in the backward direction (as the phase mismatch is large), reducing the available signal for epi-CARS [10]. Based on this observation, the generation of CARS photons in the epi direction would seem to be impossible with thick samples. There are, however, three mechanisms that allow for collection of photons in the backward direction. Cheng demonstrated the first, that when the size of the scattering object is small enough ($\lambda/3$), there is incomplete destructive interference in the backward direction [25]. The second source of epi-generated photons lies within discontinuities of the scattering object, specifically when $\chi^{(3)}$ changes rapidly, which was discussed in the paper on four-wave mixing in optical microscopy by Potma et al. in 2000 [23]. The final generation mechanism is not related to the coherent generation of photons, it in fact is simply backscattered forward-propagating CARS photons, scattered by differences in the refractive index of the material.

All three of these epi-generation mechanisms were demonstrated by Cheng et al. They were able to successfully collect CARS photons in the epi direction which is critical in the development of an endoscopic CARS microscope. Cheng used two picosecond, phase-locked Ti-sapphire lasers running at 80 MHz, one producing pump photons at 690-840 nm, while the other produced Stokes photons at 770-900 nm. The use of dual picosecond pulse trains meant that the system could resolve

sharper Raman spectral features, being able to distinguish between molecular bonds with closer vibrational energy signatures in the fingerprint region [25].

The previous work on advancing CARS microscopy techniques all require a significant amount of capital to be spent on laser systems. A single ultrafast laser is a costly piece of equipment, and a single source system could reduce the barrier to entry for CARS. Not only would this enable more laboratories to perform chemical specific imaging, but it also could bring CARS imaging closer to the bedside. Murugkar et al. addressed this challenge, developing a CARS microscope system requiring only a single source. In order to generate the second wavelength required for CARS, a PCF was used to generate a supercontinuum. Transform-limited, 800 nm light from a Ti-sapphire laser was split into two distinct arms, one for the pump and one focused into a PCF. This PCF had custom tailored dispersive properties, specifically two closely lying zero-dispersion wavelengths, situated on either side of the input 800 nm light. The generated output light was blue and red shifted, creating a supercontinuum with a peak at 1040 nm, suitable for use as the Stokes beam. The supercontinuum was filtered with a band-pass filter around the 1040 nm wavelength, and recombined with the pump beam and directed toward the sample. The temporally and spatially overlapped beams of light successfully resonantly excited the CARS process, resulting in the chemically specific images of unstained dorsal root rat axons shown in Figure 16 [26].

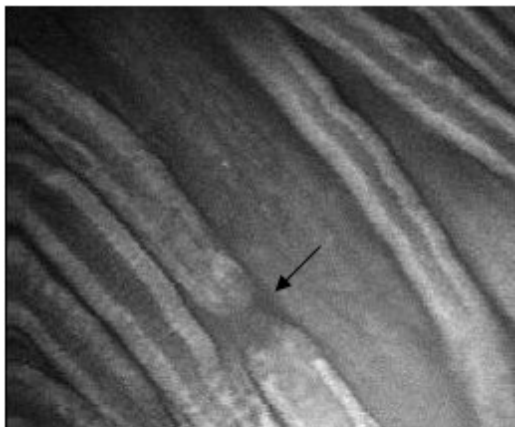

Figure 16: Mouse axons, with surrounding bright myelin, with a node of Ranvier denoted by the arrow [26].

3.2 Limitations of CARS

It would seem that the usefulness and applications of CARS as an imaging modality are endless, and while this is almost true, there are many reasons why the spread of CARS into mainstream medicine isn't as prolific as one might expect. Based on the previous section, it is evident that CARS has been successfully used in ex vivo experiments, although the transition to performing in vivo experiments is not an easy task. This is due to the many complications that arise when dealing with a dual-wavelength, nonlinear modality.

The most apparent difficulty that plagues CARS is the requirement for a pump and a Stokes beam to resonantly excite a Raman shift. Getting both of these beams to overlap both in space and time has proven to be quite a substantial obstacle. The fact that these wavelengths are separated by >200 nm means that chromatic aberrations mustn't be ignored if a detectable CARS signal is to be generated. The difficulty rises if an endoscopic CARS probe is being developed, as high NA miniaturized optics are famously susceptible to spherical aberrations. These aberrations can be dealt with if non-traditional components or specific care is given to the engineering of the optics.

Related to the overlapping of the two beams, the generation of said beams is also a main reason that CARS hasn't been deployed to the bedside. As CARS is a nonlinear process, high peak powers must be present in order to generate CARS photons. Traditionally, these peak powers are generated with the famous titanium sapphire laser. While this laser is the clear

choice for researchers, due to the high power availability, wavelength tunability, and adjustable pulse widths, its operation requires highly qualified personnel, and is incredibly bulky. Fibre lasers have begun addressing this issue, but CARS still remains in the laboratory.

Even if these fundamental difficulties are overcome, there are a few obstacles that will be present whether in the lab, or by the bedside. Unfortunately, a non-resonant background is ever-present. This background signal can overwhelm weak CARS signals, if there are a significant number of these off-resonance transitions. In some situations the signal to noise ratio can be increased by modifying the polarization. As CARS is a parametric process, phase matching conditions must be met. This can make detecting CARS photons from a biological sample quite tedious, as it introduces another variable that must be optimized. Typically, biological samples are much more difficult to image than a bulk sample, or microspheres. One of these reasons is due to the need to fix the samples in order to maintain their structural integrity over longer imaging periods. Through personal experimentation, it was determined that the standard fixation media can add additional FWM or two-photon signals, or even solubilize the lipids that are being probed. It is for this reason that careful consideration must be given to the selection, processing, and care of biological samples.

The final, and perhaps the most detrimental aspect to performing CARS imaging in the epi direction is the photon generation mechanics. As CARS is a coherent process, the majority of the photons propagate along the same vector as the excitation wavelengths. There typically is only constructive interference of CARS photons in the forward direction, except in a few cases. Interfaces (index of refraction changes) between objects and wavelength-sized objects do not have complete destructive interference in the backward direction, although this is not the most significant source of epi-generated photons. The majority of photons that propagate in the backward direction are mainly due to backscattered, forward propagating photons in thick samples. The consequence of these generation mechanics is a sharp reduction in the available photons for epi-detection; approximately only 10% of generated CARS signal is in the backward direction.

3.3 Miniaturized CARS Exoscope: Enabling Technologies and Overcoming Limitations

Now that the history and limitations of CARS imaging have been established, a brief description of the function of the major components of a nonlinear microscope system will be given as well as what components must be scaled in order to create a miniaturized version. The primary goal of this project is to enable in-vivo imaging of the spinal column tissue in a live rat.

The first component that all nonlinear microscopy systems must have is an ultrafast laser source. Ideally, the source has wavelength as well as pulse width tuneablility. This flexibility in the pulse width allows for fine control over the bandwidth of the stimulated Raman process. Wavelength tuneablility can vary the resonance frequency being probed, allowing alternative chemical bonds to be resonantly excited. As long as there is a method to deliver the ultrafast pulse train to a miniaturized microscope, the laser source does not have to be scaled down.

The second significant element in a microscopy system is the scanning assembly. Typically, benchtop microscopes utilize galvanometric scanners to steer the beam from one edge of the field of view to the other. It is imperative that the scanning system be decreased in size, as in a miniaturized probe the scanner is contained within the head of the endoscope itself.

Another significant component to a microscopy system is the focusing optics. Typically, a multi-element optic with diameter in excess of 1.27 cm is used for this purpose to minimize aberrations. The focusing system must be reduced in size in order to be included in a miniaturized microscope, while maintaining a high NA. A method to collect the generated photons must also be included in a benchtop system. Typically photons are focused either directly into a photomultiplier tube (PMT), or into a multi-mode fibre, and then sent to the PMT. The capture geometry

for a miniaturized system must include a multi-mode fibre, as the delocalization of the PMT allows for an even further reduction in size of the probe.

There is only one component that is unique to a portable miniaturized microscopy system. It is necessary due to the impossibility to deliver the pump wavelengths to a portable probe by free space optics. This hurdle is overcome by the use of fibre optics.

The discoveries that make all of these aforementioned miniaturizations possible are discussed in the following section. Details as to what components were chosen for the exoscope are also given, as well as the specific reasoning for selection.

3.3.1 Photon Delivery

3.3.1.1 Photonic Crystal Fibre Fundamentals

Nonlinear imaging is extremely sensitive to laser pulse duration. This is due to the fact that the amount of nonlinearly generated photons has a quadratic dependence on the intensity of the pump light. Therefore, it is ideal to have the pulse width at the sample to be as close to transform-limited as possible. In order to minimize the pulse width, it is important to understand why the pulse broadens in the first place. Performing a Fourier transform on a short pulse from the temporal domain to frequency spectrum generates a large frequency spread. This relationship dictates that the shorter the pulse, the more frequency components make up the pulse envelope [14]. It is known that the velocity of a wave travelling through a medium is wavelength dependant. This is caused by the wavelength dependence on the index of refraction of a material. In normally dispersive materials, the closer the wavelength to the absorption band of the material, the slower the wave travels [12]. This causes the high energy photons in a packet to lag behind the low energy photons and is what causes the significant GVD. If GVD is not compensated for, the nonlinear signal generated would be extremely weak, or not present at all.

Traditionally, all silica fibres are used to transport photons from one location to another, either over long distances or if the destination isn't fixed. In this case, the

exoscope will not have a fixed location; therefore free space beam delivery is out of the question. A delivery fibre must be used, and dispersive effects must be paid special attention. In standard single-mode silica fibre, the ZDW is at approximately 1310 nm, with the dispersion curve shown in Figure 17 [27]. This value is relatively constant for all silica fibres (this value can be modified slightly with the introduction of dopants). The wavelengths of interest for CARS are nowhere near the 1310 nm that would introduce little dispersion as the pulses propagate along the fibre. At either side of the ZDW, either Raman shifts, self-modulation, or soliton propagation are responsible for the modulation of the temporal profile of the propagating pulse. These effects, like the ZDW are also constant at specific wavelengths. If the ZDW point and the dispersion plot could be tailored, the temporal broadening effects on the pumping wavelengths could be diminished. Fortunately fibre fabrication techniques have led to developments in dispersion tailoring.

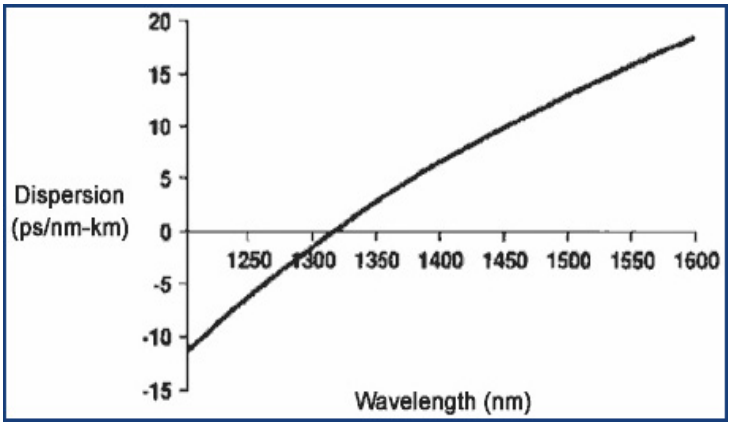

Figure 17: Dispersion profile of a standard SMF [27]

The fabrication process of standard step index telecom fibre has been perfected over the course of its thirty plus years in existence. This has given the ability for researchers to easily play with the physical structure of the fibres itself. If the refractive index difference between the core and the cladding could be achieved by creating a photonic band gap surrounding the core, instead of having slightly different glasses, the properties of the fibre could be altered to suit one's need. This idea was introduced in 1974 by Kaiser and Astle, but was not physically possible until

1996 after fibre drawing techniques had matured. This was a pivotal moment in fibre design, when PCFs were first created. PCFs are similar to normal fibres, but are made of a single type of glass, with periodic holes that run longitudinally along the fibre, with one air hole in the centre replaced with silica. This defect is the core, which causes a localized increase in refractive index (in comparison to the air-gap surrounding matrix) and allows for wave propagation through normal total internal reflection. An image of the first PCF used by Ranka et al from 2000 to produce broadband SC generation is shown in Figure 18 [28]. If the hole diameter, the pitch (distance from the centre of one hole to the adjacent) and even the packing structure of the fibre is altered, the resulting dispersive and wave guiding properties will change. The ZDW of these fibres can be shifted to the red or the blue or even creating more than one ZDW.

The ability to shift the ZDW of the delivery fibre isn't the only advantage of selecting a PCF for photon delivery. In order to maintain a high quality imaging system and diffraction limited focus, single-mode propagation is obligatory. With standard single-mode fibre (SMF), this single-mode confinement is achieved by keeping the core diameter low (<10 μm), and each fibre is only suited to propagate a discrete wavelength range. Now since the magnitude of the nonlinear effects suffered within the delivery fibre is intensity dependant, a larger core diameter would reduce these unwanted effects. As a result, the unique properties of PFCs can increase the core diameter while maintaining single-modality across all wavelengths for which fused silica is transparent. This is accomplished by engineering a cladding with a small air filling fraction resulting in a low index contrast fibre. The effective index of refraction that is experienced by the passing wave is modified based on the wavelength of light passing through the structure. For shorter wavelengths, the effective refractive index of the cladding shifts towards the normal refractive index of silica [29].

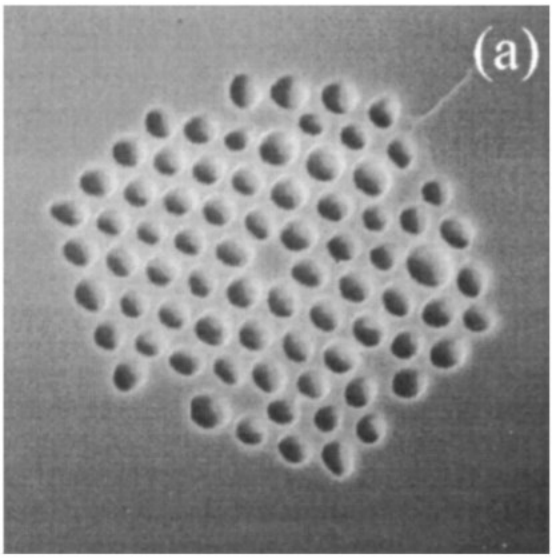

Figure 18: Scanning electron microscope image of the core and surrounding air-gap cladding matrix of a PCF [28]

3.3.1.2 Photonic Crystal Fibre applications in Endoscopy

Fibre optics have been widely used as an optical transmission medium for various types of microscopy, including confocal, fluorescent, optical coherence tomography, and other in vivo imaging applications. The inherent flexibility of fibres allows for the distribution, and collection of photons to areas not easily (or sometimes impossible) attained with free-space optics. The mobility associated with fibre delivered probes could have great impact on the functionality of CARS, enabling chemically selective, in vivo imaging of human patients. A significant amount of work has been performed on the development of a nonlinear endoscope for single modality imaging. A dual-clad photonic crystal fibre (DCPCF), gradient-index lens (GRIN) lens focusing as well as a 1D MEMS scanner has been combined to successfully image stained nucleic acids (TPEF) as well as the collagen from rat esophagus (SHG) [30]. This work was important in the development of a multimodal microscope, although does not address the challenges associated with working with a multi-wavelengths modality such as CARS.

The first attempts at obtaining a CARS image through means of fibre delivery was performed in 2006 by Evans et al. This work was performed as a proof of concept, to demonstrate that CARS images could be obtained through fibre delivery, in this case

an SMF. The laser source used was a passively mode-locked Nd:YVO_4, that put out 7 ps transform limited pulses at 1064 nm. The pump wavelength, generated by an OPO, was tunable between 780-920 nm, resulting in a 5 ps pulse width. The temporally broad pulses induced little spectral broadening effects within the 0.12 NA, 5.6 µm core diameter fibre. The SMF was coupled to a set of miniaturized optics, and the imaged polystyrene beads shown in Figure 19 were generated by the scanning of a three dimensional piezo stage [31].

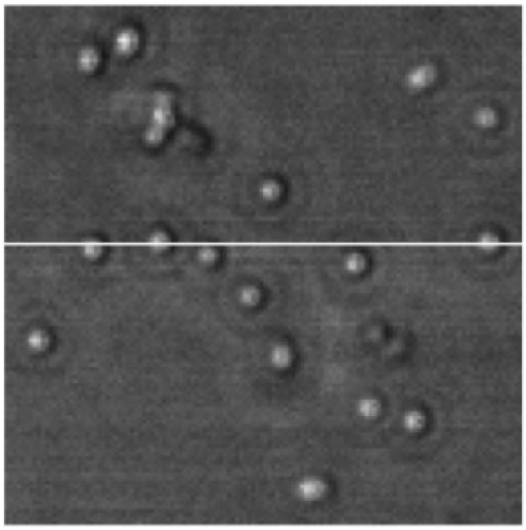

Figure 19: CARS image of polystyrene beads, with fibre delivered pump and Stokes beams [31]

In parallel, work was being performed with shorter pulse widths by Wang, et al. at Purdue University, investigated the differences between SMF, and PCF delivery. Specifically, they were trying to quantify the SPM and GVD effects generated by the propagation of these shorter pulses through the different delivery fibres. Their laser system consisted of two Ti-sapphire lasers that output 2 ps, and 3 ps pulses for the pump and stokes respectively. The trials were performed on two 1m long fibres: an SMF (NA=0.13) and a PCF (NA=0.05). While the 2 and 3 ps pulses suffered very little SPM and GVD while propagating through the PCF (<1% pulse broadening), a 200 fs pulse encountered significant spectral broadening, widening from 5 to 12 nm. Based on that observation, it is clear that in order to use femtosecond pulses, pre-

compensation must be done to counteract fibre generated nonlinearities. The SMF fibre also induced significant spectral broadening to the 2 ps pump pulse. Additional wings were produced in the autocorrelation trace, corresponding to a pulse width of 3.1ps. When the pump and Stokes beams were delivered by the SMF, the CARS intensity was only half of that when compared to the PCF delivered light [32]. This discovery is not surprising, although quantifying the reduction in CARS intensity was an important step in understanding the benefits of using PCFs as a photon delivery method. The use of PCFs in conjunction with picosecond pulses (although with macro optics) allowed Wang et al. to obtain the epi images of myelin shown in Figure 20.

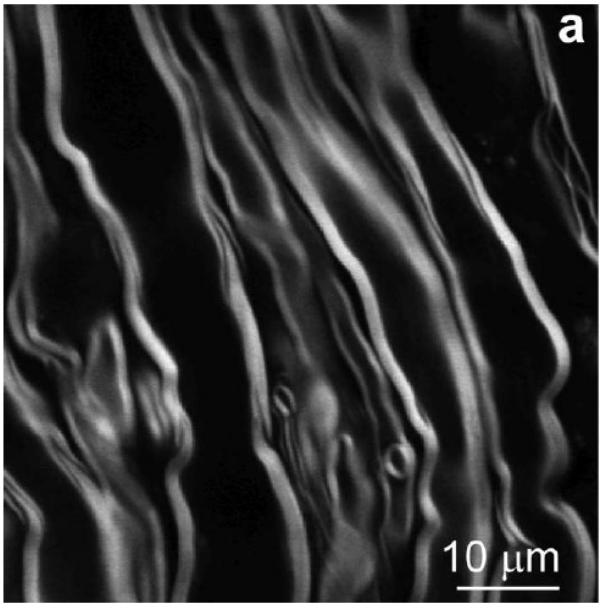

Figure 20: Bright strands of myelin, surrounding the dark axon of a neuron [32]

Spectral pulse broadening is not the only unwanted nonlinear effect generated within the delivery fibre. As the pump and Stokes beams are temporally and spatially overlapped within the fibre, FWM during propagation is possible, and was demonstrated by Balu et al. in their 2010 paper. Picosecond pulses in conjunction with PCFs (DCPCF-16 and LMA-20) were used for this experiment. Both pump and Stokes beams were temporally overlapped, and focused into the PCFs. An alarmingly

high anti-Stokes signal was observed. The fibre-generated FWM and CARS intensity from dimethyl sulfoxide are plotted in Figure 21 for the LMA-20.

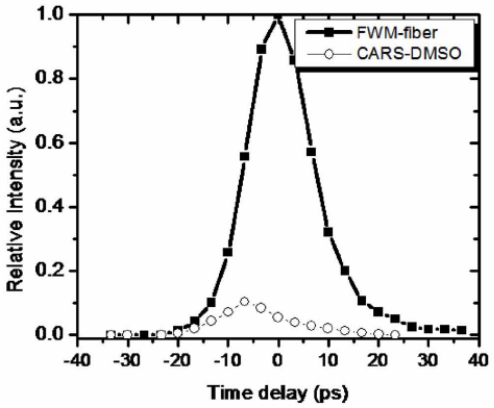

Figure 21: FWM signal generated within PCF delivery fibre (square) for comparison with the CARS signal obtained from DMSO (circle) [33]

It was theorized that the generation mechanism was not from phase-matched Raman mechanisms, but possibly by fibre impurities through stimulated Raman pumping, with incoherent anti-Stokes photons scattered by the pump beam [33]. This observation was critical to the design parameters of the exoscope, as the excitation and collection path must be kept discrete to avoid saturation of the CARS signal with the fibre-generated FWM.

3.3.1.3 In-Depth Analysis of the Implemented Fibre Delivery System

Choosing a fibre for the delivery of multiple wavelengths with high enough peak powers to induce nonlinear effects is not trivial. A fibre with a high operational threshold power must be single-mode for all wavelengths of operation, have low bending losses while maintaining a high coupling efficiency is critical. Two fibres were selected for preliminary investigation, a dual clad photonic crystal fibre (DCPCF), and a large mode area (LMA) fibre.

The DCPCF (NKT Photonics, Denmark) was the first fibre to undergo testing. A DCPCF is very similar to a regular PCF, with the exception of an additional cladding layer surrounding the traditional holey structure. The physical structure of a cross section image of the DCPCF used is demonstrated in Figure 22 [34] with the solid silica core

surrounded by the first cladding, a honeycomb-like lattice of air gaps. It is easy to observe the secondary cladding layer, the dark ring surrounding this entire waveguide structure. The cladding surrounding the solid core acts as a single-mode fibre for multiple wavelengths, while the secondary cladding and the rest of the internals act as a multimode fibre. It was proposed that this single fibre could be used as a delivery fibre for the pumping wavelengths, as well as a collection mechanism for the generated nonlinear photons.

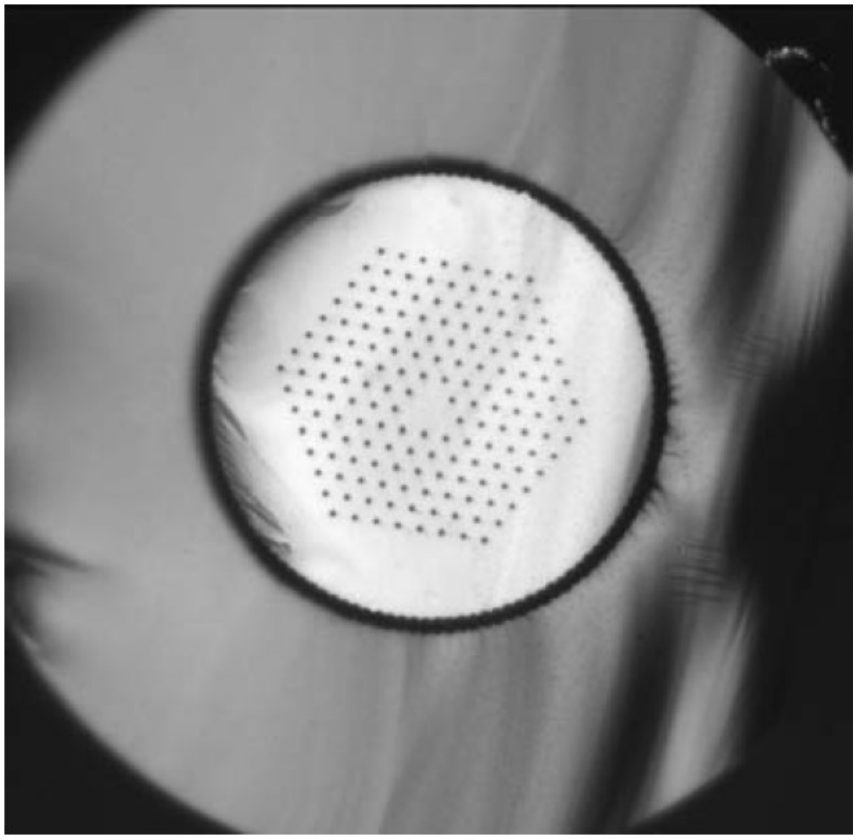

Figure 22: Microscope image of a DCPCF [34]

Utilizing this non-standard fibre introduced a new set of challenges. The large core and cladding diameter meant that telecom tools could not be used to prepare this fibre. Traditional stripping and cleaving methods could not be applied. An attempt to chemically strip the jacket with sulphuric acid was made, although this weakened the mechanical strength of the fibre, causing it to break easily. The complex structure of the multiple arrays of air holes also made it almost impossible to cleave

without shockwaves travelling through the silica, fracturing the delicate matrix of air holes. The fibre was sent to OZ Optics (Carp, Canada) to be terminated. The fibre tip was heated, collapsing and sealing the air holes, and end capped with a portion of solid silica. With both ends of the fibre cable terminated, attention was turned to dispersion compensation.

There are various methods used to compress ultrafast optical pulses, and the two that were focused on are prism compressors, and grating compressors. The end result of these two compression mechanisms are the same, but vary in implementation. Both function by supplying anomalous GVD. For a prism compressor this is accomplished by spectrally separating the beam of light by a standard prism, allowing the path length that each frequency of light travels to be altered. This spatial dispersion is thereby converted to temporal dispersion. Based on the geometry of the prism compressor, a positively chirped incoming beam can become negatively chirped, with the lower frequency components lagging behind the higher ones. A diagram of a four prism compressor setup and subsequently shorter optical pathway for the lower frequencies can be seen in Figure 23 [35]. This negatively chirped pulse can then be coupled to a normally dispersive element (such as a photonic crystal fibre), reversing the chirp that was introduced by the prism compressor. This method enables transform limited pulses immediately after travelling through a normally dispersive medium.

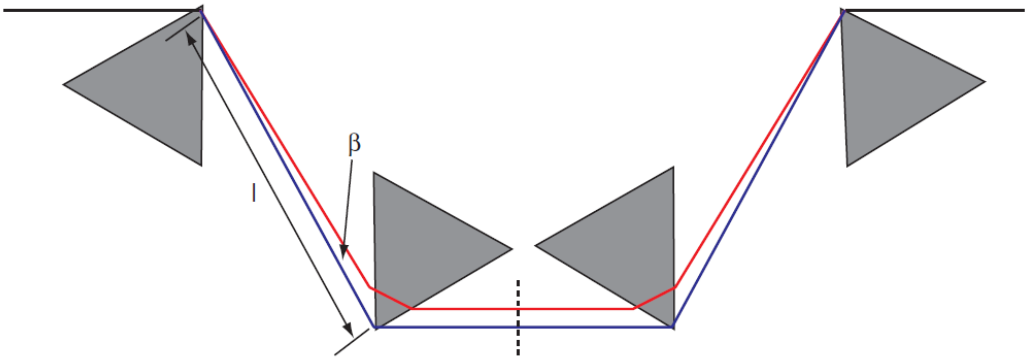

Figure 23: Typical prism compressor setup [35]

As mentioned previously, a grating compressor operates under the same principle as a prism compressor. Instead of using the effective refractive index change experienced by various wavelengths passing through a dispersive medium, the spectral diffusion is accomplished by the Huygens-Fresnel principle. Each periodic ruling on the grating can be treated as a point source. The reflected light will then either have constructive or destructive interference, with the reflection angle depending on the wavelength, and spacing of the rulings (as well as the reflected order of interest). This relationship is modeled by the following equation, when the incident light is normal to the grating surface:

$$d \sin \theta_m = m\lambda \tag{14}$$

This relationship causes longer wavelength light to have a smaller diffracted angle, while the shorter wavelength light has a larger diffracted angle. With the correct system geometry, this spatial dispersion can be transformed to temporal dispersion; two examples of this are depicted in Figure 24 [36].

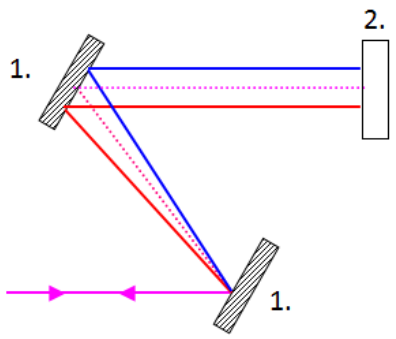

Figure 24: Typical grating compressor (1) Grating (2) Mirror [36]

Both prism compressors and grating compressors have their own set of advantages and disadvantages. While the grating compressor physically takes up less space per amount of chirp required, it also introduces more losses from the modes not captured by the second grating, reducing the available power for nonlinear imaging. Before any compressor setup can be selected or designed, the effective dispersion

introduced by the DCPCF must be measured. A 300 fs long, 26 mW of 800 nm pump light was focused into the DCPCF with a 10X microscope objective lens. The measured dispersion introduced by the DCPCF was 75000 fs^2, and the maximum dispersion that could be introduced by the prism compressor was measured to be 61000 fs^2. According to calculations, with a transform-limited input pulse, the output should have been 583 fs. This was not the case, as the autocorrelator measurements varied from 2.4-5.4 ps depending on coupling conditions. Due to the nature of the dual clad fibre; it wasn't possible to only couple the laser into the single-mode core. Inevitably, there was light coupled to the outer core, creating two effective dispersions, for which could not be compensated. As the exoscope was not designed to use the outer core, the DCPCF was placed aside, and attention was focused on the LMA-20 fibre (NKT Photonics, Denmark), as this fibre only had a large, single core facilitating simple dispersion compensation.

Figure 25 demonstrates the intensity cross section of the LMA-20 fibre of which the dispersive properties needed to be experimentally determined. An approximation of the dispersive properties is shown in Figure 26, demonstrating normal dispersion for both the 800 nm and 1030 nm wavelengths. 30 mW of the 300 fs long, 800 nm pump beam was focused into the LMA-20 by a 10X microscope objective lens. The output pulse width was measured with an autocorrelator, and determined to be 1.331 ps.

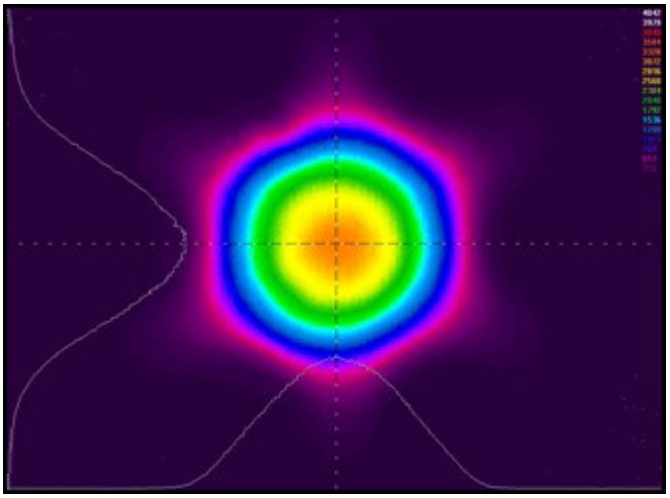

Figure 25: LMA-20 intensity distribution profile [37]

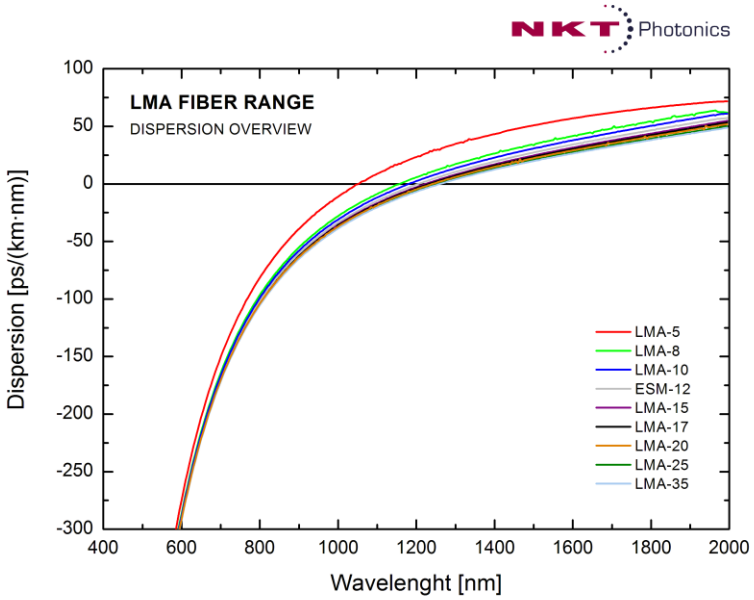

Figure 26: LMA20 dispersion profile (orange) [38]

The effective GVD was calculated using the following formula:

$$\beta^2 = \frac{(T')^2 - (T_0)^2}{7.69}(T_0)^2 \quad (15)$$

$$\therefore \beta = 37373.4\, fs^2$$

Where β_2 is the GVD, T' is the final pulse width in fs, T_0 is the input pulse width. The compressor system must compensate for both the dispersion of the fibre, as well as any other positively dispersive elements in the system. The resultant sum of all positively dispersive elements is:

$$\beta_{2_{system}} = 37373.4fs^2 + 8148fs^2$$

(16)

$$\therefore \beta_{2_{system}} = 45521.4fs^2$$

The compressor system must introduce anomalous dispersion equal to the normal dispersion created by all the optical elements contained within the GVD calculated. Due to size constraints on the optical bench, the use of a prism compressor was not possible. It was hypothesized that the amount of power reduction in a grating compressor system wouldn't be severe enough to hamper the creation of a CARS signal; therefore a grating compressor was chosen to modify the GVD of the pulse. The equation used to determine the group delay dispersion (GDD - which is the GVD per centimeter of grating separation) is as follows [39]:

$$\beta_2 = -\frac{\lambda^3}{2\pi c^2 d^2 \left[1 - \left(\frac{\lambda}{d} - sin\gamma\right)^2\right]^{\frac{3}{2}}}$$

(17)

$$\beta_2 = -12340\ fs^2/cm$$

Where λ is the input wavelength, c is the speed of light in a vacuum, d is the grating parameter representing the spacing of the rulings, and γ is the incident angle. To calculate the grating separation distance (X), a simple division of the GVD by the GDD is necessary.

$$X = \frac{45521.4fs^2}{12340\frac{fs^2}{cm}}$$

(18)

$$\therefore X = 3.69cm$$

With the grating separation distance set to approximately 3.69 cm, the separation was fine-tuned until a transform limited, 100 fs pulse out of the LMA-20 was acquired.

3.3.2 Optics

3.3.2.1 Literature Review of Focusing Systems

The reduction of aberrations in optics is crucial even for single wavelengths in attempting to resolve the smallest possible features. When a multi-wavelength imaging modality such as CARS is being performed, the chromatic aberrations create an even more substantial barrier to obtaining high quality images. If the input pump and Stokes wavelengths are not overlapping in space, a reduction of generated CARS photons will occur, possibly not creating a CARS signal at all depending on how severe is the overlap mismatch. The cause of these aberrations is due to the fact that the index of refraction in a material is wavelength dependent. When dealing with closely spaced wavelengths, as in a single photon fluorescence system, the slight aberrations affecting the system do not cause catastrophic failure. The large separation between the excitation wavelengths (>200 nm) means that effects of chromatic aberration must be taken into careful consideration. As this microscope is to be used as an epi photon collecting device, the wavelength of the collected photons must also be considered in the design. There are two plausible methods to accomplish this goal: a custom fabricated GRIN system, or a series of miniaturized optics. Both of these methods are well suited for a multimodal exoscope, with the GRIN lens offering a slight size advantage.

GRIN lenses were used in a 2006 paper by Fu et al. in conjunction with a DCPCF to perform TPEF, or SHG imaging [40]. The lack of a requirement to perform CARS imaging allowed Fu to use an off the shelf GRIN lens. The effects of chromatic aberrations were not as critical to these single wavelength modalities, as there was no need to overlap a pair of beams. In order to perform CARS with a GRIN lens,

careful consideration must be given to the design of the focusing optics. Saar et al. were responsible for pushing the limits of nonlinear endoscopy by developing a GRIN lens system used for CARS microscopy, although the size of the entire unit was still relatively large. In order to combat the inherent chromatic aberrations present with a single GRIN lens, their objective lens system was composed of a pair of GRIN lenses, with a diffractive optic sandwiched in between. The lens system had an NA of 0.3, a working distance of 150 µm and an outer diameter of 1.4 mm, capable of producing high quality images as demonstrated in Figure 27. This resulted in a lateral resolution of <2 µm, and an axial resolution of 6.5 µm [41]. The main difference between Saar's device and the exoscope developed for this thesis is the detector scheme. Saar's device included a sizeable 10x10 mm, on-device photodiode. This increased the dimensions of the probe significantly, rendering it quite unsuitable for insertion into any small cavity.

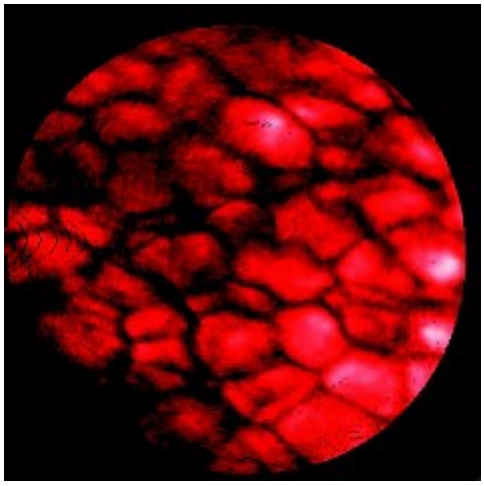

Figure 27: Surface enhanced Raman image of subcutaneous fat as demonstrated by Saar et al. [41]

The alternative to a GRIN lens system is simply a miniaturized objective, which was demonstrated by Wang et al. in 2006. Although the lens system employed was not ideal for the inclusion in an endoscope as the proximal end of the objective still included macroscopic lenses, the tip of the probe was a mere 1.3 mm, with a working distance of 200 µm. The quality of the lens system of the miniaturized

objective was not as high as the dual GRIN lens system mentioned previously in the axial resolution (11.4 μm), although it outperformed in the lateral resolution (0.86 μm). The miniaturized objective lens also was capable of producing high quality CARS images of rat myelin as demonstrated in Figure 28 [32].

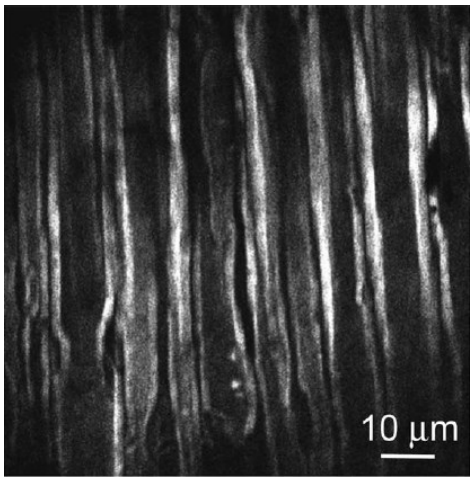

Figure 28: Epi-CARS image of rat myelin acquired by Wang et al. [32]

3.3.2.2 Implemented Focusing System

A miniaturized objective lens system was selected to focus the pump and Stokes beams. While slight performance gains could have been achieved with using an achromatic GRIN lens system, it was not worth the expense to have a custom GRIN setup made.

The exoscope design has a requirement that the distal end of must not have an outer diameter greater than 3 mm. This is based on the maximum size of the laminectomy that can be performed on the rat spinal cord. Based on this prerequisite, the internal optics of the exoscope could have a maximum diameter of 2 mm while still maintaining a high NA of 0.6 and a long enough working distance of 400 μm while still attaining sub-micron resolution.

Combatting chromatic aberrations with these tight geometrical constraints required careful consideration when designing and assembling the optics. The chosen design includes several lenses with varying focal lengths ranging from 3.0 mm BK7 glass for input light collimation down to a combination of SF4 and FK51 glass of 1.8 mm

diameter for a five times post-MEMS beam diameter expansion (to fill the back aperture of the focusing optics), for chromatic aberration correction at both pump wavelengths and sample focusing. All of these optical elements are coated with broadband anti-reflection coatings with a reflection of less than 1% over 652-1036 nm on both air/glass surfaces, the simulated reflectance charts can be seen in Figure 29.

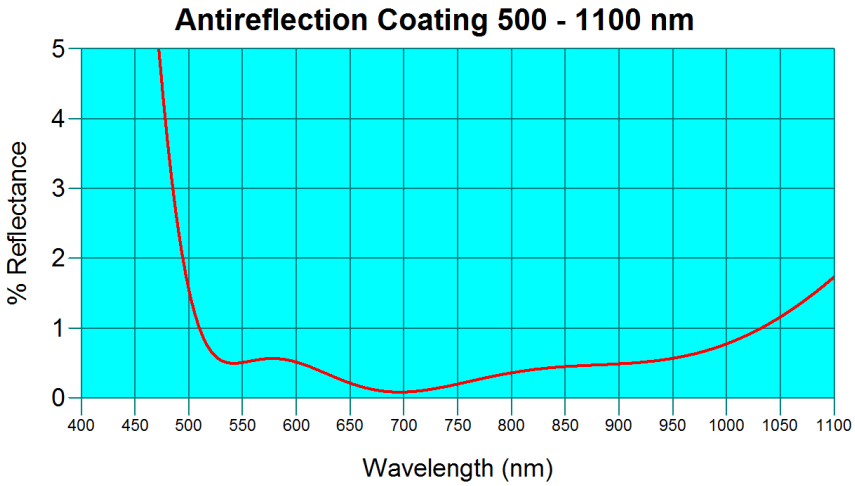

Figure 29: Coating deposited on all focusing optics in the exoscope

This low reflection per surface is made possible by a custom four layer deposition of alternating hafnium oxide and silicon dioxide. This entire optical system is capped off with a 100 µm glass window to protect the optics and allow for water/specimen immersion. Simulations that were performed on the optical system indicate that it will be a diffraction limited focus. The ray diagram of the entire system is shown in Figure 30.

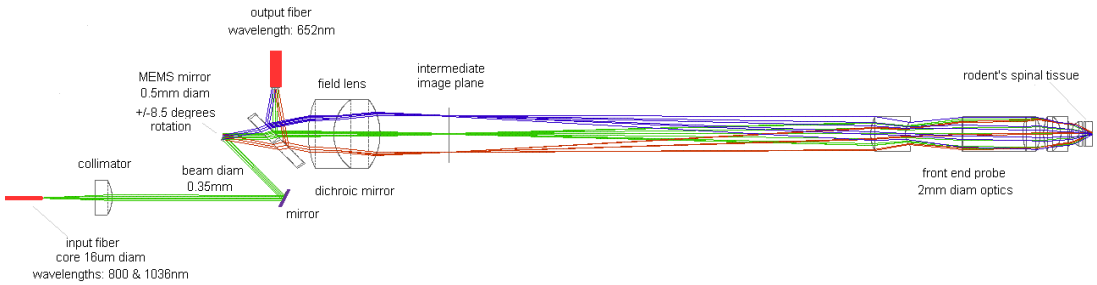

Figure 30: Internal ray diagram of the exoscope

3.3.3 Filter

Another crucial optical component is the dichroic mirror that allows the excitation light to be separated from the emitted light. Light destined for the PMT is reflected off of the dichroic mirror and focused into a multimode fibre, while the excitation wavelengths pass through unimpeded. This component is also critical to removing any anticipated four-wave mixing component that is generated within the delivery fibre, as mentioned previously [33]. A reflection of greater than 95% over a wavelength range of 400-700 nm and transmission of greater than 99% from 800-1036 nm is accomplished by more than 100 alternating layers of Ta_2O_5 and SiO_2, giving a total thickness of 8.849 µm (BMV Optical Technologies, Canada). The manufactured dichroic mirrors were tested at the optical assembly lab. At an incidence angle of 45°, the transmission of a 750 nm diode laser was experimentally determined to be 92.3%.

3.3.4 Scanning Mechanism

3.3.4.1 Literature Review of Scanning Systems

Photon delivery and concentration and optical filtration are only three of the four key elements in developing a miniaturized microscope. Developments and options in scanning methods and their application to nonlinear miniaturized microscopes have been investigated by many groups. The simplest method to scan and collect blue shifted photons is by moving the sample stage one step at a time. This is not a suitable technique to obtain video rate imaging, as current high-speed, high-precision scanning stages cannot cover the required 100x100 µm field of view with adequate refresh rates. This technique had been applied to early iterations of endoscopic probes [31] but merely used as a proof of concept for other aspects of miniaturized nonlinear imaging.

A possible candidate for in-vivo endoscopic applications is a fibre-mounted piezo tube actuator. This was the scanning method of choice for the GRIN lens system used by Saar et al. The delivery fibre was inserted into a miniature (<0.5 mm) ceramic piezo-electric actuator, and scanned in a spiral pattern at the natural

mechanical resonance of the piezo tube [41]. This gave a frame rate of 7 Hz, which is the natural resonance frequency of the piezo tube which cannot be modified, restricting the scanning rate [42]. The geometry of the entire system was still rather large, with a probe tip >10x10 mm.

A scanning mechanism that is not only limited to its resonance frequency is a MEMS reflecting system. Fu et al. used a single axis MEMS mirror (shown in Figure 31) in order to demonstrate their PCF nonlinear endoscope [40]. Although there was still the need to translate the sample stage on one axis, this still improved the image acquisition time, paving the way for two-dimensional scanning systems.

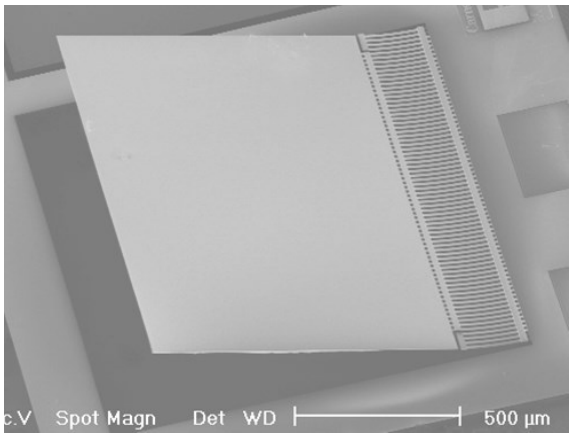

Figure 31: The single axis MEMS mirror used by Fu et al. in their nonlinear endoscope [40]

Various two-dimensional MEMS reflectors have been used in miniaturized microscopes. The first high frequency scanning assembly used for multi-photon microscopy was demonstrated by Liu et al. in 2008. The system employed was a MEMS mirror from the Fraunhofer Institut Photonische Mikrosysteme, capable of being driven at 2.475 kHz and 19.608 kHz for each axis independent of each other. The resultant frame rate was 24 Hz, which is at the bottom end of frame rate in order to be considered video rate [43]. Video rate imaging is highly sought after for many reasons. These include instant visual feedback for the observer, a reduction in blurring of dynamic cellular processes and a reduction of entire frame blurring (due to breathing, or the heartbeat of the specimen) when performing in vivo imaging. Similar mirrors have been used in other miniaturized endoscope-like probes

including the 2009 GRIN system demonstrated by Tang et al. with their MEMS scanner shown in Figure 32, solidifying MEMS scanners as robust, highly capable, versatile beam directing devices [42], suitable for inclusion into our exoscope.

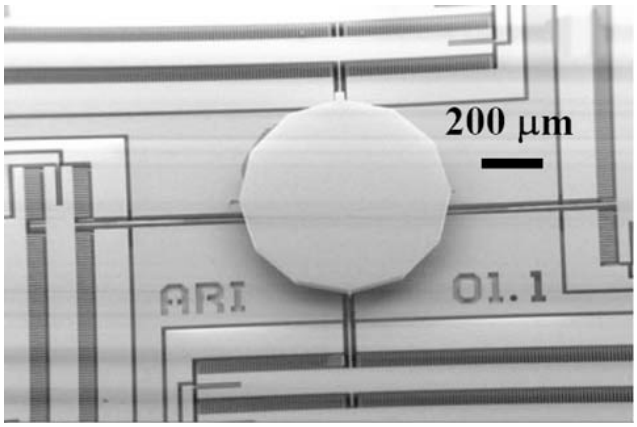

Figure 32: A two-dimensional MEMS scanner used by Tang et al. [42]

3.3.4.2 In-depth Analysis of the Implemented MEMS Scanning Systems

In order to create a minimally invasive, portable scanning CARS exoscope, a laser scanning system that is extremely small, robust, produces large scan angles and high frame rates is crucial. High frame rates are important to this project, as the end goal is to image live animals. Simple things like the beating heart of a rat, or micro movements caused by the animal's breathing can cause significant blurring if high speed acquisition isn't possible. A MEMS based scanner was selected to perform this duty as it fulfills all of those requirements. The fabrication of MEMS borrows the manufacturing process almost entirely from the semiconductor industry, utilizing single crystal silicon and similar etching techniques. This enables the fabrication of extremely intricate moving parts, while maintaining an incredibly high degree of accuracy. The same manufacturing techniques are used to deposit metals to facilitate electrical connections, as well as on the 500 μm diameter reflecting surface, giving a >80% reflection for the pump and stokes wavelengths. Single crystal silicon has proven to be incredibly durable. It has excellent elastic and fracture mechanical properties as there are no grain boundaries, making it a perfect material of construction for high stress elements, such as the torsional springs of a MEMS mirror [44].

The torsional springs are only half of the driving mechanism in the harmonic oscillations of the MEMS mirror. An initial force must be present to displace the reflecting surface from its rest state, before the torsional spring can act on the system. This is an electrostatic force. Figure 33 (a) shows a microscope image of a mirror chip, while Figure 33 (b) shows the engineering diagram [45], with a close up of the electrostatic combs in Figure 33 (c).

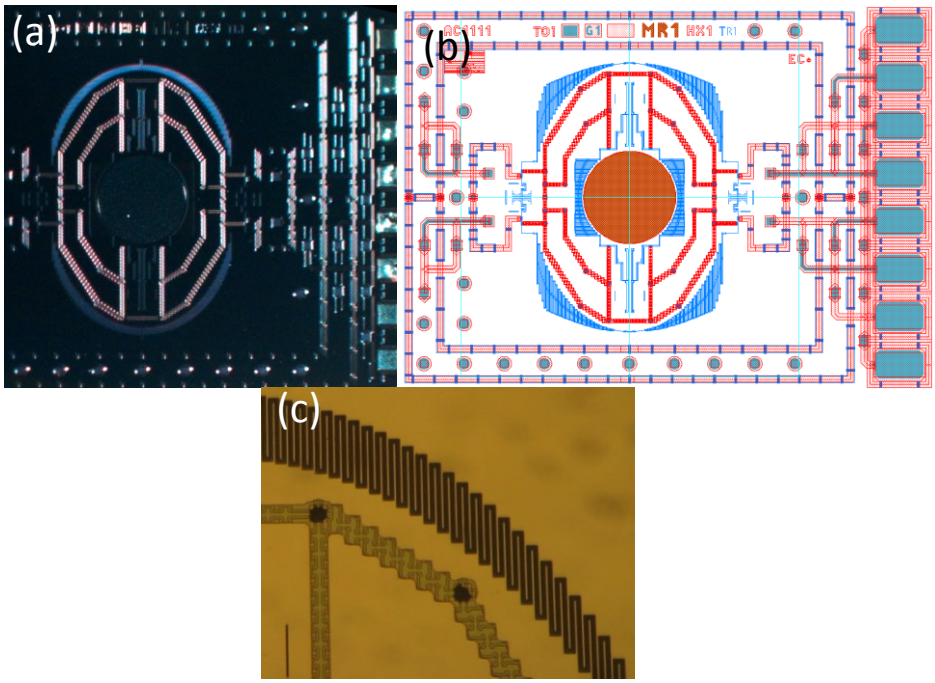

Figure 33: Images of the MEMS used in the exoscope (a) Microscope image (b) Engineering diagram [45] (c) Close-up of the driving combs

In order to generate the electrostatic force, there are combs on both the stationary mirror frame, as well as the oscillatory mirror section. The combs extend out into the space between the frame, and the mirror, alternating between frame and mirror, while never touching. High voltage is applied to the stationary frame. The frame's combs conduct this voltage, forming an electric field surrounding the extended conductors. According to Coulombs law, this electric field will produce a force, acting on the mobile combs, subsequently deflecting the mirror. This applied voltage is a DC square wave, and for the fast axis of the mirror (inner set of driving

combs) has an electrical operating frequency of 33 kHz, while the slow axis (outer set of driving combs) has an electrical driving frequency of 2.5 kHz. During the zero voltage half of the duty cycle, the mirror's torsional springs brings the assembly back to the rest position, until another pulse arrives sending the mirror in the opposite direction. The driving waveforms for the slow and fast axes can be seen in Figure 34.

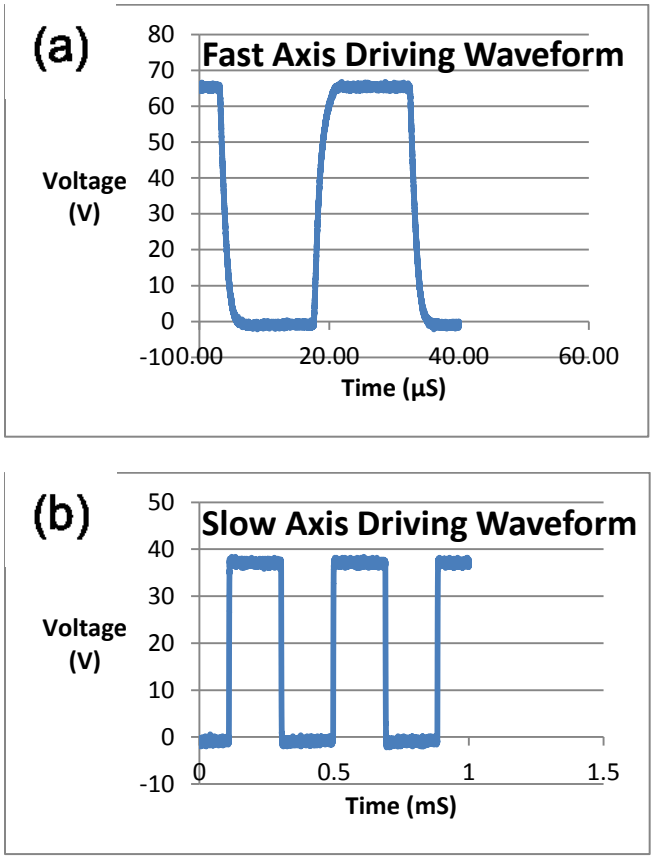

Figure 34 (a) MEMS fast axis electrical driving waveform (b) MEMS slow axis electrical driving waveform

A gimbal suspension allows 2D scanning, both axes operating independent of each other. Both axes of the mirror are driven as close as possible to their natural resonance frequency to maximize the mirror's scan angle and desired field of view. These mirrors will not operate by simply applying the maximum voltage at the eigenfrequency. The amplitude of oscillation must be increased incrementally. Specialized software was developed and run from a field-programmable gate array (FPGA) to sweep from a high frequency (low mechanical oscillation amplitude) to the eigenfrequency. The start frequency is approximately three times the resonance

frequency for both the slow and fast axes, with a sweep time of 10 seconds and a duty cycle of 50%. A typical characterization curve for both slow and fast axes is plotted in Figure 35.

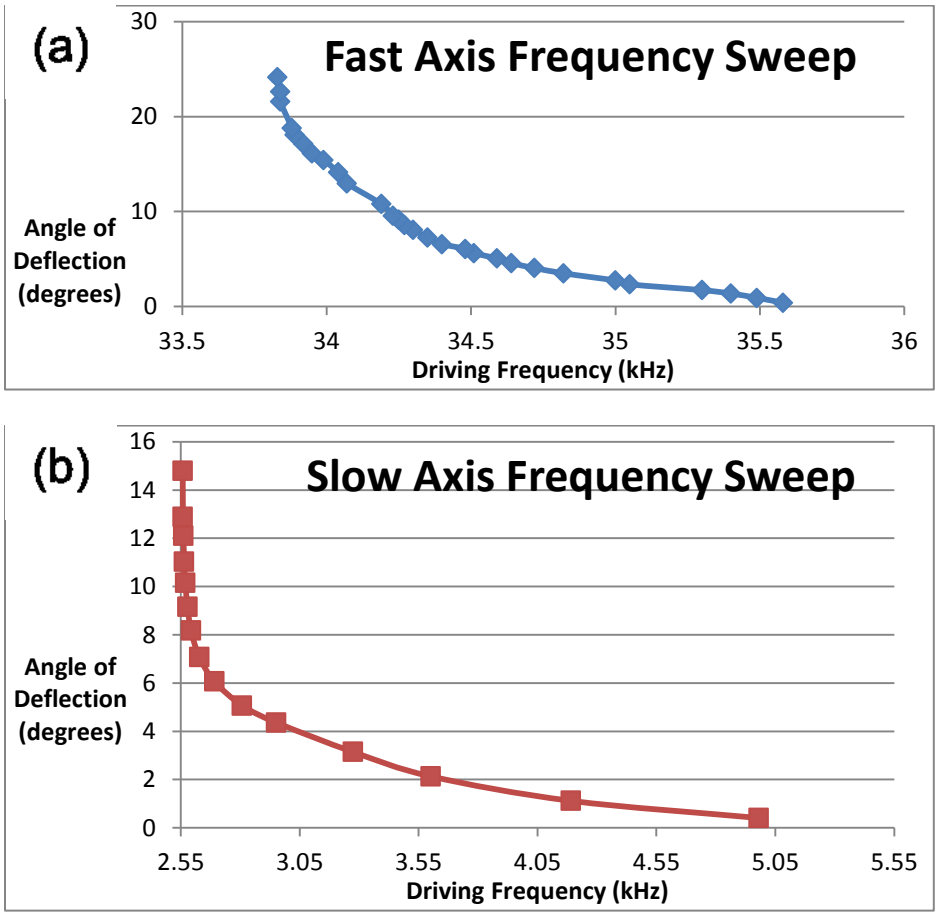

Figure 35: Frequency sweep and corresponding oscillation angle for the (a) fast and (b) slow MEMS axes

A voltage amplification circuit was also constructed to increase the 5.0 V provided by the FPGA to the operating voltage of the mirror. A schematic of the voltage amplifier is shown in Figure 36 with the specific parameters for the slow axis' operational amplifier (op amp). Careful consideration needed to be taken in order to reduce the slew rate of the fast axis to maintain consistent sinusoidal oscillations of the mirror. Op amps from Apex Microtechnology (USA) were used as the slew rate at the required frequency and input voltage was >100 V/µs. A potentiometer was used to tune the output voltage allowing the same op amp to be used for both slow and fast axes.

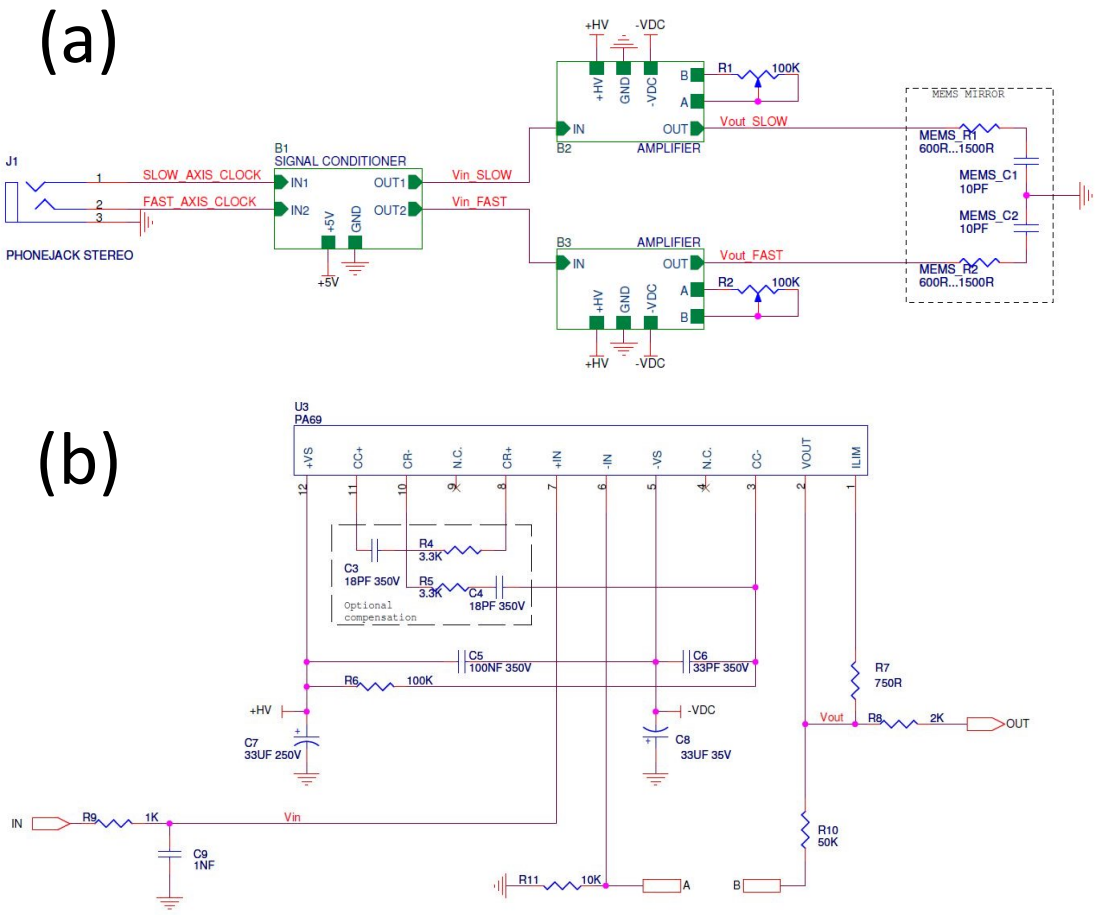

Figure 36: (a) Electrical high voltage amplification circuit (b) Operational amplifier specific configuration

The electrical driving square wave has an amplitude of 37 V for the slow axis and 65 V for the fast axis. This corresponds with a sinusoidal mechanical oscillation frequency of ~2 kHz for the slow axis and ~16 kHz for the fast axis. When combined these parameters result in a mechanical oscillation of +/-8.5 degrees and a corresponding Lissajous scanned ~100x100 µm field of view. A pair of prototype, DIP packaged MEMS mirrors were supplied by the Institut Photonische Mikrosysteme. After initial testing and successful scanning trials, ten mirror chips for exoscope use were ordered.

3.4 Assembly of Selected Miniaturized Components

The assembly and alignment of the miniature optics provided a significant challenge. The optics located within the front end of the exoscope (barrel) had to be precision aligned. The high number of optical elements and size constraints of the barrel, would not allow for any precision adjustments to be made once the optics were cemented into place. Instead, extremely tight tolerances on the machining of the stainless steel were necessary. Once the focusing optics, as well as the end capping window were installed, the barrel was tested independently with a dual in-line packaged (DIP) MEMS mirror. Upon confirmation that the chromatic aberrations weren't detrimental to the ability to generate CARS photons, the assembly of the entire system could begin.

As the assembly process was performed off site in a clean room, the Ti-sapphire laser was not viable for alignment. Instead, a 750 nm diode laser was used. The diode laser was coupled to the LMA20 delivery fibre by a 10X microscope objective (with a transmission of 53%), and then connected to the collimating lens. The collimating lens was located within a separate aluminum mount that would be connected to the body. Once the collimating lens assembly was in place, the folding mirror and the dichroic mirror were also cemented into place and a dummy reflector was placed instead of the MEMS mirror for simplicity of alignment. The optical alignment of the main section of the exoscope could be completed without the additional complications the barrel would introduce. After ensuring the diode laser beam was on axis, the dummy reflector was replaced with the MEMS mirror. As it is critical that the 500 µm reflector of the MEMS mirror reflects the most amount of light as possible, it has full three degrees of freedom. The transmission of the 720 nm laser light through the body of the exoscope remained low, at 46% (it is important to note that this transmission number does not include the barrel and the many optical elements located within), regardless of the adjustments made to the various fine position controlling hardware. It is important to note that due to the

extremely small size of the internal optical pathway of the exoscope, there is no possible way to obtain direct power measurements in between optical components. It was theorized that the removal of a pinhole (located after the collimating lens) would increase the throughput of the exoscope body by >10%. This would potentially see the reflective surface of the MEMS mirror overfilled, a risk that was deemed necessary in order to maximize the power output of the system. The removal of the pinhole saw the output efficiency increase by 12%.

Figure 37: Photograph of the barrel housing the focusing optics

With the internal components of the body fully aligned, the barrel (seen in Figure 37) was added. Three adjustment screws attaching the barrel to the body allowed fine tuning of the transmission and alignment of the laser beam. Potentially due to a slight offset of the collimating lens (this component was cemented into place making the position impossible to alter with respect to the fibre tip) or some problems with the internal alignment of the barrel optics, the output of the barrel tip was slightly off axis. No amount of adjustments with any of the alignment screws could alter the amount of this optical offset. Figure 38 demonstrates the following simulations, and the effect on the optical beam path: Lateral displacement of the input fibre with respect to nominal as well as a 1 degree tilt in the barrel optics.

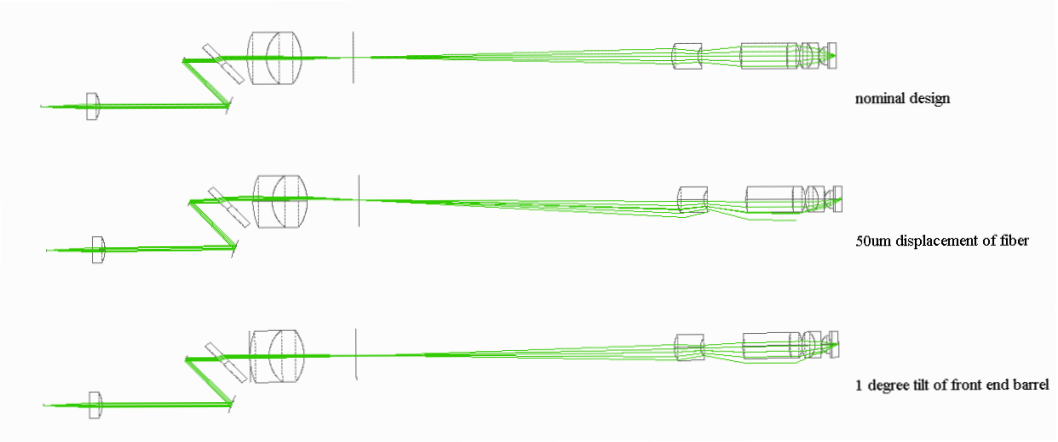

Figure 38: Simulations performed with various misalignments

With all adjustment screws firmly in place, and the cavity sealed, the assembled exoscope (as depicted in Figure 39 (a) and (b)) could leave the clean room, and begin testing.

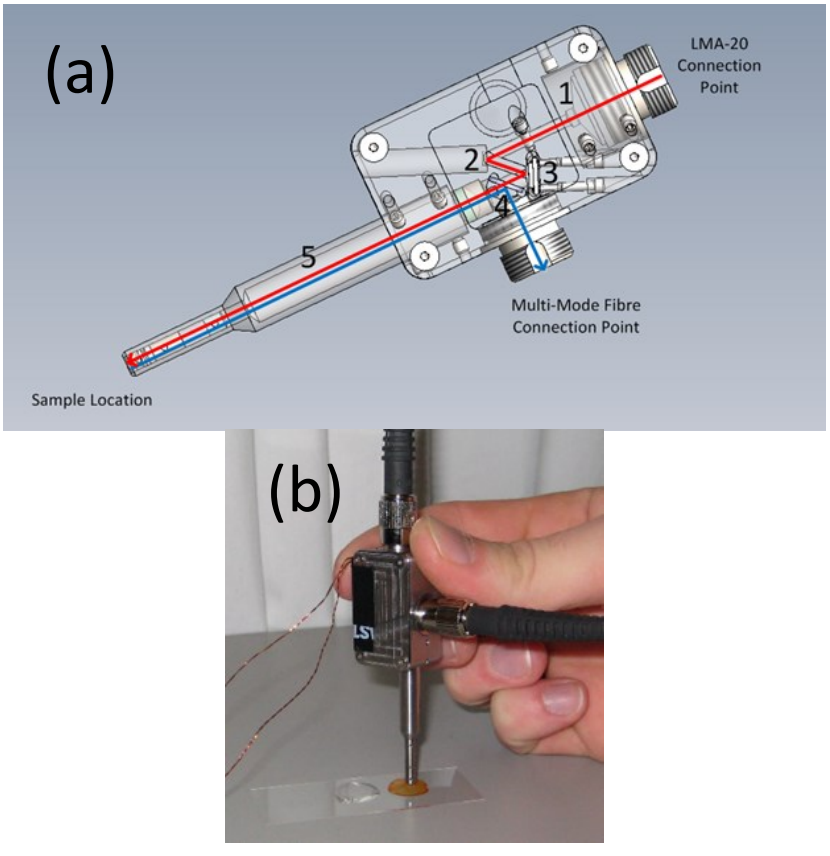

Figure 39: (a) Computer-aided design image with excitation (red) and emission (blue) pathways (1) Collimating lens housing (2) Turning mirror (3) MEMS mirror (4) Dichroic mirror (5) Barrel (b) Photograph of the exoscope

3.5 Photon Collection and Capture

A critical component to the exoscope function is the ability to efficiently capture photons of a desired wavelength for specific imaging modalities. Following the nonlinearly generated photon's journey back through the exoscope, the capture process starts with the collection fibre. The 1.0 mm diameter of the multimode fibre selected acts as a photon bucket, allowing the capture of photons scattered away from the focal point. The multimode fibre also has low losses over a broad wavelength range, from 300-1200 nm, with an NA of 0.39.

As mentioned in 3.2.3, there is a dichroic filter to selectively direct blue shifted photons to the collection fibre, although this does not completely extinguish 100% of the excitation wavelengths. If left as is, the excitation photons would greatly overwhelm any of the blue shifted photons which need to be detected. In order to sort this out, additional filters were added prior to the entrance of the PMT. Specifically, a band pass filter centred at 645 nm (ET645, Chroma Technology, USA) was used for CARS imaging. The spectral transmission curve is shown in Figure 40 (a) [46]. The spectral transmission curve of the filter (680SP) used for all imaging modalities to extinguish the excitation beams is displayed in Figure 40 (b). An additional short pass filter is used for SHG imaging, with cut off at 485nm (Z485SP, Chroma Technology, USA).

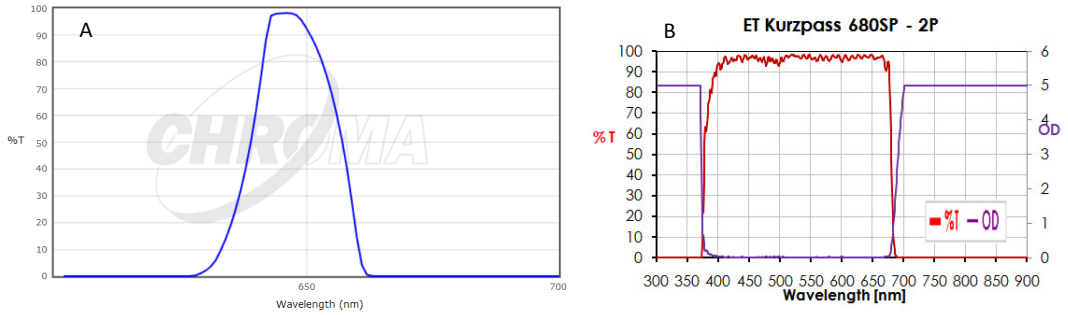

Figure 40: (a) Spectral transmission filter used for CARS imaging [46] (b) Spectral transmission filter used for SHG imaging

Immediately after the modality specific filters was the PMT, to convert photon energy to electric current. Two PMTs were used, the first a H7422 from Hamamatsu (Japan), with the sensitivity plotted in Figure 41 A. It is important to note that the H7422 is blind in the 800 nm region, requiring the laser to be tuned to <750 nm in order to complete the transmission measurements of the USAF target. Part way through the development of the exoscope, a new PMT was acquired due to the quantum efficiency degradation of the H7422. The replacement PMT, a Hamamatsu R3896, was sensitive in the titanium-sapphire's 800 nm native operating wavelength making the USAF TX imaging simpler to obtain, while stressing the necessity of filtering out all of the pump photons before nonlinear signal detection. The sensitivity and quantum efficiency of the R3896 can be seen in Figure 41 B [47].

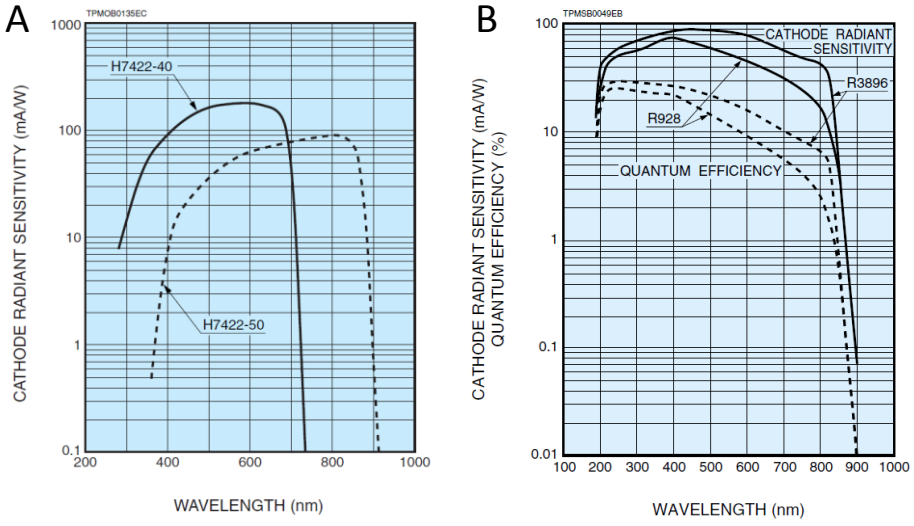

Figure 41: PMT sensitivity (a) Hamamatsu H7422 (b) Hamamatsu R3896 [47]

3.6 Entire System Description and Analysis

All of the individual exoscope components have been discussed in detail, but it is only half of what is required in order to generate a CARS signal. A method to generate two ultrafast laser pulses, overlapping in both time and space is critical to the CARS imaging modality. This section describes the entire system and how these

two wavelengths are created. Figure 42 will be referenced heavily in the following segment.

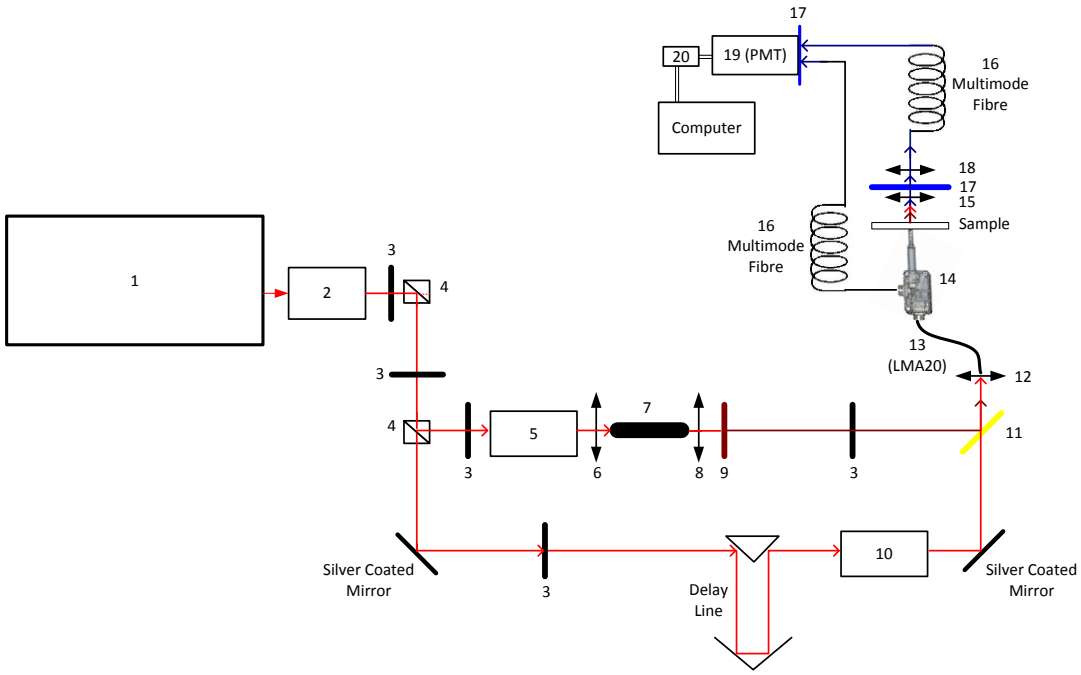

Figure 42: Entire nonlinear imaging system setup

The entire process begins at (1), the titanium sapphire laser. In order to eliminate back reflections into the laser cavity, we have an isolator (2). A half wave plate (3) in conjunction with a polarizing beam splitter (4) allow for alternative experiments to be performed outside of the CARS setup. Another half wave plate (3) and polarizing beam splitter (4) are used to control how much power is sent to either the pump or the Stokes arm.

For the Stokes arm, a half wave plate (3) is used to control the polarization before the beam enters a prism compressor (5), which ensures a transform limited pulse before being focused by an aspheric lens (Thorlabs, USA) having a focal length of 4.5 mm. (6) into the supercontinuum generation PCF (7). A collimation lens (8) directs the supercontinuum towards a notch filter (9), before hitting the final component in the Stokes arm, a half wave plate (3) which controls the polarization before recombination with the pump beam.

As for the pump arm, the path length, and relative polarization to the Stokes arm must be considered. The relative polarization is controlled by another half wave plate (3), while a network of mirrors are used as the delay line. A telescope system of lenses (10) allows the beam diameter of the pump arm to match that of the Stokes arm, before recombination at a dichroic mirror (11).

Both beams are now collinear, overlapping in both space, time and having matching polarizations before being focused by a 10X lens (12) into the LMA20 fibre (13). The beams of light pass through the exoscope (14), and can be collected in either the forward or backward directions. For the forward collection geometry, either an air objective (20x, Mitutoyo, Japan), or a water objective (60X, Olympus, Japan) (15) collimates the beam before being spectrally separated by the filter system at (17). An achromatic lens focuses the nonlinear signal into a multimode collection fibre (16), and that fibre is connected to the PMT (19).

For the epi collection geometry, the backscattered light is collected by a multimode fibre (16) which is connected to a spectral filter (17) that is located on the body of the PMT. For both forward and epi, the output of the PMT is converted to a discrete TTL-like pulse by a discriminator (20) (Ortec, USA) before being handed off to an FPGA and computer system for event counting and image reconstruction. This entire setup is how CARS photons are generated, and it is obvious that the optics involved in the creation of these nonlinear signals is not trivial, but the ability to transmit ultrashort optical pulses to a portable exoscope is clear, due to the ability to deliver, and collect photons via fibre optics.

3.7 Anticipated System Performance

There are two significant resolution measurements that affect the performance of any microscope system, the lateral and axial resolution. The lateral resolution is the ability to resolve adjacent objects in the X-Y plane, while the axial resolution is the

ability to resolve structures in the Z plane (enabling three dimensional imaging capabilities). In order to calculate the lateral resolution, an understanding of how a point source is resolved is imperative. A plane wave of light is not in fact a plane wave at all. According to the Huygens-Fresnel Principle: “every unobstructed point of a wavefront, at a given instant, serves as a source of spherical secondary wavelets. The amplitude of the optical field at any point beyond is the superposition of all these wavelets” [12]. The result of this effect means optical waves cannot be simply treated as plane waves. They must be considered as individual sources, constantly emanating spherical waves. This has a profound impact on the ability to resolve objects that are smaller than the wavelength of light used to illuminate the sample. Instead of being able to illuminate a single spot, an airy disk (seen in Figure 43 [48]) is created around the object. The surrounding artifacts are created by either the constructive or deconstructive interference of the light that diffracts as it passes through the circular aperture of the lens system. In order for a microscopy system to be able to fully distinguish between two adjacent objects, the Rayleigh criterion is used [49]: The images are resolvable if the minimum of one point source is at the maximum of the adjacent point source. Any closer and they are not able to be resolved as distinct objects.

Measurements to determine the Rayleigh criterion are demonstrated in chapter 4, while the calculation to estimate the diameter of the spot size is given as:

$$d = 1.22\frac{\lambda}{NA} \quad (19)$$

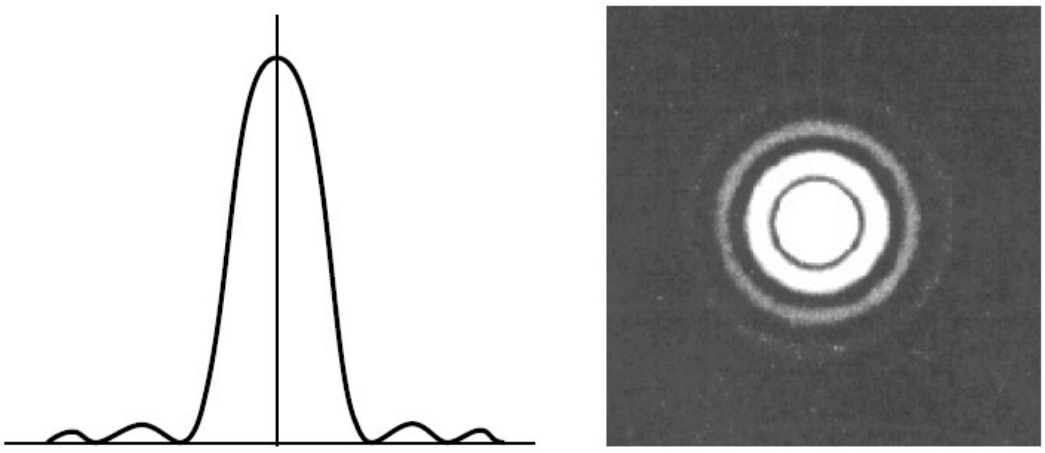

Figure 43: Point spread function and corresponding airy disk [48]

The lateral resolution, while similar to the axial resolution, is the ability to resolve distinct sources in the Z plane. As the purpose of this exoscope is to perform nonlinear imaging, and nonlinear processes are quadratically dependent on the field intensity at the focal plane, the resolution in the Z plane is a function of intensity. In order to calculate the axial resolution, the following equation is used [49]:

$$r_{axial} = \frac{1.4\lambda n}{NA^2}$$

(20)

Where λ is the wavelength in the medium, in this case water $\lambda = \frac{\lambda_{vacuum}}{n}$, λ is the excitation wavelength, n is the index of refraction of the medium and NA is the numerical aperture of the objective lens.

For these calculations, NA=0.6, λ=800 nm, and n=1.33 resulting in an estimated lateral Resolution of 813 nm, and an estimated axial resolution of 3.1 µm The calculated value for the axial resolution coincides quite well with the ~3 µm obtained through simulations performed by the optical designer. The lateral resolution measurements however, differ slightly. This could be due to the simulation including chromatic effects. Experimental investigation of these values will be completed following chapter.

In summary, this chapter has given a synopsis of the progression of CARS from a simple spectral analytical tool, all the way to a powerful chemical specific imaging modality. The technologies that enable CARS probe miniaturization have also been described. Specifics into the particular components that have been used in the exoscope, as well as their operation and characterization have been discussed, ending with an anticipated performance analysis.

With an unlimited budget, the components selected might have been slightly different, possibly resulting in improved system performance. Two multi-watt laser sources would have been ideal for producing the maximum CARS signal possible, but a system at half the cost performs quite adequately, as demonstrated in the following chapter. The selection of the included components (based on the reviewed technologies) maximized the possibility of obtaining a CARS signal from such a single laser-based system. Chapter four demonstrates the culmination of the assembled miniaturized components and the exoscope's ability to offer chemical specific imaging through examination of the results obtained.

Chapter 4

Results and Comparison

4.1 Introduction

All of the experiments undertaken for this thesis will be described in detail in the following chapter. The first main section focuses on an assessment of what is referred to as a benchtop setup. The benchtop microscope's light is delivered via free-space optics, without the LMA-20 delivery fibre. Only a DIP packaged MEMS mirror in conjunction with the barrel, are the only components tested. The second main section describes the tests performed on the completely assembled exoscope including the barrel, integrated MEMS, dichroic mirror, and fibre connectors. The experiments on either setup are similar, starting with the simplest, but still quite significant: determination of the physical size of each pixel. TPEF sensitive microspheres are then examined, followed by CARS sensitive polystyrene microspheres. Lateral axial resolution measurements are performed on these beads, followed by various biological and crystal samples.

4.2 Benchtop Performance Analysis

4.2.1 Pixel Calibration

The complex nature and its extreme sensitivity to optical misalignment means that testing as many individual pieces independently was vital to the success of the project. Once all of the lenses were placed inside the barrel (component housing the lens assembly), it was necessary to confirm that aberrations and resolving power were within operational limits. It is important to note that due to the lack of a dichroic mirror and epi collection fibre on this preliminary test setup, only images in the forward direction were possible. A diagram of the setup is shown in Figure 44.

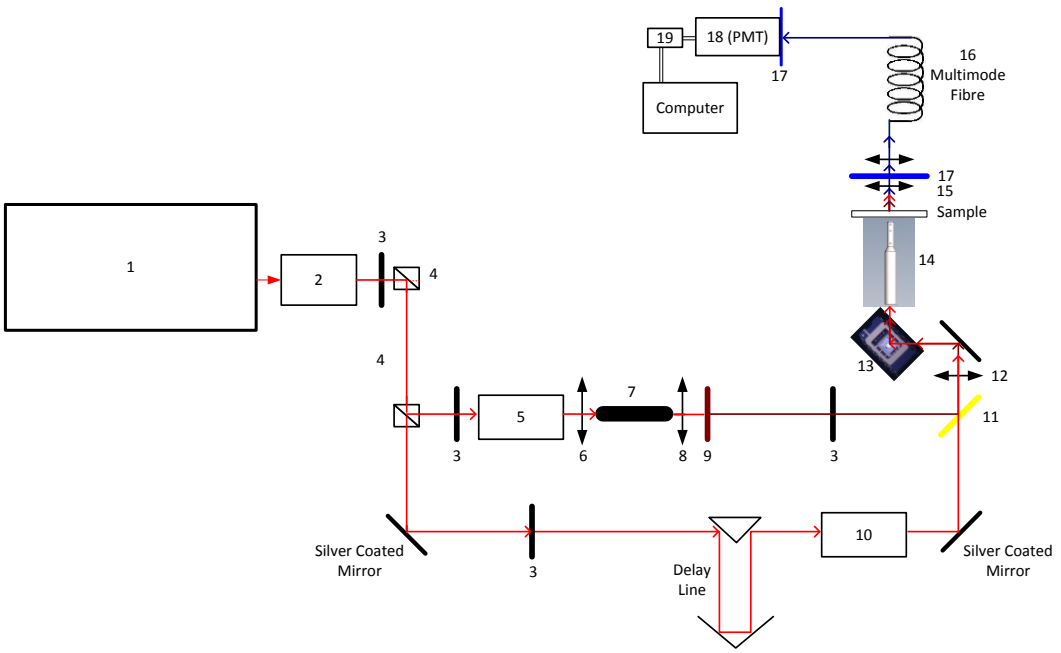

Figure 44: Entire nonlinear imaging system setup with DIP MEMS mirror (13) and barrel only (14)

The first sample that was imaged was a 1951 United States Air Force (USAF) target (Edmund Optics, USA). The purpose of this sample is to calibrate the pixel size of the imaging system. The sample consists of sets of three opaque lines, diminishing in size in a fractal-like pattern towards the centre of the sample, shown in Figure 45 (a) [50]. The first glance at the USAF target through the exoscope barrel can be seen in Figure 45 (b), exposed with white light and being detected by an IR camera (Sony, Japan), demonstrating that there are no obvious issues with the optical alignment.

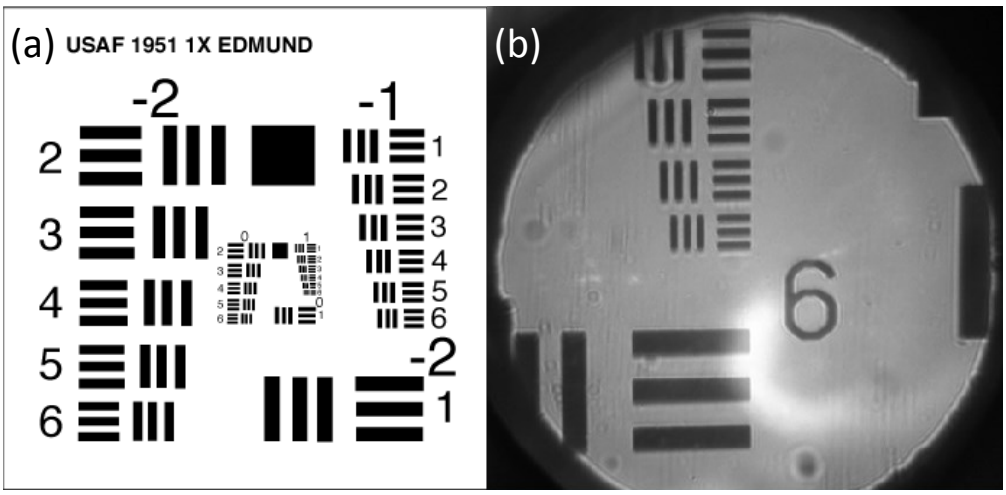

Figure 45: (a) 1951 USAF resolution target diagram [50] (b) White light transmission image through the barrel of the USAF target

Following this rudimentary demonstration, the Ti-sapphire laser was tuned to 720 nm (as the PMT used is blind at 800 nm), and the power reduced to be 1.5 mW average power at the sample. This power was low enough to not cause any damage to the USAF target. A water drop was added to the tip of the exoscope, with the purpose of bridging the gap between the focusing optics and the target. The USAF target was placed upside down onto the water drop. The smallest element (six) on the smallest group (seven) was the area of interest, with a line spacing of 228 line pairs/mm, corresponding to a line thickness of 2.2 µm. Once that area was in the field of view, an optimal focus was achieved by moving the sample vertically in 1.0µm increments. The transmission image of the USAF target, as well as the intensity cross section of the line collection of group seven, element six can be seen in Figure 46. There are no significant image distortions, except for some conical distortion effects where the right side of the image is rotated counter clockwise. This is a known artefact caused by the 45 degree angle between the slow axis of the scanning mirror and the incoming laser light. This has since been corrected for in software processing. The distance between the two dark minima (corresponding to the centre of the dark lines) is equal to 32.175 pixels. When compared to the known width and spacing of the lines, a calibration factor of 0.136 µm per pixel was determined. Following this fundamental calibration, a test to confirm basic

operation and transmission of the crucial wavelengths was made. The first nonlinear imaging that was performed was of fluorescent beads.

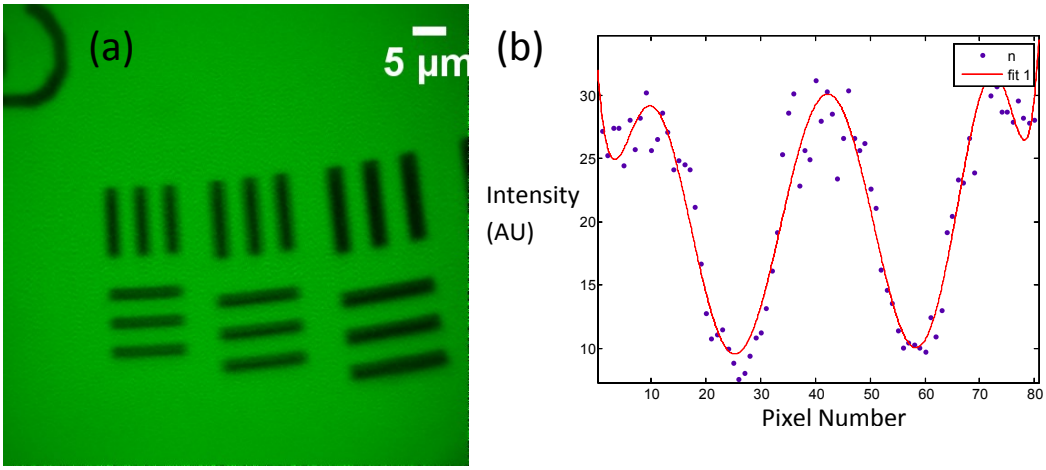

Figure 46: (a) 720 nm transmission image of the smallest resolution bars of a 1951 USAF target (b) Intensity cross section of group 7 element 6 markers

4.2.2 Resolution Measurements

4.2.2.1 Two Photon Excitation Fluorescent Microspheres

1.0µm Fluoresbrite yellow green microspheres (Polysciences, Inc., USA) were chosen, as their excitation and emission spectra (shown in Figure 47 [51]) are suitable for TPEF with the 800 nm Ti-sapphire source. The TPEF beads were diluted, then spin coated onto No. 1 cover slips (Fisher Scientific, USA) in order to reduce natural bead coalescence. The 800 nm laser light was reflected off of the MEMS mirror (80% transmission), and directed toward the back aperture of the barrel (64% transmission). The resultant average power at the sample was 28 mW.

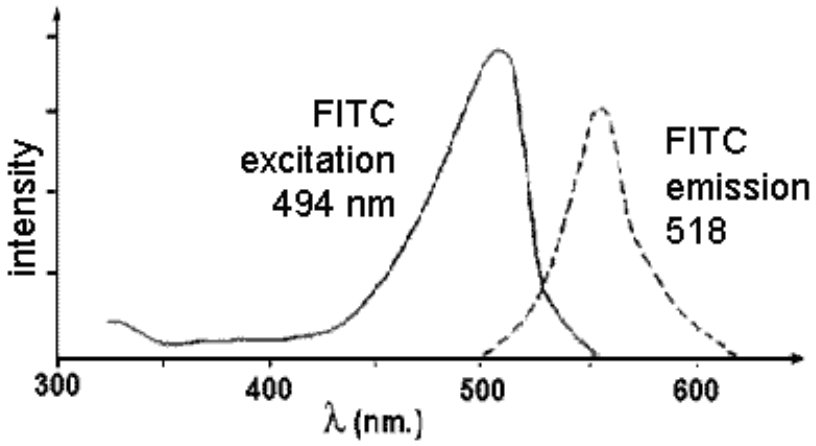

Figure 47: Single photon excitation emission curve for the Fluoresbrite microspheres [51]

The reconstructed image of the beads is shown in Figure 48, and was confirmation that the optics were in sufficient alignment to produce high enough power densities to create a TPEF signal from microspheres near the designed resolution limit. The high power densities actually created a problem in terms of sample burning since the image reconstruction software that was used didn't allow for instant visual feedback, the time for data acquisition was actually quite lengthy. In early TPEF microsphere imaging (and CARS microspheres imaging), many beads were burned before a suitable image or measurement could be taken. Lateral resolution measurements were also taken from these 1.0 µm fluorescent microspheres. A Gaussian curve was fit to an intensity profile plot of a single bead. The full width at half maximum (FWHM) was determined to be ~1.3 µm. Obtaining these nonlinear signals and measurements from a single input wavelength is almost a trivial task when compared to multi-wavelength nonlinear modalities. The generation of CARS photons is a much more difficult endeavour. It was first tested with standard microscope objective oil.

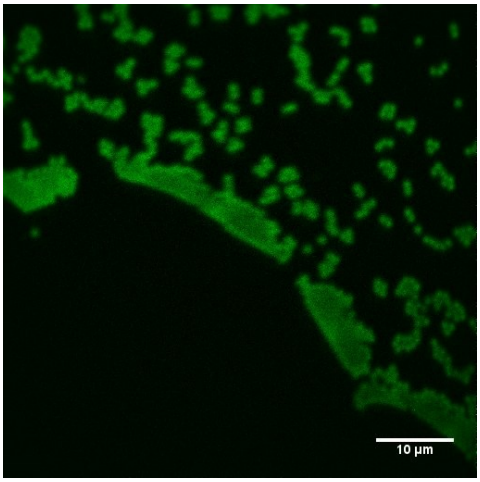

Figure 48: TPEF image of 1um Fluoresbrite microspheres

4.2.2.2 Coherent Anti-Stokes Raman Scattering Generation Microspheres

Microscope objective immersion oil is an excellent sample for CARS imaging. It is designed to exhibit low auto-fluorescence, and its high concentration of C-H bonds generates a strong CARS signal.

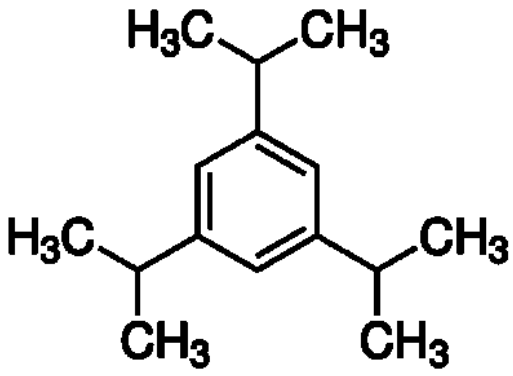

Figure 49: Chemical structure of the microscope oil used for CARS signal verification [52]

A drop of 1,3,5-Triisopropylbenzene microscope objective oil (Olympus, Japan) (chemical structure shown in Figure 49 [52]) was placed onto a No. 1 cover slip. The sample was exposed to 38 mW of the 800 nm pump, as well as 1.0 mW of the 1030 nm Stokes beam. The optical path delay between the two arms was minimized, and with both beams overlapped temporally and spatially, the resultant spectrum in

Figure 50 was observed. This initial confirmation of spatial overlap at the focal volume was not a trivial result to obtain. The many unknowns (including the temporal delay, relative polarization orientation, sample height, power densities, and 650 nm collection) all had to be modified independently, with absolutely no feedback. Once a peak in the background noise of the spectrometer was observed, the relative polarizations of the two pumping beams were aligned with a half-waveplate on the Stokes arm. The presence of the peak at 650 nm confirms that the chromatic aberrations of the barrel weren't significant enough to be detrimental to the generation of CARS photons. After the confirmation that a CARS process is indeed possible with the barrel, it was necessary to demonstrate the CARS imaging capabilities.

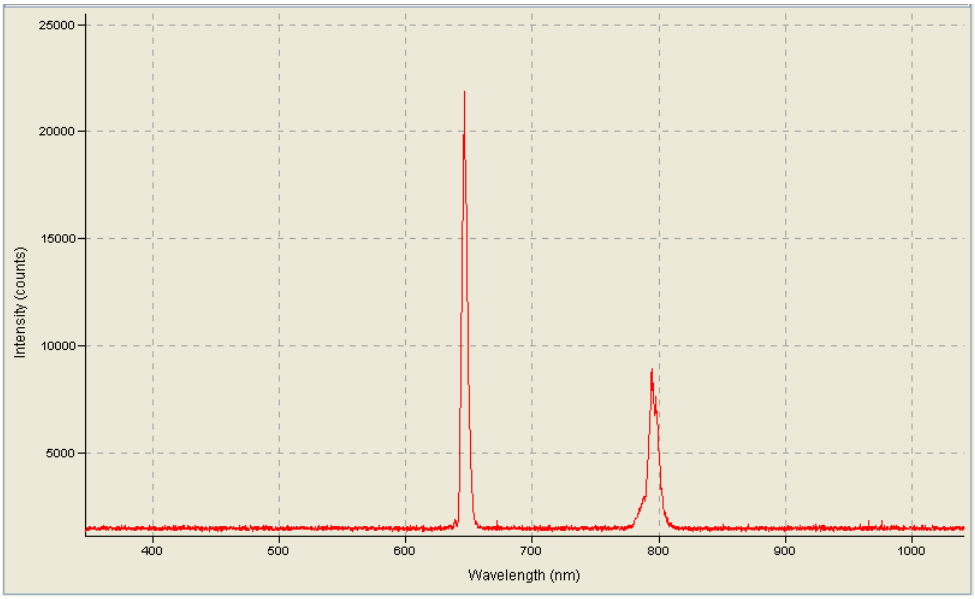

Figure 50: CARS spectrum obtained from microscope objective oil

The first CARS bead sample imaged with the benchtop setup was a 20 µm Polybead microsphere (Polysciences, Inc., USA). Polybead microspheres are a monodisperse polystyrene microsphere. Polystyrene is a suitable candidate for CARS photon generation as there are numerous C-H bonds located throughout the chemical structure shown in Figure 51 (a) [53]. These microspheres were spin coated onto a No. 0 cover slip and exposed to 28 mW of pump light, as well as 800 µW of Stokes

light. The difference between the two pumping wavelengths was tuned so that the aromatic C-H bond vibrations of the polystyrene beads were resonantly excited at 3045 cm^{-1}. The captured image of the microspheres is shown in Figure 51 (b), and based on this result, it is clear that there are no fundamental flaws affecting the spatial overlap of the pump and stokes beam. This also confirms proper operation of the MEMS mirror and image reconstruction. Axial resolution measurements were also performed on CARS microspheres. 4.5 µm Polybead microspheres were prepared in the same way as the 20 µm beads. Once placed on the microscope stage, the beads were exposed to 28 mW of pump light and 800 µW of Stokes light. The entire sample volume was scanned through at 1.0µm intervals. The resultant axial resolution was 12.74 µm.

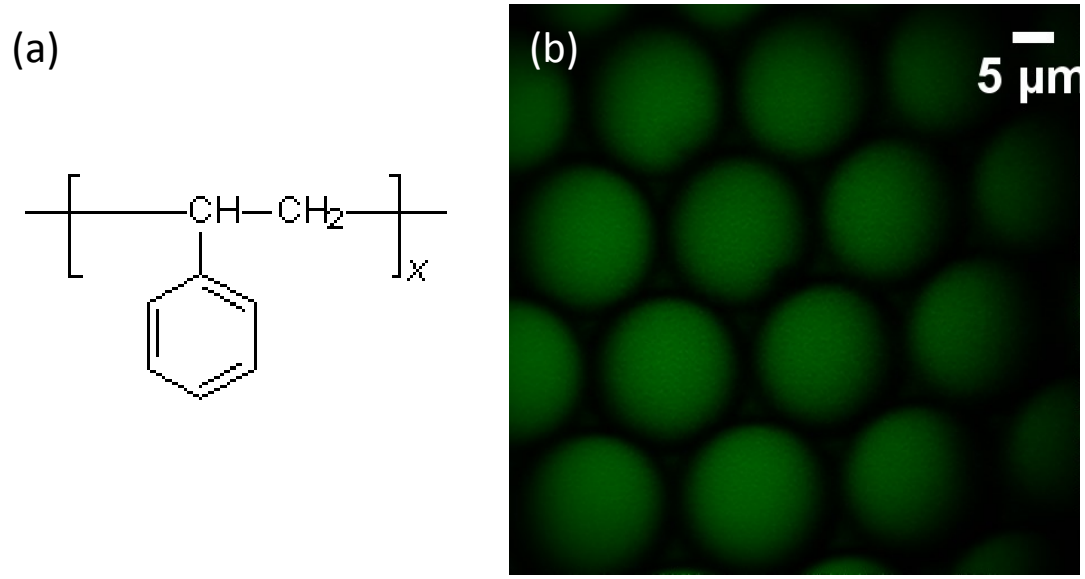

Figure 51: (a) Chemical structure of polystyrene [52] (b) CARS image of 20 µm polystyrene microspheres

4.2.3 Biological Samples

In order to properly exhibit the imaging capabilities of the exoscope, suitable samples must be carefully chosen to appropriately exploit a specific nonlinear mechanism. The samples selected must have appropriate feature sizes for a 70x70 µm field of view, have a high enough structural density (to facilitate the

backscattering of forward propagating CARS photons), and exhibit minimal structural decay while maintain consistent photon generation for an entire imaging period. These parameters must all be satisfied while using appropriate mounting medium that does not generate, or contributes very little to the nonlinear background. For this reason paraformaldehyde could not be used as a standard fixing agent and alternatives were investigated. Discovering biological samples that would demonstrate the fine imaging capabilities of the exoscope was one of the most difficult aspects of this project. For reasons that will be discussed in the following chapter, the larger than designed axial resolution would blur thick structures in the biological samples.

4.2.3.1 Coherent Anti-Stokes Raman Scattering: Myelin

Now that all fundamental attributes of the exoscope have been confirmed, the ex vivo imaging capability could be demonstrated, starting with a 0.5 mm thin section of a fixed dorsal root from a yellow fluorescent protein mouse (Jackson Laboratory, USA). This sample was mounted onto a microscope slide, with a No. 1 coverslip mounted on top of the dorsal root. The sample was imaged with the coverslip on the bottom, again with a water drop to bridge the gap between the barrel and the coverslip. As this is a yellow fluorescent protein (YFP) mouse, the axons exhibit fluorescence at a peak of 530 nm. The lipid rich myelin surrounding the axons remains unstained, and can be isolated by capturing CARS photons. The bright lipids associated with myelin can be clearly seen in Figure 52. A 645 nm notch filter was used to only capture CARS photons. When the Stokes beam was blocked, the signal disappeared entirely, confirming that the photons being captured are indeed CARS photons; the photons generated by YFP were being completely extinguished by the notch filter.

Acquiring this image (as well as all following biological images) was a difficult task. The combination of the lack of uniformity of the sample thickness, inability to observe the sample optically to determine areas of interest, unknown sample quality, and slow speed of image acquisition made all biological images utilized in

this chapter difficult to obtain. Quite often, a CARS (or TPEF or SHG) signal was visible, without any desired structure shown. The field of view was painstakingly translated until either one of two conclusions were made. Either a large enough sample was scanned determining the sample, or preparation method was bad or until the desired structure came to view. The need for water immersion also provided an additional hurdle to these long-term imaging trials. While modifying one of the many parameters mentioned above, the water drop connecting the exoscope with the sample slide would slowly evaporate causing an index mismatch. This would shift the focal point, reducing the acquired signal, often making the correlation between the parameter being modified and the result unclear. As this was setup as an inverted microscope, replacing the water drop also was a difficult manoeuvre to execute without making contact with the microscope slide and moving the sample.

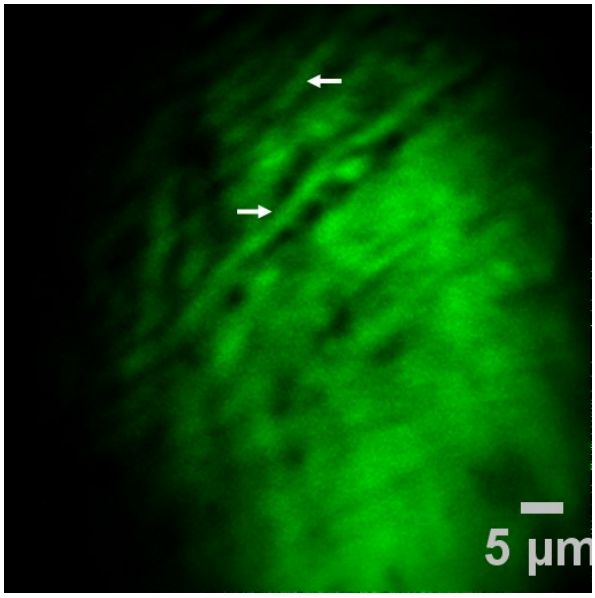

Figure 52: Forward CARS image from label free myelin in fixed dorsal roots of a mouse. Arrows denote label free myelin strands

4.2.3.2 Two Photon Excitation Fluorescence: Axons

The YFP stained axons were imaged following the myelin. The peak of two photon excitation of YFP is known to be ~970 nm [54], where the nominal operation of the titanium-sapphire laser rests around 800 nm. The laser was tuned as red as possible,

attaining mode-lock at a maximum of 870 nm. Fortunately, this wavelength was long enough to excite the YFP, although the signal to noise ratio isn't as high as with the CARS experiments, the axon strands in Figure 53 can still be identified. Finally, the laser was tuned back to its native 800 nm for SHG imaging of unlabeled rat tail collagen. Collagen has a native second harmonic signal as it is highly non-centrosymmetric, and possesses a tremendous nonlinear susceptibility.

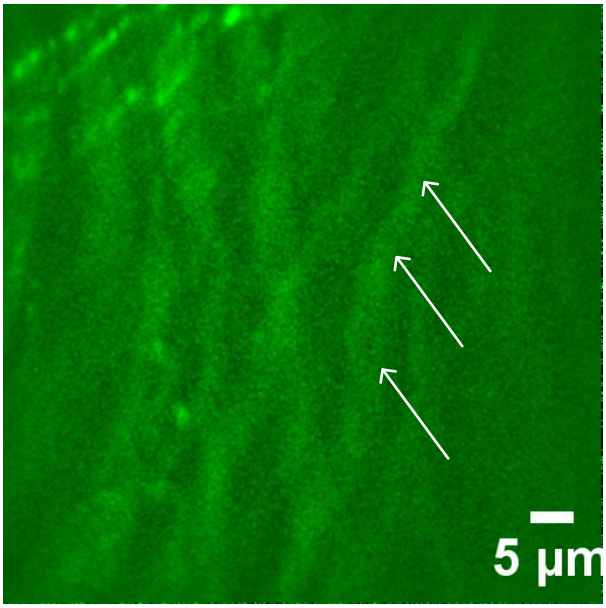

Figure 53: TPEF image of YFP labeled axons excited at 870 nm, with a single axon denoted by the arrows

4.2.3.3 Second Harmonic Generation: Collagen

A 0.5 mm thick sample of tail collagen was prepared similarly to the dorsal root. The wavy type-I collagen is clearly visible in Figure 54. The completion of the biological imaging was confirmation there were no obvious issues that would render CARS imaging impossible. The final assembly of the components could be performed.

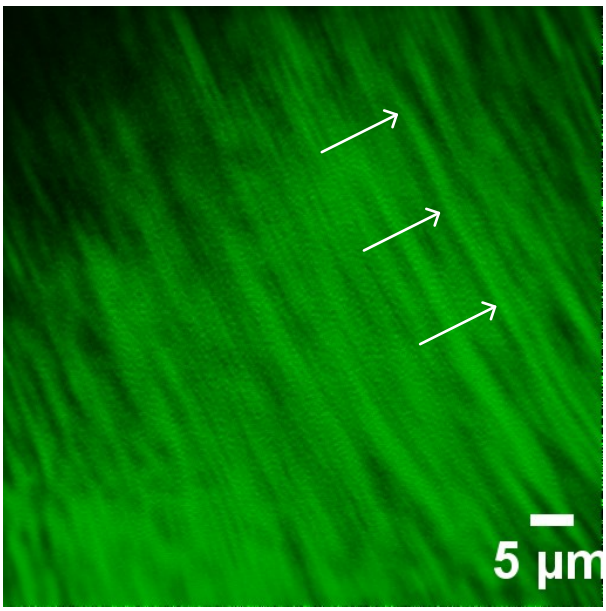

Figure 54: SHG image of unlabeled rat tail collagen, with an individual strand indicated by the arrows

4.3 Fully Assembled Setup

A primary significant difference between the previously demonstrated benchtop setup and the fully assembled setup is the fibre delivery. Before any imaging could be performed, a transform limited pulse had to be delivered to the sample. This was a non-trivial aspect of the exoscope, as with the first fibre that was investigated (DCPCF) ended up with a dispersive profile that was incredibly difficult to compensate for (a further discussion on this topic is made in the following chapter). Also, as it turned out, the pointing of the Ti-sapphire laser output was not consistent over tens of minutes. As the distance between the laser and the fibre was large, any slight change in the pointing of the laser would result in a loss of coupling efficiency out of the LMA-20. Close attention needed to be paid to the quality of mode-locking, as well as the pulse to pulse stability. Floating the optical table seemed to reduce the instabilities, making possible the following measurements.

4.3.1 Pixel Calibration

As with the benchtop setup, the fully assembled exoscope was tested with the USAF target to determine the resolving power of the exoscope in the forward direction. The negative pre-chirped 800 nm pump beam from the Ti-sapphire laser was coupled to the LMA-20 fibre, then to the exoscope. A water drop was placed on the tip of the exoscope, and the glass USAF target was placed marking side down making contact with the water. The sample height and x-y positions were modified until the smallest features of the resolution target were in focus. The average power at the sample was 16 mW, which was attenuated after the target by a 680 nm short-pass filter (Chroma Technology, USA). There was no need to tune the laser to 720 nm as with the benchtop setup, as a different PMT was used (Hamamatsu R3896). This PMT has a quantum efficiency that is greater than 40% at 800 nm. The smallest features (group 7, element 6) are resolved in Figure 55 (a). As this is the same target, and the same group and element used in the benchtop pixel calibration, all line dimensions are the same. An intensity cross section is plotted in Figure 55 (b), and when compared to the actual line thickness, a calibration factor of 0.118 µm per pixel was obtained.

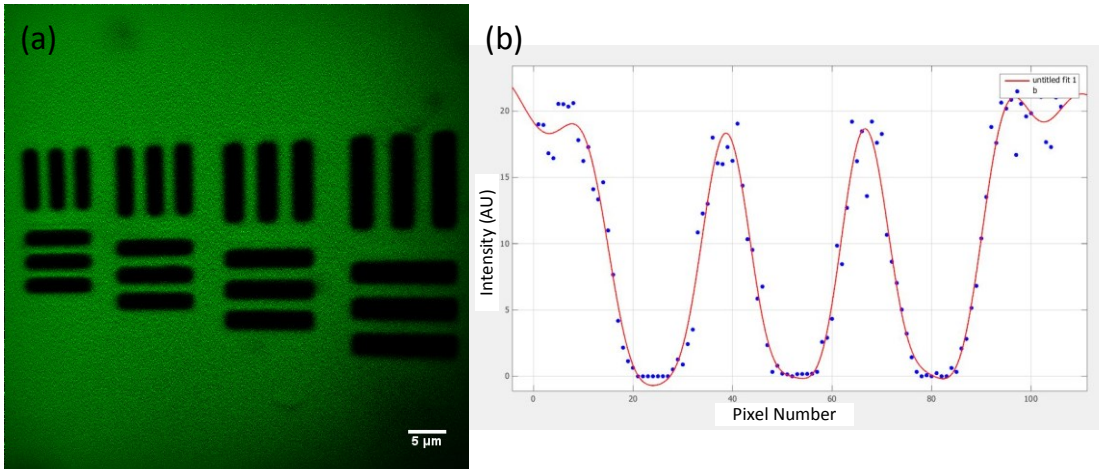

Figure 55: (a) 800 nm transmission image of the smallest resolution bars of a 1951 USAF target (b) Intensity cross section of group 7 element 6 markers

4.3.2 Resolution Measurements

4.3.2.1 Two Photon Excitation Fluorescent Microspheres: Axial Resolution

Following the USAF calibration, the performance of the exoscope was further examined by determining the axial and lateral resolutions. TPEF sensitive 1.0 µm diameter fluorescent microspheres (Polysciences Inc., USA) were spin coated onto a #1 cover slip. 800 nm light from the femtosecond laser was negatively chirped to compensate for the dispersion introduced by the LMA-20 delivery fibre. After being coupled to the LMA-20, light was sent to the exoscope, with an average power of 15 mW at the sample. The transmission efficiency through the exoscope was 47%. The spin coating of the beads reduced the natural occurrence of bead coalescence as seen in Figure 56 (a). For beads that were in focus across the FOV, the intensity profile was plotted. A Gaussian curve was fit to this profile (shown in Figure 56 (b)) and the bead size was found to be 0.94 µm. It is important to note that in contrast with the acquired benchtop images, the fully assembled exoscope allows for photon collection in the epi direction. The generated photons were either generated in the backwards direction or forward propagating photons that were backscattered. These photons then entered back through the exoscope tip and subsequent lenses, reflected off of the dichroic mirror and directed to the multimode collection fibre.

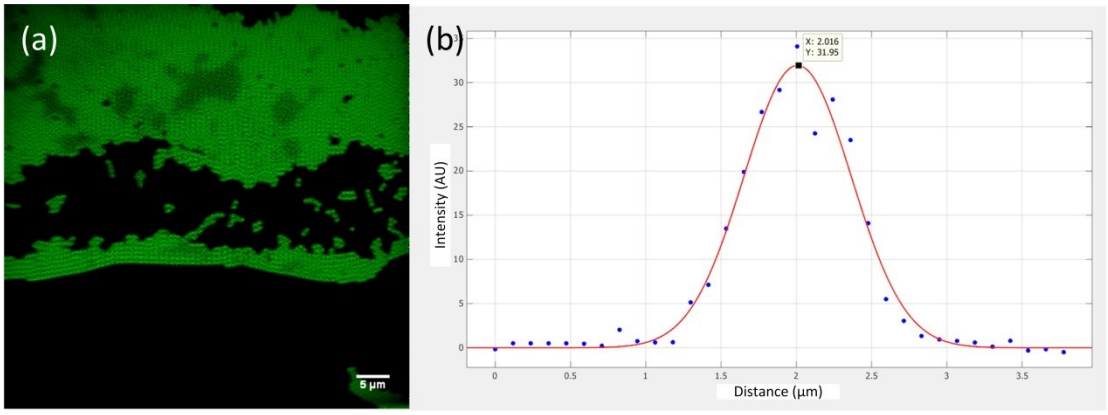

Figure 56: (a) TPEF excitation of 1.0 µm Fluoresbrite microspheres in the epi direction (b) Lateral intensity profile of a single 1.0 µm Fluoresbrite microsphere

4.3.2.2 Two Photon Excitation Fluorescent Microspheres: Chromatic Aberrations

The second set of fluorescent microsphere measurements were performed with a sample of 4 µm rainbow microspheres (Bangs Laboratories, Inc., USA), coated with eight different fluorescent dyes including FITC, PE, PE-Texas Red, PE-Cy5, PE-Cy7, APC, APC-Cy7, and Violet 1. The reason for the plethora of dyes is due to the fact that these beads were used in determining the chromatic aberrations of the exoscope, necessitating fluorescence over a wide excitation spectrum. A plot of the excitation bands of these fluorophores is shown in Figure 57. It is evident that these beads will provide single photon fluorescence from 375-775 nm and consequently a TPEF mechanism could be exploited for the wavelengths of interest from 800 to 1000 nm.

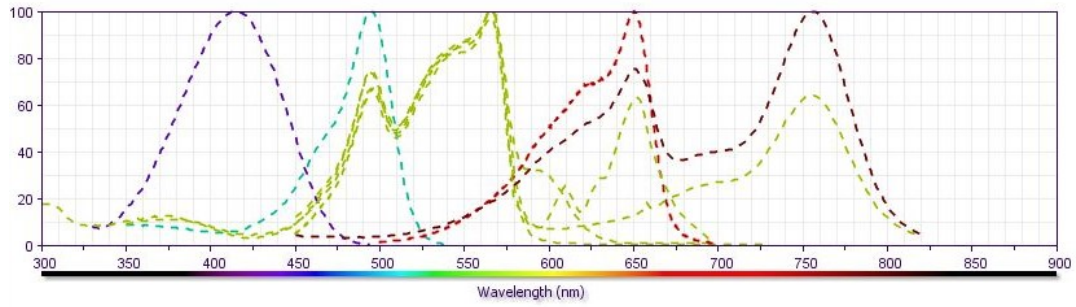

Figure 57: Complete spectral plot of all fluorophores fixed to the 4 µm rainbow microspheres

Unfortunately, the amount of peak power available at the sample of the Stokes beam alone was not enough to produce a detectable TPEF signal. The pulse broadening that occurs in the delivery fibre in conjunction with the low power availability out of the supercontinuum is to blame for the low peak power availability. Fortunately, the inherent tuneablility of the Ti-sapphire laser facilitated imaging the rainbow microspheres with a longer wavelength. It was possible to tune the Ti-sapphire to 960 nm before mode locking was no longer maintainable for these aberration measurements.

As was previously prepared, the beads were diluted, and mounted on a #1 coverslip. Three separate experiments were performed to determine the severity of the

chromatic aberrations, starting with the change in axial resolution. The sample was exposed to 0.8 mW of 800 nm light. The rainbow microsphere sample was placed on the sample stage, with a water drop bridging the gap between the exoscope's optics and the coverslip. The bead sample was stepped through the focus of the exoscope at 5 µm intervals until only background noise was visible, collecting photons in the epi direction. The three dimensional stack of these images is shown in Figure 58. A lateral profile of a single bead on each image was taken, with the maximum intensity of each plotted against the Z position. A Gaussian curve was fit, in order to determine the FWHM as well as the peak intensity location. The same procedure was implemented, with the same field of view while exposing the sample to the 960 nm beam. It was determined that the peak location of the 800 nm axial resolution was at 100.9 µm, while the peak of the 960 nm axial resolution was at 102.9 µm, a difference of 2 µm.

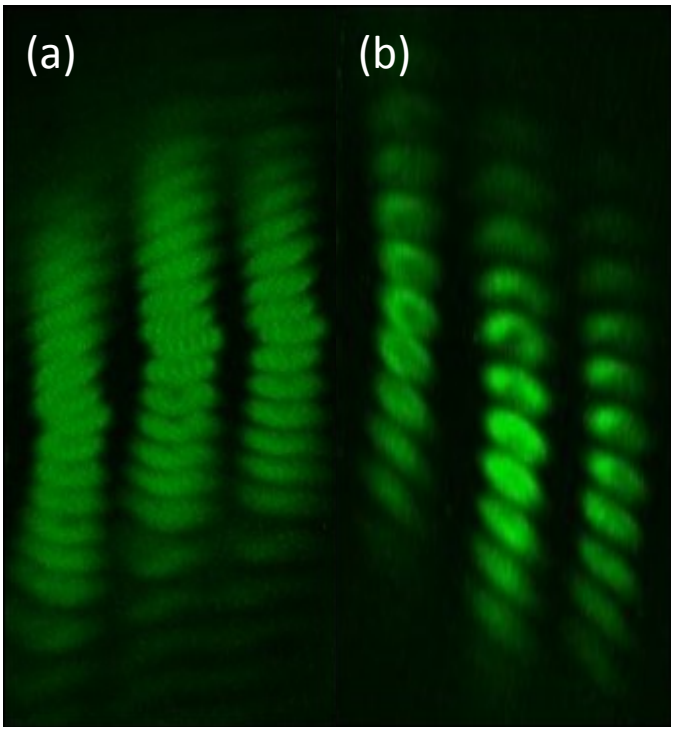

Figure 58: Axial resolution image stack (a) 800 nm excitation wavelength (b) 960 excitation wavelength

The second chromatic aberration measurement was the lateral displacement. The most in focus frame from the previously analyzed Z stack was taken, and a lateral intensity profile was obtained in both the X and Y directions. A Gaussian curve was fit to both the 800 nm and 960 nm plots, and it was determined that the peak shifted by a total of 0.1 µm in the X direction, and 0.29 µm in the Y direction. The beads that these experiments were performed on are displayed in Figure 59 (a) and (b). The corresponding horizontal and vertical intensity profile plots of both the 800 nm and 960 nm measurements relative to the edge of the frame are shown in Figure 60.

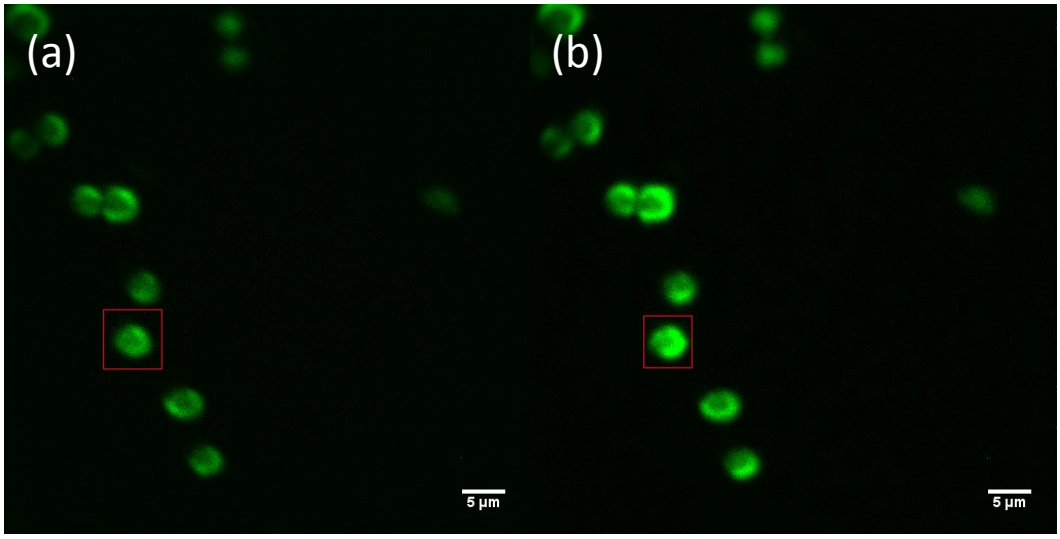

Figure 59: Lateral chromatic aberration images (a) 800 nm excitation wavelength (b) 960 nm excitation wavelength

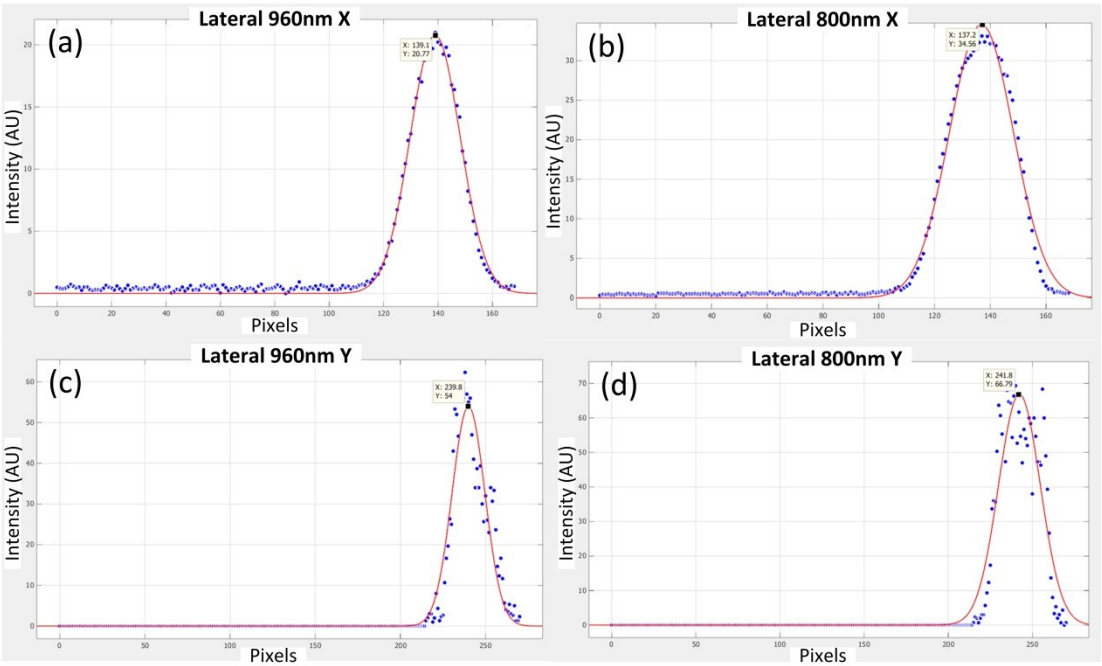

Figure 60: Lateral chromatic aberration intensity plots (a) 960 nm horizontal (b) 800 nm horizontal (c) 960 nm vertical (d) 800 nm vertical.

4.3.2.3 Coherent Anti-Stokes Raman Scattering Microspheres

Similar to the benchtop experiments, the CARS imaging started with 20 µm, 4.5 µm and 2.0 µm polystyrene beads. These beads were spin coated onto #1 coverslips. The aromatic C-H bonds in all of these beads have a strong peak at 3070 cm^{-1} when resonantly excited. Again, it is crucial to note that the images shown in Figure 61 have been collected in the epi direction.

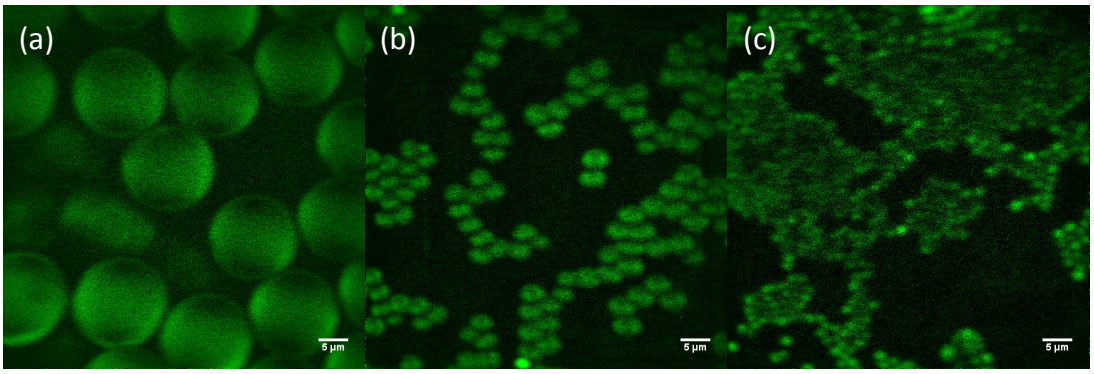

Figure 61: Epi CARS microsphere images (a) 20 µm (b) 4.5 µm (c) 2.0 µm

CARS axial resolution measurements were performed on a series of 2 microsphere samples. Photons for this resolution measurement were also collected in the epi

direction in a similar fashion to the TPEF chromatic axial resolution measurements, although with a 1.0µm step size due to the decreased bead size. For the entire data set, a line profile of a single bead was taken at each Z step. The maximum intensity was identified, plotted and fit with a Gaussian curve, shown in Figure 62. The resultant axial resolution was determined to be 15.8 µm. This concludes the resolution measurements and characterization of the exoscope, onto the demonstrations of the biological imaging capabilities of the system.

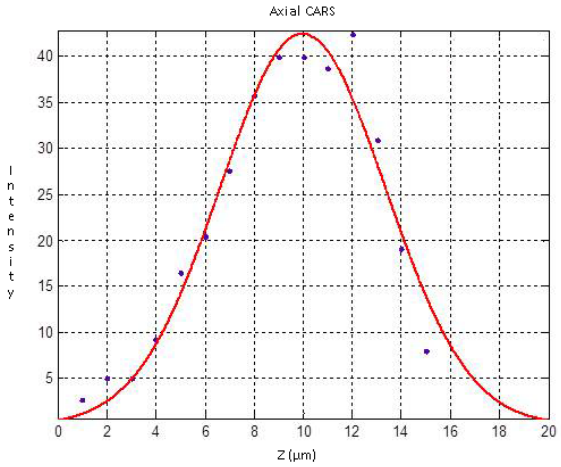

Figure 62: Axial epi CARS resolution plot

4.3.3.1 Two Photon Excitation Fluorescence

To begin the exoscope's ex vivo biological imaging, a stained tissue sample was selected. The tissue was from a mouse lung, perfused with fluorescein (Life Technologies, USA) in Fluoromount mounting medium (Sigma-Aldrich, USA). In order to attain the required concentration of fluorescein in the vasculature, the mouse was anesthetized, followed by a fluorescein injection. With all blood replaced by the fluorescein solution, any portion of the mouse could be used as a suitable TPEF candidate. Mouse brain tissue was the first sample used, although the fine structure of the brain vasculature underwent rapid degradation and was not suitable for use. The lung tissue, however, turned out to be very robust and held up well to imaging. Thin samples that would reduce this blurring, and consequently increase the interface-generated epi CARS were the obvious choice for improving the quality of the images recorded.

The section of lung tissue was placed between a microscope slide, and a #1 coverslip. The package was placed coverslip side down, with a water drop bridging the gap between the exoscope tip and the coverslip. The sample was exposed to 18 mW of the 800 nm pump beam. The generated TPEF signal was collected in the epi direction, with the excitation wavelengths filtered out by a short pass filter (Chroma Technology, USA). The fluorescein that had propagated throughout the mouse's vasculature can clearly be seen in Figure 63 (a). The vasculature rich alveolar walls are clearly visible, surrounding the void of the alveolar cavities. A confocal image of the same sample is also shown in Figure 63 (b) for comparison, demonstrating the same fluorescing alveolar wall vasculature.

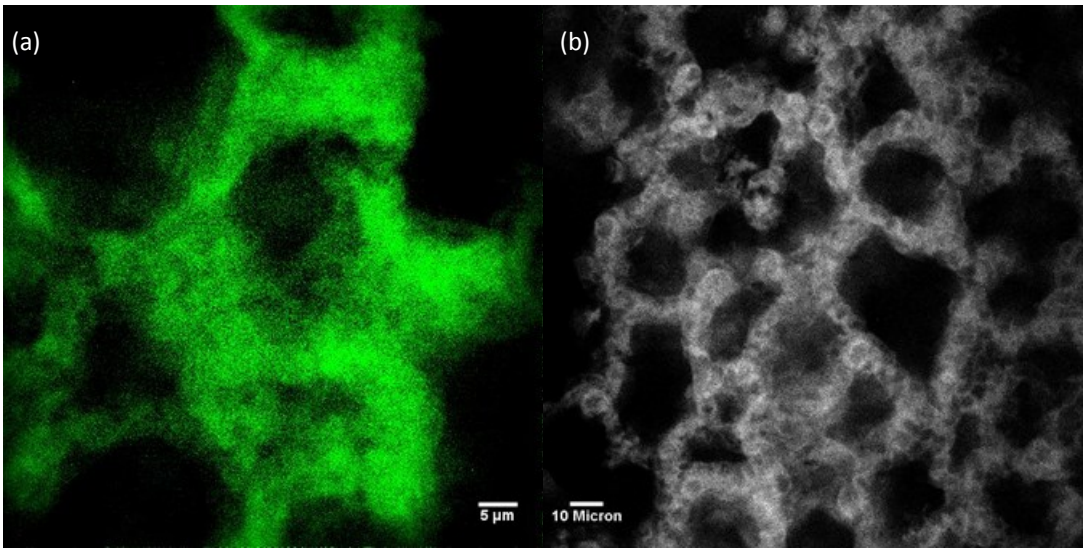

Figure 63: Fluorescein perfused mouse lung tissue (a) Epi TPEF excited at 800 nm (b) Confocal microscope image for reference

4.3.3.2 Second Harmonic Generation

When compared to TPEF, the generation of SHG photons is similar as they involve two pump photons to create the blue shifted nonlinear signal. This is where the similarities end, as the SHG process is parametric, while the TPEF process is not. This subtle difference results in the emission of photons that are exactly equal to double the energy of the incoming pump photons. No energy has been absorbed by the tissue structure. Imaging must be performed to confirm the exoscope's ability to capture these higher energy photons in the epi direction. The sample that was

chosen was potassium dihidrogen phosphate (KDP). KDP crystals are popularly used as frequency doubling elements for lasers, used in electro-optic modulators, Q-switches and many other nonlinear optic applications. For exoscope testing, various sample preparations were tested. The method that generated a strong nonlinear signal and periodic structure was attained through pulverization of the crystal followed by dissolution into water. The aqueous solution was placed onto a #1 coverslip, allowing the water to evaporate. The sample was placed on the microscope stand, with a drop of water between the coverslip and the exoscope tip. 3.5 mW of the 800 nm pump light was scanned across the sample surface. The generated SHG was captured in the epi direction, with an additional short pass filter (Chroma Technology, USA) to block out any unwanted nonlinear signal. The longitudinal structure of the KDP crystal is displayed in Figure 64 (a). Confirmation of the crystal's sample structure is demonstrated in Figure 64 (b). This image was taken with a white light transmission microscope with a 40X objective. The ability of the exoscope to capture SHG photons in the epi direction is clearly visible based on this image alone, although since the goal of this project is to perform in vivo imaging of biological tissues, a biological collagen sample was also imaged.

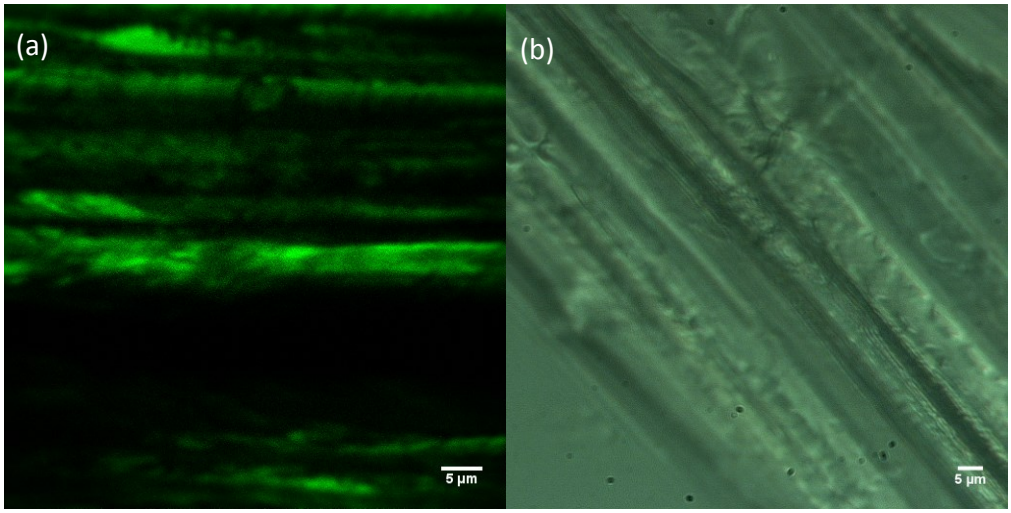

Figure 64: KDP crystal (a) Epi SHG excited at 800 nm (b) White light transmission image at 100X magnification

There is plenty of collagen in mouse tail tendons, ideal for SHG imaging. A tendon sample from a mouse tail was sourced, and placed on a #1 coverslip, with a second coverslip placed on top. The sample was placed on the microscope stage and exposed to 12 mW of 800 nm pump light. Preparing the mouse tail collagen proved to be quite difficult, as it was very dense and firm. Slicing a thin, even section provided a significant challenge, with the best image displayed in Figure 64.

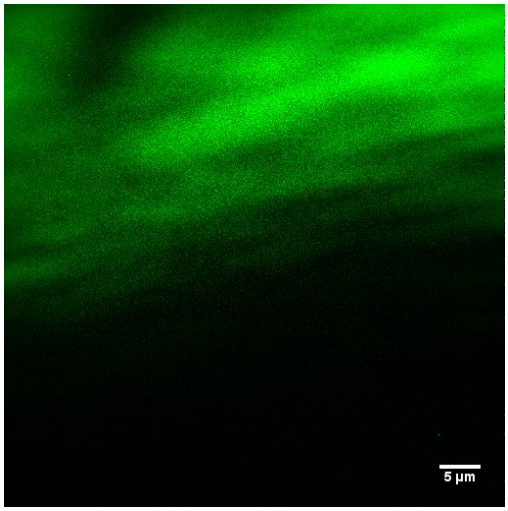

Figure 65: Epi SHG image of mouse tail collagen

4.3.3.3 Coherent Anti-Stokes Raman Scattering

The culmination of the work on the development of this exoscope is in the demonstration of the CARS imaging capability in the epi direction. Careful selection of a sample is incredibly critical primarily due to the reduction of the CARS signal in the epi direction. Various samples and preparation methods were attempted, with two samples providing adequate images to prove the functionality of the exoscope. The first sample cultured for its localized lipid droplets was embryonic 3T3-L1 cells (ATCC, USA) differentiated into adipocytes. Adipocytes are specialized cells that have high concentration of lipid droplets, primarily used as a cellular energy storage device. Traditionally adipocytes were imaged with exogenous dyes such as Oil Red O [55] or Nile Red [56]. In addition to only allowing indirect observation of ex-vivo fixed samples, the structure of the lipid droplets could be modified by either the addition of the dye or the fixation process. CARS has been a very important imaging

modality when observing lipid droplet concentration, growth patterns and determining functions beyond energy storage, and will serve as an excellent platform for exoscope demonstration.

The method of preparation followed the differentiation protocol demonstrated by CS Rubin's paper on preadipocytes and adipocytes [57]. The adipocytes were fixed via a methanol solution and mounted within a chambered cover glass slide. The vibrational mode of the C-H bonds at 2845 cm^{-1} contained within the adipocytes is resonantly excited by the frequency difference between the pump and the Stokes wavelengths. The adipocytes were exposed to 10 mW of the 800 nm pump beam, as well as 0.6 mW of the 1030 nm Stokes beam. The generated CARS signal was collected in the epi direction. The pumping wavelengths and any other unwanted signal is extinguished with a 65 nm band pass filter with central peak at 645 nm (Chroma Technology, VT, USA) while allowing the epi collected photons to reach the PMT. Illumination solely by either the pump or the Stokes wavelengths results in the disappearance of the lipid droplets, demonstrating that CARS is the primary source of the detected signal. A graphic of the differentiation process is displayed in Figure 66 [58] and helps explain the images obtained by the exoscope. Figure 67 displays the adipocyte cells in a mixture of states, mature adipocytes as well as some in the intermediate state. The mature adipocytes making up the majority of the image with the large lipid droplets, while the immature adipocytes still containing smaller lipid droplets (seen as smaller bright regions) that have not yet accumulated into a larger mass.

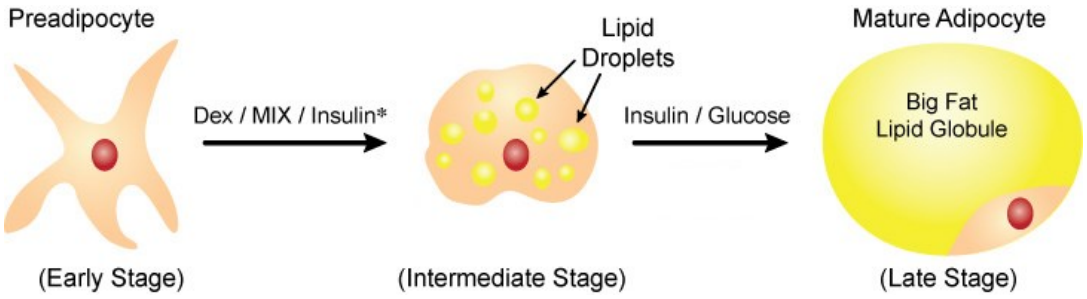

Figure 66: Adipocyte differentiation process [58]

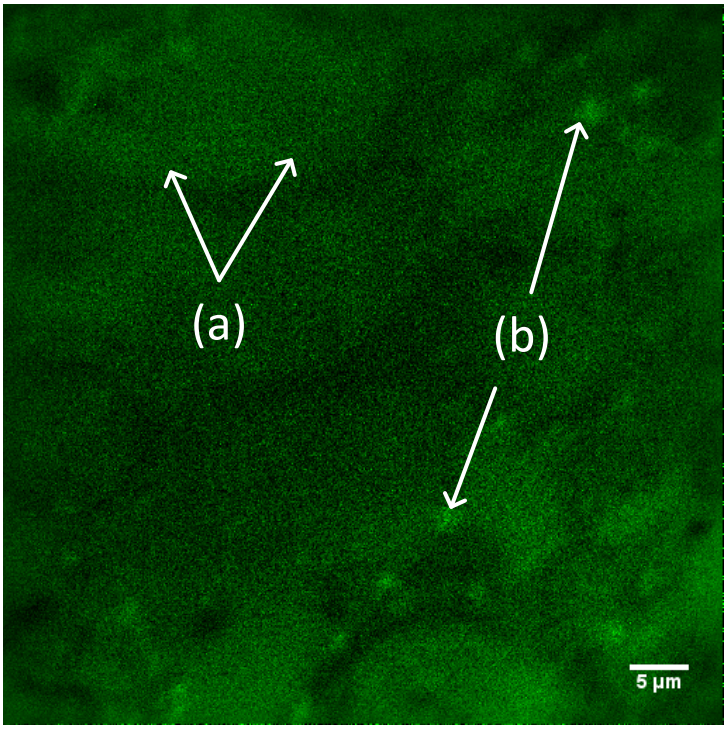

Figure 67: Epi CARS image from cell membrane (a) and lipid droplets (b) of unstained adipocyte cells

The second image sample was human orbital tissue, specifically adipose tissue that is similar to the differentiated embryonic adipocytes. The larger feature size, and upgraded pump compression gratings (and perhaps the sample quality) were responsible for the increase in available pump power and subsequent CARS signal and enhanced SNR when compared to the embryonic adipocytes. The same fixing and mounting procedure was followed for the orbital cells as the differentiated adipocytes. In order to obtain the images demonstrated in Figure 68 (a), the orbital sample was exposed to 19 mW of the 800 nm pump beam, as well as 0.62 mW of the 1030 nm Stokes beam. For comparison purposes a standard, white light transmission microscope was used to image the same sample. The image shown in Figure 68 (b) used a 100X magnification objective (with a similar field of view as the exoscope), and Figure 68 (c) used a 20X magnification objective for reference.

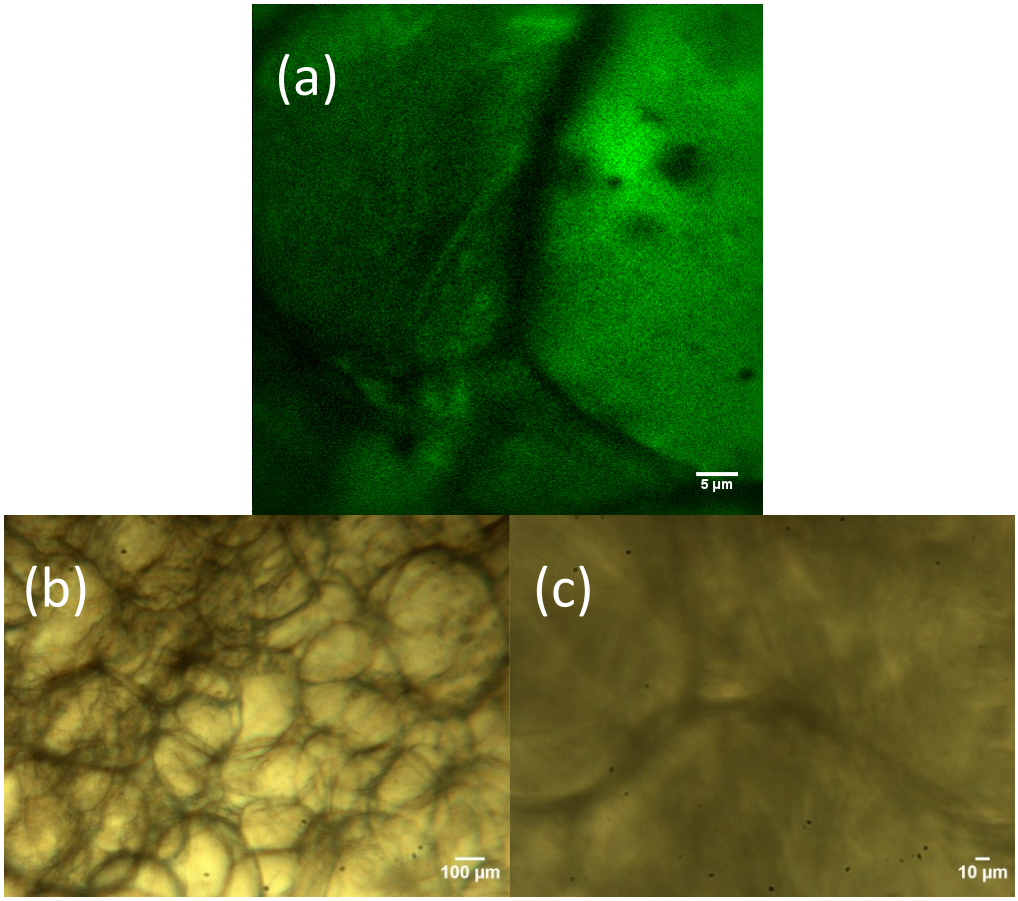

Figure 68: Human orbital fat tissue (a) Epi CARS image (b) For comparison: White light transmission microscope image at 20X magnification (c) For comparison: White light transmission microscope image at 100X magnification

It is clear, based on the prior evidence of images and resolution measurements that the exoscope is a fully functioning multimodal imaging tool. The TPEF, CARS and SHG images obtained with the barrel and free-space optics confirmed that there were no glaring errors with the assembly of the miniaturized lenses. These images also confirmed the successful operation of the MEMS mirror, and the subsequent image capture and reconstruction process. The completely assembled exoscope also demonstrated similar quality images of the same modalities. It is important to note that the CARS images obtained from the fully assembled exoscope have a lower SNR due to the inherent weaker generation of epi-CARS photons. These images are not the last that will be taken with the exoscope. Further experimentation with alternative samples will be done, as well as trials with different laser sources. These future plans will be examined in the following chapter.

Chapter 5

Discussion

When examining what was accomplished in this thesis, first, a larger picture must first be analyzed. It is easy to get caught up in the specialized technologies employed in order to accomplish the CARS imaging that was previously demonstrated, while losing sight of the potential substantial medical applications this device could accomplish. One such potential application is in spinal cord disorder research. Spinal cord disorders have lifelong consequences, often having disastrous impacts on the patients and their families. These disorders can occur through traumatic events such as fractures, or penetrating injuries that cause damage to the white matter contained within the spinal column. This white matter facilitates the transfer of electrical signals descending, or ascending the spinal column. Depending on the severity of the effect on the conduction of these electrical signals, these traumatic events can lead to severe paralysis. Another significant source of spinal cord disorders is MS. Again, this is can be a devastating disease, as MS is progressive, irreversible and has no treatments to reverse progression once onset.

While animal models of spinal cord injuries and MS have been developed, there is limited understanding as to the progression of tissue changes over time. Current methods applied to the histological examination of lab animals involve the sacrifice of multiple specimens. This only allows for a brief snapshot of the state of the white matter within the spinal column. Serialized examinations over time could offer a significant increase in the understanding the progression of medical therapies applied to spinal cord disorders. This is accomplished by non-invasive therapies such as magnetic resonance imaging, although with limited resolution capabilities. The exoscope demonstrated in this thesis allows for minimally-invasive, chronological examinations of a single specimen with microscopic accuracy, all while enabling the observations of morphological and chemical changes within the tissue.

Although this thesis does not directly address the problems associated with spinal cord injury, it demonstrates that these kinds of images are possible. The actual purpose of this thesis is to develop a fully functional miniaturized microscope that enables TPEF, SHG, and CARS imaging. As anticipated, the bulk of the work centred on sourcing and testing appropriate components suitable for ultrafast beam delivery while maintaining as small as possible footprint. All of this needed to be accomplished while managing to maintain high peak power pulses with little net negative chromatic effects. Sourcing appropriate samples to exploit the aforementioned modalities proved to be more of a challenge than was anticipated, the same goes for the debugging of the system to increase the quality of the images. These challenges were met, and the first major step toward a fully endoscopic, multimodal nonlinear microscope was successfully demonstrated.

5.1 Summary

This section will summarize the results obtained in previous chapters, and explain possible improvements that can be made on the microscopy system in order to increase image quality. Sources of the reduction of quality of the focusing system will also be discussed, as well as a review on the functionality of the key components.

The first issue addressed, was the method of photon delivery. This aspect was crucial to the success of the project; if ultrafast light could not be delivered efficiently to the exoscope, the quality of the exoscope optics would be irrelevant. The DCPCF was the first fibre that was investigated, with a prism compressor used as the compensation mechanism. The difficulty in focusing the pump beam into the inner core of the DCPCF made difficult work compensating for the dispersion encountered within the fibre. The two discrete core paths that the pump beam could travel down resulted in an impossible compensation geometry, the two very different effective dispersions encountered in the fibre resulted in two pulse widths

separated by greater than an order of magnitude. The LMA-20 used as an alternative did not have this drawback. The pump and stokes were either coupled to the core, or scattered out of the cladding making dispersion compensation straight forward. The LMA-20 performed very well throughout the experiments and imaging executed in this thesis.

Another component that performed successfully once installed, was the MEMS mirror. The robustness of single crystal silicon allowed the system to operate for many hours on end without any loss of deflection magnitude. The actual installation of the MEMS chip, however, led to further difficulties. The miniaturized housing that the MEMS was inserted into left much to be desired in terms of how well seated and secure was the chip. This lack of a secure resting place for the MEMS also meant that the ability to finely control the X, Y, pitch and yaw was almost non-existent. The final placement of the mirror was based on macro movements, and largely on luck. The uncertain placement of the MEMS mirror also had the unintended consequence of having one of the electrical contacts intermittently bridge a connection to the body of the exoscope. Fortunately only one of the contacts made this connection and the entire system did not have to undergo disassembly and the lengthy process of realignment. This electrical short-circuit could be prevented by coating the rear of the MEMS mirror with an insulating adhesive. The issue of the fine positioning of the MEMS is a more problematic issue, and would require a re-design of the housing section of the exoscope. Regardless of these setbacks, the MEMS still managed to perform its duty as a two-dimensional scanner with consistency.

The MEMS mirror was not the only element that had a problematic install into the miniaturized optical housing. While the barrel individually performed as expected, it was difficult to obtain an on optical axis output with high output power. Due to the miniaturized nature of the probe, the transmission efficiency or the optical deviation that individual components imparted on the system could not be analyzed. An additional source of error impacting the output angle of the barrel could also be the position of the input fibre. Unbeknownst at the time of assembly, the company that

connectorized the LMA-20 had very little control over the lateral position of the fibre tip. This was assumed to be correctly placed in the exact centre of the ferrule, thus the collimating lens had no X-Y adjustment built in. Based on this observation, it is possible that the very first optical component could be responsible for the optical output angle shift. An off axis optical beam could also be responsible for the increased axial resolution that was observed, as well as the chromatic aberrations that were reported. Additional pinholes built into the design of the exoscope could have given the ability to identify an off axis beam path. A method to monitor the power after every optical component or reflection would give extremely valuable information to the alignment of components. One such possible solution could be a miniaturized reflector that would be inserted into the beam path of the exoscope to direct the beam out of the miniaturized cavity to an external power meter.

All of these previous difficulties that occurred during the assembly of the exoscope could directly have an effect on the quality of the images obtained, as well a potential reason why the axial resolution measurement was off when compared to the designed value. Reducing these inaccuracies would most certainly improve the acquired images, whether they are of microspheres, crystals, or biological tissue.

5.2 Future Work

Performing CARS imaging of lipid rich tissues is only the first half of the project intended for the exoscope. Now that it has been successfully demonstrated, in vivo trials will be performed on the spinal tissue of a live rat. Not only will the lipids contained within the white matter be illuminated, but genetically encoded fluorescent proteins will be excited. These combined modalities will reveal the chemical changes in myelin and axons when various treatment strategies are being experimented. There are two experiments planned to investigate the rate of degradation of spinal cord myelin. The first is based on a contusive traumatic injury model. First a rat will be anesthetized, and a neurosurgeon will expose the dorsal

spinal cord at the thoracic level via a laminectomy. A guide tube will be inserted into the cavity made by the neurosurgeon, allowing the insertion of the exoscope tip. Following this surgery, a fluorescent dye will be injected into the rat, allowing the exoscope to illuminate the surface vasculature of the dorsal spinal cord. The vasculature will serve as a landmark, ensuring the probe is directed toward the same location for multiple imaging sessions. The spinal column will be mechanically injured, and CARS images of the myelin will be acquired, over many imaging sessions. The second experimental method is done by using a focal demyelination model. The rats will be prepared in a similar manner to the previous method, but instead of blunt trauma causing the damage, a solution of lysolecithin will be injected into the spinal cord. This causes rapid degradation of the myelin, while leaving the axons intact. The demyelination process will be monitored over the first 3 days, while the progression of remyelination that occurs from about 7-14 days post injury, will also be examined.

The techniques learned imaging the myelin of a live rat can also be applied elsewhere. With little to no changes to the hardware, chronological imaging of different organs of live specimens can also be performed. The applications of this are quite broad and significant. Notice that the last statement didn't include a qualification that the organism being imaged had to be a lab rat. It is quite conceivable that this very instrument could be brought to the bedside, and used as a multi-photon imaging probe. These applications could range from surgical interventions, to disease diagnosis.

While these myelination trials are being investigated, a second iteration of the exoscope will be built. Lessons learned from the first assembly will be applied, and special attention will be given to the location of the fibre tip within the LMA-20's ferrule. Further improvements on this exoscope will reduce the optical aberrations of the system in a second iteration. Signal collection will be improved by using a more sensitive PMT. In the far future, further miniaturization will be done, perhaps modifying the beam geometry to only have a single reflection off the MEMS mirror

making a 90 degree probe. Inserting the MEMS mirror in between the optics of the barrel could also reduce the size of the exoscope, although this would increase the difficulty of fabrication and alignment.

A future application of this further miniaturized probe could be in atherosclerosis research. While the size of the current exoscope would not fit inside a human artery, it is conceivable that further miniaturization would allow artery insertion. Giving physicians the ability to extract morphological and chemical data from the inside of an artery could significantly reduce the amount of human deaths caused by blood flow reduction. Although with current bulky laser sources, this dream of a bedside multimodal endoscope is impossible. Fortunately, much work is being done to develop a femtosecond fibre laser [28]. Trials will be performed with this setup, which will reduce the footprint of the entire system, bringing multimodal nonlinear imaging closer to a clinical application.

References

[1] M. Minsky, "Microscopy Apparatus". United States of America Patent 313467, 19 Dec 1961.

[2] F. J. McClung and R. W. Hellwarth, "Giant Optical Pulsations from Ruby," *Applied Optics,* vol. 1, no. S1, pp. 103-105, 1962.

[3] P. F. Moulton, "Spectroscopic and laser characteristics of Ti:Al2O3," *Journal of the Optical Society of America,* vol. 3, no. 1, pp. 125-133, 1986.

[4] A. F. Pegoraro, A. Stolow, A. Ridsdale, D. J. Moffatt, J. P. Pezacki and Y. Jia, "CARS Microscopy Made Simple," *Biophotonics,* October 2009.

[5] World Health Organization, "The top 10 causes of death," World Health Organization, Geneva, 2011.

[6] British Heart Foundation, "British Heart Foundation," [Online]. Available: http://www.bhf.org.uk/heart-health/conditions/coronary-heart-disease.aspx. [Accessed 13 02 2013].

[7] T. T. Le, I. M. Langohr, M. J. Locker and J.-X. Cheng, "Label-free molecular imaging of atherosclerotic lesions using multimodal nonlinear optical microscopy," *Journal of Biomedical Optics,* pp. 054007-1 - 054007-10, 2007.

[8] D. Shria, "Suboxone Assisted Treatment," 6 January 2007. [Online]. Available: http://suboxoneassistedtreatment.org/17.html. [Accessed 13 02 2013].

[9] H. Kasai, T. Kishimoto, T. Nemoto, H. Hatakeyama, T.-T. Liu and N. Takahashi, "Two-photon excitation imaging of exocytosis and endocytosis and determination of their spatial organization," *Advanced Drug Delivery Reviews,* pp. 850-877, 2006.

[10] R. W. Boyd, Nonlinear Optics, Burlington: Academic Press, 2008.

[11] P. Pantazis, "Second harmonic generating (SHG) nanoprobes for in vivo imaging," *Proceedings of the National Academy of Sciences of the United States of America,* vol. 107, no. 33, pp. 14535-14540, 2010.

[12] E. Hecht, Optics, San Francisco: Addison Wesley, 2006.

[13] S. Murcia-Mascaros and J. V. Garcia-Ramos, "National Institute of Material Physics," [Online]. Available: http://alpha1.infim.ro/cost/pagini/handbook/chapters/raman.htm. [Accessed 13 02 2013].

[14] A. Yariv and P. Yeh, Photonics, New York: Oxford University Press, 2007.

[15] Columbia University, "Intensive Seminars in Modern Chemistry. Experiment 7 IR Spectroscopy," New York, 2007.

[16] J.-X. Cheng, "Coherent Anti-Stokes Raman Scattering Microscopy," *Applied Spectroscopy ,* vol. 61, no. 9, pp. 197-208, 2007.

[17] K. P. Knutsen, J. C. Johnson, A. E. Miller, P. B. Petersen and R. J. Saykally, "High spectral resolution multiplex CARS spectroscopy," *Chemical Physics Letters,* pp. 436-441, 2004.

[18] J. M. Dudley, "Supercontinuum generation in photonic crystal fiber," *Reviews of Modern Physics,* pp. 1135-1184, 2006.

[19] R. R. P and P. T. J, "On the possibility of measuring gas concentrations by stimulated anti-Stokes scattering," *Applied Physics Letters,* pp. 240-242, 1973.

[20] V. M. O, B. L. M, K. C. R and C. E. A, "Spatially resolved coherent anti-Stokes raman spectroscopy from a line across a CH4 jet," *Optics Letters,* pp. 167-169, 1979.

[21] D. D. M, R. J and J. M. T, "Scanning coherent anti-Stokes Raman microscope," *Optics Letters,* pp. 350-352, 1982.

[22] A. Zumbusch, G. R. Holtom and X. S. Xie, "Three-Dimensional Vibrational Imaging by Coherent Anti-Stokes Raman Scattering," *Phyiscal Review Letters,* vol. 82, no. 20, pp. 4142-4145, 1999.

[23] O. E. Potma, P. W. de Boeij and A. D. Wiersma, "Nonlinear coherent four-wave mixing in optical," *Journal of the Optical Society of America,* pp. 1678-1684, 2000.

[24] J.-X. Cheng, A. Volkmer and X. S. Xie, "Theoretical and experimental characterization," *Journal of the Optical Society of America,* pp. 1363-1375, 2002.

[25] J.-x. Cheng, A. Volkmer, L. D. Book and X. S. Xie, "An Epi-Detected Coherent Anti-Stokes Raman Scattering (E-CARS) Microscope with High," *The Journal of Physical Chemistry,* pp. 1277-1280, 2001.

[26] S. Murugkar, C. Brideau, A. Risdale, M. Naji, P. K. Stys and H. Anis, "Coherent anti-Stokes Raman scattering microscopy using photonic crystal fiber with two closely lying

zero dispersion wavelengths," *Optics Express,* vol. 15, no. 21, pp. 14028-14037, 2007.

[27] International Engineering Consortium, "Fiber-Optic Technology," [Online]. Available: http://www.hyperline.com/info/fiber/index.php?id=6. [Accessed 29 April 2013].

[28] J. K. Ranka, "Visible continuum generation in air-silica microstructure," *Optics Letters,* pp. 25-27, 2000.

[29] H. P. Uranus, H. J. Hoekstra and E. v. Groesen, "Modes of an endlessly single-mode photonic crystal," *Proceedings Symposium IEEE/LEOS Benelux Chapter,* pp. 311-314, 2004.

[30] L. Fu and M. Gu, "Double-clad photonic crystal fiber coupler for compact nonlinear optical microscopy imaging," *Optics Letters,* pp. 1471-1473, 2006.

[31] F. Légaré, C. L. Evans, F. Ganikhanov and X. S. Xie, "Towards CARS Endoscopy," *Optics Express,* vol. 14, no. 10, pp. 4427-4432, 2006.

[32] H. Wang, T. B. Huff, Y. Fu, K. Y. Jia and J.-X. Cheng, "Increasing the imaging depth of coherent anti-," *Optics Letters,* vol. 32, no. 15, pp. 2212-2214, 2007.

[33] M. Balu, G. Liu, Z. Chen, B. J. Tromberg and O. E. Potma, "Fiber delivered probe for efficient CARS imaging of tissues," *Optics Express,* pp. 2380-2388, 2010.

[34] NKT Photonics, "Photonic Crystal Fibrers," 2013. [Online]. Available: http://www.nktphotonics.com/fiber. [Accessed 29 April 2013].

[35] Newport Spectra Physics, *Prism Compressor for Ultrashort Laser Pulses,* Newport Corporation, 2006.

[36] K. J. Bock, "Femtosecond Fiber Lasers," University of Ottawa, Ottawa, 2012.

[37] NKT Photonics, "LMA-20," [Online]. Available: http://www.nktphotonics.com/files/files/LMA-20.pdf. [Accessed 28 04 2013].

[38] ThorLabs, "Endlessly Single Mode, Large-Mode-Area-Fiber," 2013. [Online]. Available: http://www.thorlabs.com/newgrouppage9.cfm?objectgroup_id=1902. [Accessed 28 04 2013].

[39] E. Treacy, "Optical pulse compression with diffraction gratings," *IEEE Journal of Quantum Electronics,* pp. 454-458, 1969.

[40] L. Fu, A. Jain, H. Xie, C. Cranfield and M. Gu, "Nonlinear optical endoscopy based on a double-clad photonic crystal fiber and a MEMS mirror," *Optics Express,* pp. 1027-1032,

2006.

[41] B. G. Saar, R. S. Johnston, C. W. Freudiger, X. S. Xie and E. J. Seibel, "Coherent Raman scanning fiber endoscopy," *Optics Letters,* pp. 2396-2398, 2011.

[42] S. Tang, W. Jung, D. McCormick, T. Xie, J. Su, Y.-C. Ahn, B. J. Tromberg and Z. Chen, "Design and implementation of fibre-based multiphoton endoscopy with microelectromechanical systems scanning," *Journal of Biomedical Optics,* pp. 034005-1 - 034005-7, 2009.

[43] T.-M. Liu, M.-C. Chan, I.-H. Chen, S.-H. Chia and C.-K. Sun, "Miniaturized multiphoton microscope with a 24Hz frame-rate," *Optics Express,* pp. 10501-10506, 2008.

[44] Fraunhofer Institut Photonische Mikrosysteme, "We shape the light," 2008.

[45] H. Schenk, "2D-Scanner for endoscopic applications," Fraunhofer Institut Photonische Mikrosysteme, Dresden, 2008.

[46] Chroma Technology, "ET645/30x-PF," 2012. [Online]. Available: http://www.chroma.com/product/individual-filters-mirrors/widefield-microscopy/ET645_x_30x-PF-EX. [Accessed 26 January 2013].

[47] Hamamatsu, "Photosensor Module," [Online]. Available: http://www.hamamatsu.com/jp/en/product/alpha/C/3044/H7422-50/index.html. [Accessed 12 February 2013].

[48] C. Luu and M. Kalloniatis, "Webvision," 5 June 2007. [Online]. Available: http://webvision.med.utah.edu/book/part-viii-gabac-receptors/visual-acuity/. [Accessed 6 October 2012].

[49] K. R. Spring, T. J. Fellers and M. W. Davidson, "Olympus Laser Scanning Confocal Microscopy," Olympus, 2009. [Online]. Available: http://www.olympusconfocal.com/theory/resolutionintro.html. [Accessed 17 April 2013].

[50] Edmund Optics, "1951 USAF Glass Slide Resolution Targets," 2013. [Online]. Available: http://www.edmundoptics.com/testing-targets/test-targets/resolution-test-targets/1951-usaf-glass-slide-resolution-targets/1790. [Accessed 9 December 2011].

[51] University of Victoria, "Advanced Imaging Laboratory Epi-Fluorescence with the Microscope," 21 September 2005. [Online]. Available: http://web.uvic.ca/ail/techniques/epi-fluorescence.html. [Accessed 08 01 2013].

[52] Sigma-Aldrich, "Sigma-Aldrich," Sigma-Aldrich, 2013. [Online]. Available: http://www.sigmaaldrich.com/catalog/product/aldrich/161004?lang=en&region=CA. [Accessed 2013].

[53] University of Rochester, "Chem 421: Introduction to Polymer Chemistry," [Online]. Available: http://chem.chem.rochester.edu/~chem421/intro1.htm. [Accessed 17 April 2013].

[54] E. Spiess, F. Bestvater, A. Heckel-Pompev, M. Hacker, G. Strobrawa, T. Feurer, C. Wotzlaw, U. Berchner-Pfannschmidt, T. Porowl and H. Acker, "Two-photon excitation and emission spectra of the green fluorescent protein variants ECFP, EGFP and EYFP," *Journal of Microscopy,* pp. 200-204, 2005.

[55] R. Koopman, G. Schaart and M. K. Hesselink, "Optimisation of oil red O staining permits combination with immunofluorescence and automated quantification of lipids," *Histochem Cell Biol.,* pp. 63-8, 2001.

[56] P. Greenspan, E. P. Mayer and S. D. Fowler, "Nile red: a selective fluorescent stain for intracellular lipid droplets," *J Cell Biol.,* pp. 965-73, 1985.

[57] C. S. Rubin, A. Hirsch, C. Fung and O. M. Rosen, "Development of hormone receptors and hormonal responsiveness in vitro. Insulin receptors and insulin sensitivity in the preadipocyte and adipocyte forms of 3T3-L1 cellsJ Biol Chem.," *J Biol Chem.,* pp. 7570-8, 1978.

[58] M. N. James, "Biochemistry," 7 9 2011. [Online]. Available: http://www.biochem.wisc.edu/faculty/ntambi/images/5_Ntambi_cells.jpg. [Accessed 11 02 2013].

[59] Kaiser Optical Systems Inc, "Kaiser Optical Systems Inc," [Online]. Available: http://161.58.205.25/Raman_Spectroscopy/rtr-ramantutorial.php. [Accessed 13 02 2013].

[60] M. L. Roldan, H. Lanus, S. A. Brandan, J. J. Lopez, E. L. Varetti and A. Ben Altabef, "The infrared spectrum of tetrachlorophosphonium oxotetrachlorovanadate. An experimental and theoretical study," *The Journal of the Argentine Chemical Society,* pp. 53-61, 2004.

[61] Horiba Scientific, "Horiba Scientific," [Online]. Available: http://www.horiba.com/scientific/products/raman-spectroscopy/tutorial-faqs/raman-faqs/how-long-does-it-take-to-acquire-a-raman-spectral-image/. [Accessed 13 02 2013].

[62] World Health Organization, Atlas Multiple Sclerosis Resources in the World, Geneva: World Health Organization, 2008.

[63] Life Technologies, "Life Technologies," [Online]. Available: http://www.invitrogen.com/site/us/en/home/support/Product-Technical-Resources/Product-Spectra.1300ph9.html. [Accessed 14 02 2013].